UNIVERSITY OF OTTAWA

DOCTOR OF PHILOSOPHY THESIS

Mechanisms of Enhancement of Nonlinear Optical Interactions in Nonlinear Photonic Devices based on III-V Semiconductors

Author:

Ehsan MOBINI

Supervisor:

Prof. Ksenia DOLGALEVA

A thesis submitted in partial fulfillment of the requirements for the Doctorate of Philosophy in Physics

Department of Physics
Faculty of Science
University of Ottawa

Declaration of Authorship

I, Ehsan MOBINI, declare that this thesis, titled "Mechanisms of Enhancement of Nonlinear Optical Interactions in Nonlinear Photonic Devices based on III-V Semiconductors", and the work presented in it are my own. I confirm that except where specific reference is made to the work of others, the contents of this dissertation are original and have not been submitted in whole or in part for consideration for any other degree or qualification in this, or any other university. This dissertation is my own work and contains nothing which is the outcome of work done in collaboration with others, except as specified in the text and Acknowledgements.

Ehsan Mobini
July, 2022
Ottawa, Canada

Abstract

The family of III-V semiconductors is of high significance in photonics for two main reasons. First, not only they are the most practical material platforms for active photonic devices but also they are suitable for monolithic integration of passive and active photonic devices. Second, some III-V compounds exhibit high values of second and third-order nonlinear coefficients – the property useful in all-optical signal processing and wavelength conversion. This Ph.D. thesis explores the above perspectives with two candidates from the group III-V family, namely AlGaAs and InGaAsP. The dissertation consists of two main parts. The first part is dedicated to the theoretical modelling of nonlinear bianisotropic AlGaAs metasurfaces, while the second part focuses on the experimental studies of the nonlinear optical performance of InGaAsP waveguides.

Concerning the first part, due to the high confinement of light supported by the Mie resonances, AlGaAs nanoantennas and metasurfaces with both high refractive index and high nonlinear susceptibility have found a unique place in planar nonlinear optics, where not only the presence of high intensity of light is of significant matter, but also the optically thin thickness of the entities releases the device from phase matching. We first describe the linear optical properties of AlGaAs meta-atoms and metasurfaces such as relatively high scattering cross-sections and the bianisotropic effect. Also, we derive and explain all required analytic formulas for this purpose. Bianisotropic metasurfaces with magnetoelectric coupling and asymmetric optical properties have sparked considerable interest in *linear* meta-optics. However, further in this thesis, we explore the *nonlinear* features of bianisotropic AlGaAs metasurfaces. In particular, we explore a second-harmonic generation in a bianisotropic AlGaAs metasurface based on the multipolar interference inside the meta-atoms and the nonlinear polarization current. We theoretically demonstrate that it is possible to obtain several orders of magnitude second-harmonic power differences for the forward and backward illuminations by adjusting the geometrical parameters of the meta-atoms in such a way that

quasi-bound states in the continuum (quasi-BICs) are achievable. This research paves the way for the generation of directional higher-order waves.

Concerning the second part, the research is focused on exploring nonlinear material platforms for monolithic integration of active and passive devices on the same chip. In this regard, we explore InGaAsP/InP waveguides of different geometries. First, we provide the theoretical background such as the nonlinear Schrodinger equation and four-wave mixing (FWM) equations in a nonlinear waveguide, then we solve the set of FWM equations using MATLAB to observe the qualitative behavior of the signal, idler, and the pump inside a nonlinear waveguide. Furthermore, we design and employ two waveguide geometries *i.e.* half-core and nanowire waveguides. We first design these waveguides so that achieving zero group velocity dispersion is possible through a suitable material composition and certain geometrical dimensions. However, for the rest of the work, we continued with the waveguides of different dimensions compared to the designed ones (due to some limitations in fabrication). We demonstrate self-phase modulation (SPM) and FWM for the half-core waveguides. For the case of the nanowire waveguides, we also demonstrate the FWM effect. We measured and extracted the effective value of the nonlinear refractive index of InGaAsP/InP waveguides to be $n_2 = 1.9 \times 10^{-13}\,\mathrm{cm}^2/\mathrm{W}$ through the relation between the idler and the pump power when the phase mismatch is negligible. Finally, we experimentally observe the two-photon absorption effect in our waveguides through the nonlinear characteristics of input and output powers of the waveguides from which the two-photon absorption coefficient of 19 cm/GW is calculated.

Acknowledgements

It would be impossible to properly thank everyone who contributed to the completion of my thesis. Prof. Ksenia Dolgaleva deserves special recognition for including me in the group and creating a wonderful academic place to work in. As a member of the nonlinear photonics group, the research experiences she provided for me were really valuable. Thank you, Ksenia, for all of your scientific advice, encouragement, and patience with me over the course of my Ph.D., which lasted nearly five years.

I would like to thank all CERC members, especially Prof. Robert W. Boyd who was a big motivation for me to choose the topic of nonlinear optics for my Ph.D. program. In particular, It was great to attend every-week CERC research talks and communicate with many people from different backgrounds.

I am grateful to my collaborator Dr. Rasoul Alaee for his collaboration with the first part of the thesis. Rasoul was a great help for this part. He shared his valuable experience in the physics of scattering with me. Thank you, Rasoul, for all of your time of discussion. I am also grateful to Dr. Daniel Espinosa, for his collaboration with the second part of the thesis. Daniel was a great help to me to do measurements and characterization of InP devices in the lab. Thank you, Daniel, for your patience and time in training me in the lab. I would like to thank my groupmate, Kaustubh Vyas, who fabricated all InP devices reported in this thesis. He made much effort for all those fabrications even during the covid time.

I would like also to thank other past postdoc members Dr. Akbar Safari and Dr. Orad Reshef for all discussions we had. Special thanks to other group members Saad, Daniel Hutama, Sina, Daniel Espinosa, Soheil, Shubhendra, Kaustubh, Rania, Ozan, Tuhin.

I would like to thank other friends in Advanced Research Complex (ARC) namely Mohammad Karimi, Payman Rasekh, Pedram Abdolghader, Maryam Amiri, Farshad NejadSattari, Mitra Rahimian, Zohreh Hirbodvash, Hamed Mozaffari, Masoud Shaabani, and Qasem Exirifard.

Finally, I would like to express my heartfelt gratitude to my parents, sisters, and brothers for endless reasons.

Contents

List of Figures

List of Abbreviations

AlGaAs	**A**luminium **G**allium **A**rsenide
InGaAsP	**I**ndium **G**allium **A**rsenide **P**hosphide
SPR	**S**urface **P**lasmon **R**esonance
LSPR	**L**ocalized **S**urface **P**lasmon **R**esonance
BIC	**B**ound states **I**n the **C**ontinuum
TIR	**T**otal **I**nternal **R**eflection
VSH	**V**ector **S**pherical **H**armonics
PML	**P**erfectly **M**atched **L**ayer
SHG	**S**econd **H**armonic **G**eneration
THG	**T**hird **H**armonic **G**eneration
FWM	**F**our **W**ave **M**ixing
DFWM	**D**egenerate **F**our **W**ave **M**ixing
NDFWM	**N**on **D**egenerate **F**our **W**ave **M**ixing
NLSE	**N**on **L**inear **S**chrodinger **E**quation
GVD	**G**roup **V**elocity **D**ispersion
ZGVD	**Z**ero **G**roup **V**elocity **D**ispersion
SVEA	**S**lowly **V**arying **E**nvelope **A**pproximation
TOD	**T**hird **O**rder **D**ispersion
SPM	**S**elf **P**hase **M**odulation
TPA	**T**wo **P**hoton **A**bsorption
OPO	**O**ptical **P**arametric **O**scillator
HWP	**H**alf **W**ave **P**late
OSA	**O**ptical **S**pectrum **A**nalyzer
FCA	**F**ree **C**arrier **A**bsorption
FCD	**F**ree **C**arrier **D**ispersion
EDFA	**E**rbium **D**oped **F**iber **A**mplifier

Chapter 1

Introduction

Nonlinear optics plays a significant role in harmonic generation, ultrashort-pulse lasers, ultrafast optical switching, optical signal processing, and other applications [1]–[10]. To enhance the efficiency of nonlinear optical processes, nonlinear photonic devices either in free space or integrated forms have been developed based on different nonlinear optical materials [11]–[16]. Among efficient nonlinear optical materials, III-V compounds are increasingly attracting interest in photonics due to various reasons such as their suitability for monolithic integration of active and passive devices and exhibiting large nonlinear coefficients. These functionalities could be very helpful in all-optical signal processing, wavelength conversions, supercontinuum and frequency-comb generation. In this regard, here, we select two most common optical devices in free space and integrated photonics, namely metasurfaces and optical waveguides, respectively, to unlock potential nonlinear capabilities of III-V semiconductor compounds. We further introduce optical metasurfaces and waveguides in the following two sections.

1.1 Optical Metasurfaces

To introduce the concept of metasurfaces, it is helpful to start with the concept of electromagnetic metamaterials. Metamaterials were first experimentally realized in bulk (three-dimensional or 3D) form in the microwave regime [17], [18]. They were introduced as artificial periodic unit cells (metallic split ring resonators and wires as the building blocks or meta-atoms) with the periodicity much smaller than the incident wavelength. The artificial medium comprised of the meta-atoms exhibits overall effective electromagnetic permittivity and permeability that is controllable in sign and magnitude through

the material selection and adjustment of the geometrical parameters of the meta-atoms. In this regard, such artificial media enable electromagnetic-wave manipulation and can exhibit peculiar optical properties not accessible in natural materials, e.g. negative refractive index [19], optical invisibility cloaking [20]–[22], hyperbolic dispersion characteristics [23], [24], and other.

Metasurfaces are the two-dimensional equivalent of bulk metamaterials that can manipulate the amplitude, phase, and polarization of the incident light. They are two-dimensional (2D) periodic or aperiodic arrangements of optically small scatterers (also known as meta-atoms) that are usually located on a very thin substrate. The meta-atoms in metasurfaces are mainly made of metals and dielectrics. The former and the latter are referred to plasmonic and all-dielectric metasurface, respectively. Up to now a variety of applications such as wavefront shaping [25], [26], beam steering [27], [28], polarization conversion [29], [30], directional scattering [31], [32], and other have been reported in plasmonic and dielectric metasurfaces.

In plasmonic metasurfaces, metallic meta-atoms manipulate the incident light through their resonant behavior. This resonant behavior originates from the collective oscillation of electrons in the conduction band and occurs at the boundary of metal and dielectric. Generally, these collective oscillations are associated with two electromagnetic modes (depending on the geometry), namely, surface plasmon resonance (SPR) [33] and localized surface plasmon resonance (LSPR) [33]. The first mechanism is related to the guiding structures such as plasmonic waveguides, however, the second one (i.e. LSPR) is associated with individual meta-atoms comprising a metasurface. For instance, for a sphere-shaped metallic meta-atom, the polarizability of the sphere (α) can be expressed as [33]

$$\alpha = 4\pi a^3 \frac{\varepsilon_{\text{sphere}} - \varepsilon_{\text{host}}}{\varepsilon_{\text{sphere}} + 2\varepsilon_{\text{host}}}, \tag{1.1}$$

where $\varepsilon_{\text{sphere}}$ and $\varepsilon_{\text{host}}$ are the permittivity of the metallic sphere and the host medium, respectively. The parameter a denotes the sphere radius. As can be seen from Eq. (1.1), the resonant behavior occurs when $\varepsilon_{\text{sphere}} = -2\varepsilon_{\text{host}}$ and consequently, high local electric field at the surface of a metallic sphere is generated. In plasmonic metasurfaces, resonances with high quality factors on the order of 10^3 (or narrow linewidth) are reported based on the constructive interference of in-plane scattered light from each meta-atom at the far-field, known as surface lattice resonance (SLR) [34], [35]. Another way

to obtain resonances with high quality factors in this type of metasurfaces is based on Fano resonances, which are sharp asymmetric resonances as a result of the interference between a localized state and the continuum or a broad resonance [36], [37].

Although the radiative loss can be reduced in plasmonic metasurfaces through the above mentioned solutions, these devices still suffer from the Ohmic loss. To this end, the idea of high-index dielectric meta-atoms was proposed for metasurfaces [38]. Dielectric metasurfaces are usually made of Si, AlGaAs, GaAs, Ge, and other materials. (Note that semiconductors at a certain frequency range can be considered as a dielectric material.) Dielectric materials exhibit negligible ohmic loss and support Mie resonances in meta-atoms including both electric and magnetic multipoles [39]. They can also exhibit Fano resonances [40], [41].

Recently, another mechanism known as quasi-bound-states in the continuum (quasi-BIC) has been receiving increasing attention. This mechanism allows one to obtain resonances with very high quality factors [42] (experimentally around 1000 [43]). Quasi BICs can usually be obtained in metasurfaces as a result of in-plane broken symmetry. These sharp resonances are suitable for high nonlinear conversion efficiencies [44]–[47].

Another advantage of dielectric metasurfaces is the additive role of nonvanishing electric field inside the dielectric meta-atom (in contrast to the metallic meta-atom, where the electric field is nonvanishing only at the surface). As a result of this voluminal contribution, more overall nonlinear interaction compared to that obtainable with the metallic counterparts can be achieved in dielectric metasurfaces [48].

Based on the above reasons, dielectric metasurfaces can provide very suitable platforms for nonlinear applications such as harmonics generation.

1.2 Optical waveguides

In contrast to table-top nonlinear setups assembled of bulk optical components, integrated nonlinear optical devices employ low-power incident light to reach the high-intensity regime for the nonlinear optical processes through extremely tight light confinement in ultra-compact integrated optical waveguides [49]. The basic guiding mechanism for optical waveguides is the total internal reflection (TIR) that implies the traveling of light inside the region

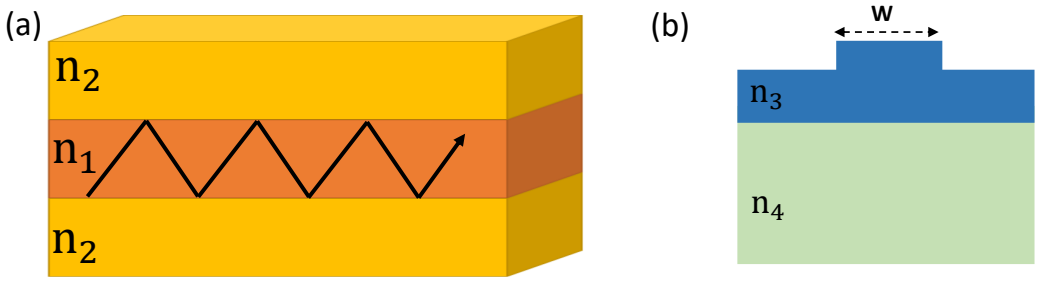

FIGURE 1.1: (a) Schematic of a slab waveguide exhibiting 1D light confinement in vertical dimension. The guiding mechanism is based on TIR. The refractive indices for the core (the central layer) and claddings (the peripheral layers) are n_1 and n_2, respectively, where $n_1 > n_2$. (b) A cross-sectional view of a rib waveguide for 2D light confinement, where $n_3 > n_4$.

with the higher refractive index. For instance, for a very simple structure like a slab waveguide (see Fig. 1.1 (a)), light can propagate in the central layer with a higher refractive index called the core or guiding layer [50]. More practical weaveguiding structures feature 2D light confinement *e.g.* a rib waveguide [50], see Fig. 1.1 (b). In this regard, the employment of dielectric/semiconductor waveguides made it possible to achieve the area of the eigenmodes occupied by the light in the structures on the order of sub-μm^2 [51], [52].

D. B. Anderson and J. T. Boyd reported the first experiment on frequency conversion in a planar waveguide in 1971, using a GaAs thin film as the nonlinear medium [53]. Other nonlinear optical experiments were reported in GaAs and AlGaAs waveguides [5], [16], [49], [52], [54]–[94], as well as InP-based nonlinear waveguide platforms [95]–[101]. In this regard, III-V semiconductors were the first waveguide platforms employed in nonlinear optics.

The search for new nonlinear waveguide materials with optimized nonlinear optical performances has been an active field of research since the early nonlinear waveguide experiments. Despite the significance of the achievements demonstrated in other promising material platforms (*e.g* silicon), they are not intrinsically suitable for monolithic integration of passive nonlinear optical devices with light sources and detectors. In contrast, III-V semiconductors like InP/InGaAsP can integrate all the necessary components on a single chip. Such components include not only passive waveguides for light guiding and nonlinear manipulation but also laser sources, modulators and detectors. In particular, over the last few decades, InGaAs/GaAs and

InGaAsP/InP quantum-well lasers operating at telecom wavelengths have been widely used [102], [103]. Furthermore, GaAs/ AlGaAsP quantum-well laser platforms are very common at room temperature [104], [105].

1.3 III-V semiconductor compounds

The III-V semiconductors are alloys of two (binary), three (ternary) or four (quaternary) elements from the group III (*e.g.* Al (aluminium) and Ga (gallium)) and group V (*e.g.* P (phosphorous) and As (arsenic)) of the periodic elements table. These compounds exhibit flexibility in terms of bandgap energy and the lattice constant, and play a crucial role in optoelectronics. Generally, the ternary and quaternary compounds can be expressed as $A_xB_{1-x}C$ and $A_xB_{1-x}C_yD_{1-y}$, respectively, where A, B, C, and D are chemical elements from the groups III and V, and $0 < \{x, y\} < 1$. All the material parameters such as the lattice constant, bandgap energy (E_g), refractive index and nonlinear optical coefficients, change with changing the material composition through varying x and y [106].

III-V active photonics started in 1962 [107], when Redhiker *et al*. created the first semiconductor laser based on GaAs. Since then III-V semiconductors have served as the backbone of active photonic devices such as lasers, electro-optic modulators, amplifiers, and photodetectors [108]. Although silicon is at the heart of photonic integrated circuits, it has an indirect bandgap that prevents it from functioning as a light source. However, most III-V compounds have a direct bandgap, see Fig. 1.2. Figure 1.2 displays bandgap energies versus the lattice constant for some binary, ternary, and quaternary III-V compounds. In this figure, the dots represent binary III-V compounds, which are made up of two different chemical elements. The lines that connect the dots represent the corresponding ternary alloys, and the areas that the lines occupy represent quaternary compounds based on the binaries at the corners.

Various parameters ($T_{ABC}(x)$) of any compound in Fig. 1.2, namely the bandgap energy or the lattice constant, can be calculated through Vegard's law which uses linear interpolation between the semiconductor AC and BC as:

$$T_{ABC}(x) = xT_{AC} + (1-x)\,T_{BC}. \tag{1.2}$$

Importantly, when E_g changes, the lattice constant varies as well, so, they are

not independent. Moreover, in integrated circuits, controlling and manipulating the guided light is very important. Typically, it is performed through waveguides made of two- or three-layer platforms, known as heterostructures. III-V heterostructures (*e.g.* ternary and quaternary compounds) provide a sufficient refractive index contrast to confine the light using different compositions of elements. To this end, the lattice-matching condition also should be considered as well. For example, the binary compounds AlAs and GaAs have very close lattice constants, see Fig. 1.2. Therefore AlGaAs layers with different compositions of x become lattice-matched to each other. For other compounds, specific conditions should be met. For instance, in InGaAsP where the substrate is typically InP, the lattice-matching condition is $x = 0.47 - 0.47 \times y$ [106].

The III-V semiconductors have the advantage of a short electron lifetime in comparison with silicon that makes them suitable for switching purposes [94], [109]. For instance, the recombination rate of GaAs is at least three orders of magnitude larger in comparison with that in silicon.

Another advantage of III-V semiconductors is that they exhibit high values of nonlinear optical coefficients [94], [110]. For instance, InGaAsP and AlGaAs have the third-order susceptibility $\left(\chi^{(3)}\right)$ of 4.2×10^{-10} esu [111] and 4.1×10^{-11}esu [79], respectively, which are all comparable with that of silicon. Additionally, most III-V semiconductors have crystalline structures of Wurtzite or Zincblende which are noncentrosymmetric, a feature that does not exist in silicon. This lack of inversion symmetry causes high values of second-order susceptibility $\left(\chi^{(2)}\right)$ in III-V semiconductors [94].

In this thesis, we explore III-V semiconductor nonlinear photonic structures of two different kinds. Specifically, we consider a nonlinear metasurface with the metamolecules organized in a regular 2D array, featuring resonances that enhance and manipulate nonlinear optical interactions. Further, we also look at guided-wave devices such as simple passive nonlinear waveguides of various geometries and observe nonlinear optical interactions existing in such structures.

In the first scenario (*i.e.* Chapters 2 and 3), we explore the potential of AlGaAs with a high value of $\chi^{(2)}$ (and large linear refractive index (n)) for bianisotropic metasurfaces. The high value of n facilitates Mie resonances inside the meta-atoms, which are required for efficient nonlinear light-matter interactions. Finally, we theoretically prove a giant asymmetric second-harmonic

generation for the proposed metasurfaces [112].

As the second scenario of this thesis (*i.e.* Chapters 4 and 5), we explore the potential of a quaternary III-V semiconductor InGaAsP to serve as a nonlinear waveguide platform. In Chapter 4, we develop a MATLAB code for the solution of the coupled nonlinear Schrodinger equations. By solving the equations numerically, we explore the qualitative behavior of the nonlinear waves inside the waveguide. As a specific example, looking at the four-wave mixing nonlinear optical interaction, we explore the generation and propagation of the signal, idler, and pump beams inside a nonlinear optical waveguide. The developed method could be helpful for determining the optimum length of the nonlinear optical interaction *i.e.* the maximum idler generation. It will help in designing waveguides with optimized nonlinear optical interactions. In chapter 5, we consider an InGaAsP three-layer heterostructure for design, fabrication, and optical characterization of passive nonlinear waveguides of two geometries: the $half - core$ and *nanowire* waveguides. We experimentally demonstrate four-wave mixing effect in both kinds of waveguides. Further, we measure an effective value of the nonlinear refractive index in InGaAsP waveguides. This information is still largely missing in literature because there have been very few experiments on the nonlinear optical characterization of InGaAsP. Further, we observe self-phase modulation and measure the two-photon absorption coefficient in InGaAsP waveguides. Finally, Chapter 6 is the concluding chapter that summarizes the achievements of this Ph.D. research and outlines future perspectives.

1.4 Optical Properties of $Al_xGa_{1-x}As$

Aluminum gallium arsenide $Al_xGa_{1-x}As$ is a ternary compound, where the fractions of Al and Ga are interchangeable and $0 \leq x \leq 1$. AlGaAs has a broad transparency window ranging from the near- to mid-infrared (MIR), from 0.9 to 17 μm [113], [114]). Its bandgap energy can be changed by varying the composition of aluminum. For the Al concentration $x < 0.45$, the direct bandgap is maintained, and its value is calculated from $Eg(x) = 1.422 + 1.2475x$, where all numerical coefficients have electron volt (eV) units [115]. At the telecom C-band wavelength range (from 1530 to 1565 nm), the refractive index of $Al_xGa_{1-x}As$ is high, ranging between 2.9 (for $x = 1$) and 3.4 (for $x = 0$). It has been shown in numerous experiments that AlGaAs exhibits large second-order susceptibility $\chi^{(2)} = 200$ pm/V [116], [117] and

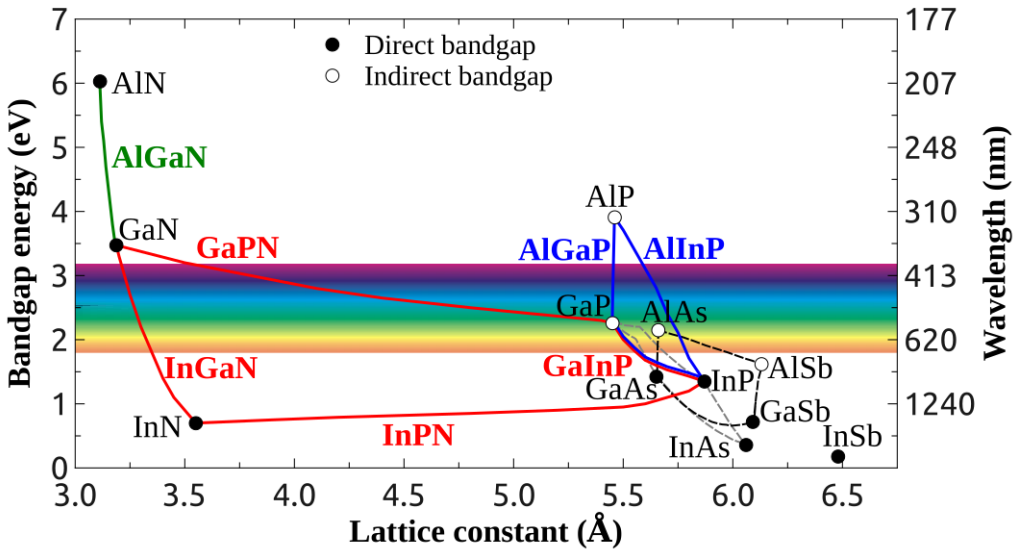

FIGURE 1.2: Bandgap energy of several III-V semiconductor compounds versus the lattice constant. The solid and dashed lines represent compounds with direct and indirect bandgaps, respectively.

nonlinear refractive index $n_2 = 1.5 \times 10^{-13}$ cm^2/W [118].

1.5 Optical properties of $In_{1-x}Ga_xAs_{1-y}P_y$

Indium gallium arsenide phosphide ($In_{1-x}Ga_xAs_{1-y}P_y$) is a quaternary alloy of InP, GaAs, GaP and InAs, where $0 < \{x, y\} < 1$. The band diagram of InGaAsP lattice matched to InP includes conduction band (CB), heavy- and light-holes band as well as split-off band due to consideration of spin-orbit coupling effect [119]. Figure 1.3 shows the band diagram around the Γ valley (where the electron wavevector k is zero) for the InGaAsP compound lattice matched to InP. The bandgap energy, E_g, can be varied as a function of x and y according to [106]

$$E_g(eV) = 0.75 + 0.46y + 0.14y^2. \tag{1.3}$$

The refractive index of InGaAsP changes from 3.2 ($y = 0.9$) to 3.6 ($y = 0.1$) at the Telecom C-band. Any parameter of InGaAsP such as lattice constant

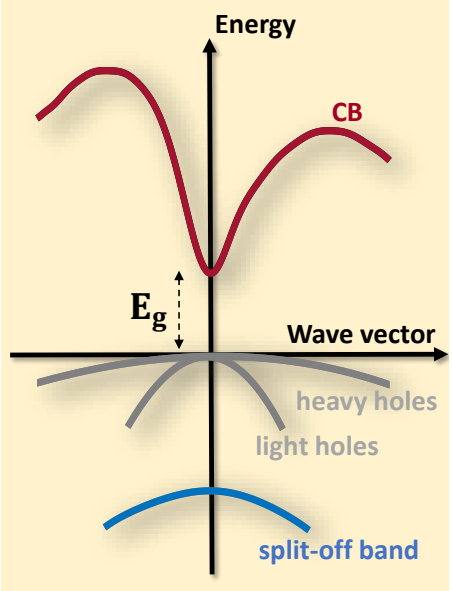

FIGURE 1.3: The band diagram around the Γ valley (where $k = 0$) for the InGaAsP compound lattice matched to InP. The band diagram includes the conduction band (CB), heavy- and light-hole bands, and the split-off band due to spin-orbit coupling effect. The parameter E_g represents the fundamental bandgap energy. The figure is reproduced from Ref. [119].

and bandgap energy can be found through the following approximate equation [119]:

$$b(x,y) = (1-x)y\, b_{\mathrm{InAs}} + (1-x)y\, b_{\mathrm{InP}} + x(1-y)\, b_{\mathrm{GaAs}} + xy\, b_{\mathrm{GaP}}. \quad (1.4)$$

The nonlinear coefficients in InGaAsP are not as well studied as those of AlGaAs. The InGaAsP compound has a high nonlinear refractive index on the order of $10^{-13}\mathrm{cm}^2/\mathrm{W}$ [101]. However, the value of $\chi^{(2)}$ is not reported in the literature, and some references [120], [121] only claim that it is "at least four times larger than that of GaAs". Exploring second-order nonlinearity of InGaAsP could be another open field of research deserving exploration.

Chapter 2

Fundamental principles of nonlinear AlGaAs metasurfaces

In this chapter, we discuss all the theoretical concepts required for the study and exploration of nonlinear bianisotropic AlGaAs metasurfaces, namely second-order nonlinear polarization of AlGaAs, scattering characteristics of an AlGaAs meta-atoms, multipolar decomposition, bianisotropy of an AlGaAs meta-atom as well as the BIC concept. These subjects will be exploited in the following chapter where we demonstrate giant asymmetric second-harmonic generation based on AlGaAs metasurfaces [112].

2.1 Second-order nonlinear optical properties of AlGaAs

Nonlinear optics describes how high-intensity coherent light interacts with a nonlinear medium, inducing the contributions to the medium's polarization scaling as several powers of the light's electric field strength. The induced polarization $(\mathbf{P})$ can be written in terms of the applied electric field $(\mathbf{E})$ as

$$\mathbf{P} = \varepsilon_0 \left[\chi^{(1)}\mathbf{E} + \chi^{(2)}\mathbf{EE} + \chi^{(3)}\mathbf{EEE} + ... \right], \tag{2.1}$$

where ϵ_0 is the permittivity of free space and $\chi^{(1)}$ is a second-rank tensor (3×3 matrix) describing the linear response of the material to the applied optical field. The rest of the terms contribute to the nonlinear response of the material to the applied optical field. The nonlinear coefficient $\chi^{(n)}$ known as n-th order nonlinear susceptibility is a $(n+1)$-rank tensor. In the expanded

form, Eq. (2.1) can be written as [122]

$$P_i = \varepsilon_0 \chi_{ij} E_j + 2\varepsilon_0 d_{ijk} E_j E_k + 4\chi_{ijkl} E_j E_k E_l + ..., \tag{2.2}$$

where P_i and E_i represent the i^{th} component of the induced polarization and the illuminating light, respectively, and $(i, j, k, l) = (x, y, z)$. The nonlinear parameter d is associated with $\chi^{(2)}$ as $2d_{ijk} = \chi^{(2)}_{ijk}$. For a lossless nonlinear medium, since the permutation $\{i, j, k, l\}$ is not important in Eq. (2.2), the number of elements in the d matrix can be reduced. Therefore the second-order polarization can be written in a contracted form as

$$\begin{bmatrix} P_x(2\omega) \\ P_y(2\omega) \\ P_z(2\omega) \end{bmatrix} = 2\varepsilon_0 \begin{bmatrix} d_{11} & d_{12} & d_{13} & d_{14} & d_{15} & d_{16} \\ d_{21} & d_{22} & d_{23} & d_{24} & d_{25} & d_{26} \\ d_{31} & d_{32} & d_{33} & d_{34} & d_{35} & d_{36} \end{bmatrix} \begin{bmatrix} E_x(\omega) E_x(\omega) \\ E_y(\omega) E_y(\omega) \\ E_z(\omega) E_z(\omega) \\ 2E_y(\omega) E_z(\omega) \\ 2E_z(\omega) E_x(\omega) \\ 2E_x(\omega) E_y(\omega) \end{bmatrix}. \tag{2.3}$$

The nonlinear polarization vector for AlGaAs crystal, with a zinc-blende structure and symmetry $\bar{4}3m$, can be obtained as

$$\begin{bmatrix} P_x(2\omega) \\ P_y(2\omega) \\ P_z(2\omega) \end{bmatrix} = 2\varepsilon_0 \begin{bmatrix} 0 & 0 & 0 & d & 0 & 0 \\ 0 & 0 & 0 & 0 & d & 0 \\ 0 & 0 & 0 & 0 & 0 & d \end{bmatrix} \begin{bmatrix} E^2(\omega) \\ E^2(\omega) \\ E^2(\omega) \\ 2E_y(\omega)E_z(\omega) \\ 2E_x(\omega)E_z(\omega) \\ 2E_x(\omega)E_y(\omega) \end{bmatrix}, \tag{2.4}$$

where $d_{14} = d_{25} = d_{36} = d$ and the only nonvanishing elements are $\chi^{(2)}_{xyz} = \chi^{(2)}_{yzx} = \chi^{(2)}_{zxy} = \chi^{(2)}$. Thanks to the large second-order nonlinear susceptibility of AlGaAs ($\chi^{(2)} = 200$ pm/V) [116], [117], it has received much attention in the field of harmonic generation based on nano-particles (nano-antennas) [123]–[130]. In the following next sections of this chapter, we will introduce the concept of dielectric nano-resonators. Next, we derive the multipolar decomposition of the induced current in the meta-atom made of AlGaAs. Following that, we introduce the concept of bianisotropy using a specific AlGaAs meta-atom and describe the fundamentals of the bound states

in the continuum (BIC).

2.2 Dielectric nano-resonators

Subwavelength dielectric scatterers with high permittivity support electric and magnetic resonances based on the Mie theory. When an electric field is applied to a dielectric, it exerts forces on electrons and nuclei in opposite directions. It causes the electron orbits to be extended, resulting in a small electric dipole. This process generates a net charge movement known as displacement current. In contrast to subwavelength metallic scatterers, in dielectric nanoantennas, the resonances are attributed to the displacement current produced by bound electrons, not the free electrons at the surface. This displacement current is the origin of the magnetic response of the dielectric scatterers. The magnetic resonance can be comparable or even stronger than the electric one [131]. These strong magnetic resonances together with the electric ones contribute crucially to the field of nano-optics where the main functionality is the localization of light. Further, they come into play when the light-matter interaction enters the nonlinear regime. Since the second- and third-order nonlinear susceptibilities ($\chi^{(2)}$ and $\chi^{(3)}$, respectively) are very small, the second- ($P^{2\omega}$) and the third-order ($P^{3\omega}$) nonlinear polarization become noticeable only at high light intensities (see Eqs. (2.1) and (2.2)):

$$P^{2\omega} = \varepsilon_0 \sum_{jk} \chi^{(2)}_{ijk} E_j(\omega) E_k(\omega), \tag{2.5}$$

$$P^{3\omega} = \varepsilon_0 \sum_{jkl} \chi^{(3)}_{ijkl} E_j(\omega) E_k(\omega) E_l(\omega). \tag{2.6}$$

Here E and ε_0 represent the local electric field and vacuum permittivity, respectively. Up to now, several studies have been reporting second-harmonic [132]–[135] and third-harmonic generation from single dielectric scatterers [136], [137], see Fig. 2.1.

Another application of dielectric scatterers is to construct a unidirectional pattern of radiation. Based on the Kerker effect [138], it can be demonstrated that a dielectric sphere with the same values of relative permittivity and permeability ($\epsilon = \mu$) shows no backscattering. The same concept, known as the *generalized* Kerker condition can be achieved using the interference of electric and magnetic multipoles for a dielectric scatterer for which by modifying the geometry or dimensions of the scatterer, the resonant wavelength can be

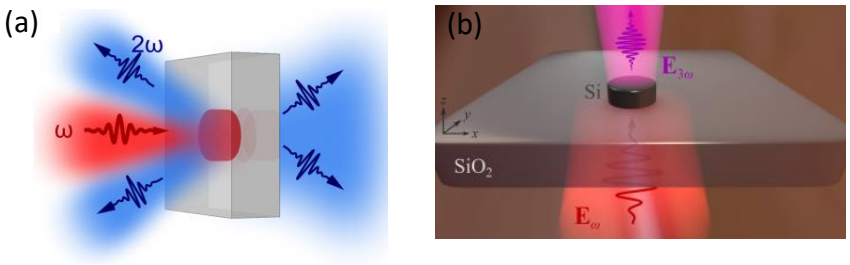

FIGURE 2.1: Schematic of second- and third-harmonic generation from (a) an AlGaAs (the figure is reprinted from [133]) and (b) a silicon scatterer (the figure is reprinted from [136])

readily changed. This concept can even be extended to higher orders of multipoles *i.e.* electric (EQ) and magnetic (MQ) quadrupoles [32]. These electric and magnetic multipoles exhibit even and odd parities, respectively, in terms of phases in radiation. These features can cause destructive interference and unidirectional radiation patterns, see Fig. 2.2. The mentioned effects can even become more significant if the collective effect of several scatterers to be considered. This situation arises when the scatterers are placed in arrays known as optical metasurfaces. Optical metasurfaces are two-dimensional periodic or non-periodic arrangements of optically small scatterers (known as meta-atoms) that are usually located on a very thin substrate. Metasurfaces are well-known for their abilities to manipulate the amplitude, phase, and polarization of reflected, transmitted, absorbed light as well as to convert the wavelength of electromagnetic waves by nonlinear optical phenomena.

Regarding the resonant light-matter interaction, another recently emerged concept known as bound states in the continuum (BIC) has attracted a great deal of attention in the field of metasurfaces. BICs are photonic modes with infinite quality factor (Q) [42], [139], and they facilitate high conversion efficiency for harmonics generation. Several experimental and theoretical works on the second- [44]–[46], [140], [141], third- [142]–[144] and higher-order [47], [145] harmonic generation in dielectric metasurfaces have been published.

Another degree of freedom associated with metasurfaces can be provided by the bianisotropy effect in which the induced electric and magnetic moments are not only dependent on the exciting electric and magnetic fields, respectively, but also dependent on the combination of the exciting fields. Using bianisotropic meta-atoms for a metasurface (*i.e.* bianisotropic metasurface), asymmetric behavior of the interacting light with the metasurface becomes feasible via magnetoelectric coupling. On the basis of bianisotropic

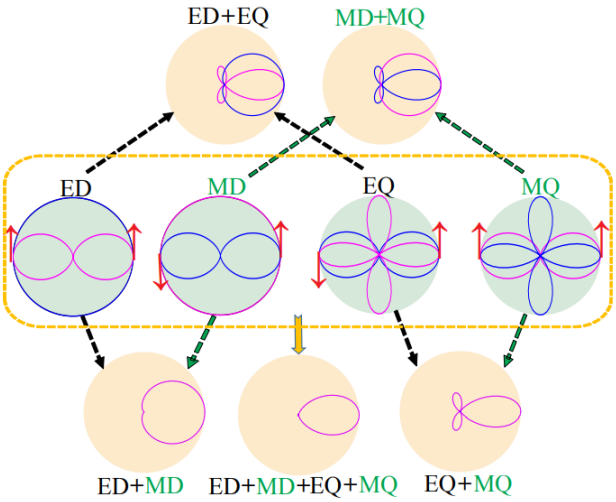

FIGURE 2.2: Radiation pattern for different multipole moments up to quadrupoles and their interference. ED and EQ (MD and MQ) represent electric (magnetic) dipole and quadrupole moments, respectively. The interference of the out-of-phase and in-phase fields demonstrates unidirectional behavior. The incident plane wave illuminates the nanostructure from the left with an in-plane electric field. Purple and blue curves represent in-plane and out-of-plane scattering patterns, respectively. Reprinted with permission from [32] © The Optical Society.

metasurfaces, asymmetric linear functionalities such as asymmetric reflection [146], [147] , asymmetric optical forces [148] , self-isolated Raman lasing [149], light trapping [150], asymmetric absorption [151]–[153] and nonreciprocity [154], [155] have been demonstrated. However, the nonlinear potential of bianisotropic metasurfaces based on bound states in the continuum have remained unexplored.

In this thesis, we propose a dielectric metasurface, made of AlGaAs, that combines nonlinearity, bianisotropy and the BIC concept to obtain very high asymmetric nonlinear behavior [112], see Fig. 2.3. To this end, three conditions must be met. First, it is important to choose an appropriate nonlinear material. Second, one can tailor the electric and magnetic response of the metasurface in terms of the induced multipoles. Third, one must understand BIC and bianisotropy concepts and how to apply them to enhance nonlinear optical interactions. In the next section, we consider AlGaAs as a suitable nonlinear material for nonlinear scattering. Next, we derive the multipolar decomposition of the induced current in the meta-atom. Following that, we introduce the concept of bianisotropy using a specific dielectric meta-atom. Finally, we explain the BIC concept.

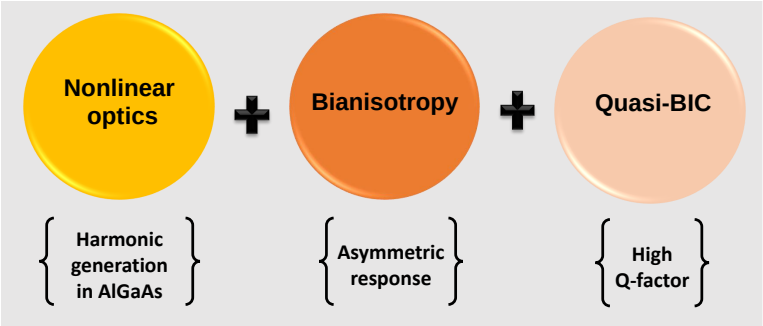

FIGURE 2.3: Schematic representing the idea of our work to enhance asymmetric nonlinear behavior.

2.3 Scattering process

Depending on the wavelength of the illuminating wave, the refractive index of the particle and the host medium, the particles can scatter or absorb light (see Fig. 2.4). The underlying mechanism of scattering is the reradiation (or secondary radiation) from the scatterer, where electric charges inside the scatterer are derived by the illuminating wave and start oscillating (or reradiating) [156]. In elastic scattering, the energy of the wave is conserved, however, the direction of light may change. The total scattered electric field ($\mathbf{E}_{\text{scattered}}$) can be calculated as

$$\mathbf{E}_{\text{scattered}} = \mathbf{E}_{\text{excitation}} + \mathbf{E}_{\text{reradiation}}. \tag{2.7}$$

Generally, due to the absorption caused by the imaginary part of the refractive index, some energy of light is removed and transferred into heat. The total contributions caused by the scattering and absorption can be expressed by the extinction parameter. Another important parameter in scattering is the scattering cross-section which is defined as $C_s = \frac{P_{\text{scattered}}}{I_0}$, where the numerator and denominator denote the total scattered power and the power per unit area of the incident wave, respectively. The scattering cross-section describes how strong the light-matter interaction is.

2.3.1 Mie theory

The scattering process in a cute mathematical form was underpinned by Gustav Mie in 1908 [157]. Mie theory is a powerful theoretical way to solve Maxwell's equations governing the scattering of an electromagnetic plane wave by a homogeneous sphere, see Fig. 2.5. The radius of the particle, the wavelength of the illuminating light, and the particle's and host medium's

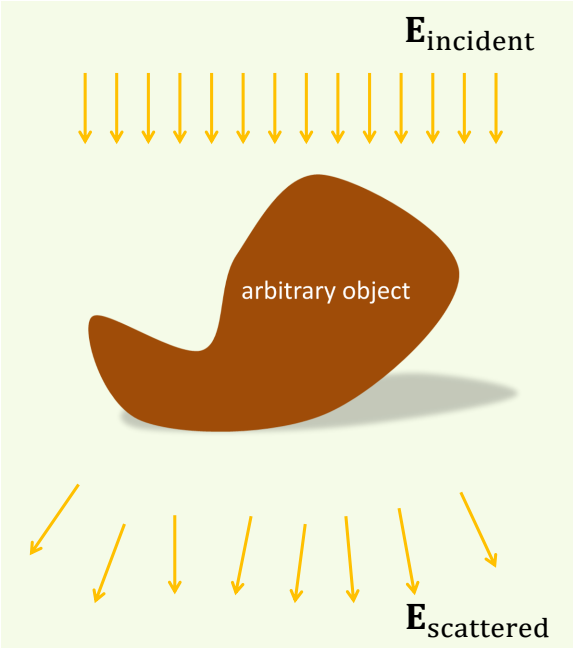

FIGURE 2.4: Schematic of the scattering process for an arbitrary scatterer.

refractive indices are all important parameters for Mie calculations. The particle's radius is assumed to be a fraction of the wavelength of light in size, *i.e.* $S = \frac{2\pi a}{\lambda} \sim 1$, where S is the so-called size parameter. The parameters a and λ denote the particle's radius and the wavelength of the incident wave, respectively.

Since the object is a sphere but the illuminating wave is a plane wave, the basic strategy is to change the system of coordinates to the spherical one and apply the boundary conditions for the inner and outer fields to obtain the scattering coefficients, a_n and b_n. In order to expand the scattered field, vector spherical harmonics (VSHs) *i.e.* the eigenfunctions of the Helmholtz equation in spherical coordinates are used. The expansion coefficients can be obtained in terms of the spherical Bessel (j_n) and Henkel functions of the first kind ($h_n^{(1)}$) as follows [156]:

$$a_n = \frac{\mu_{\text{host}} m^2 j_n(mx)\left[x j_n(x)\right]' - \mu_1 j_n(x)\left[mx j_n(x)\right]'}{\mu_{\text{host}} m^2 j_n(mx)\left[x h_n^{(1)}(x)\right]' - \mu_1 h_n^{(1)}(x)\left[mx j_n(mx)\right]'}, \tag{2.8}$$

$$b_n = \frac{\mu_1 j_n(mx)\left[x j_n(x)\right]' - \mu_{\text{host}} j_n(x)\left[mx j_n(x)\right]'}{\mu_1 j_n(mx)\left[x h_n^{(1)}(x)\right]' - \mu_{\text{host}} h_n^{(1)}(x)\left[mx j_n(mx)\right]'}, \tag{2.9}$$

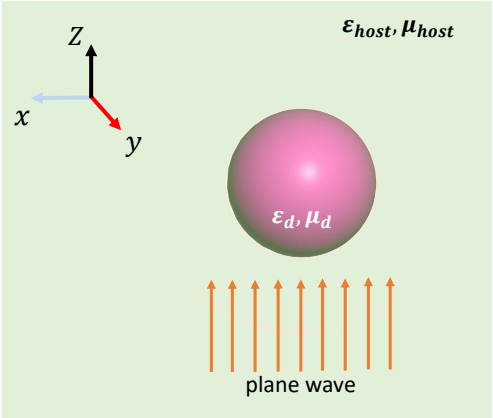

FIGURE 2.5: Schematic of the Mie scattering process for a sphere illuminated by a plane wave. The sphere is embedded in a medium with the permittivity and permeability of $\varepsilon_{\text{host}}$ and μ_{host}, respectively.

where $x = ka = \frac{2\pi n_{\text{host}} a}{\lambda}$ and $m = \frac{n_{\text{host}}}{n_{\text{particle}}}$. The coefficients a_n and b_n are related to electric and magnetic multipoles, respectively. Figure 2.6 shows the patterns of the electric and magnetic fields associated with the two first electric and magnetic Mie coefficients for a spherical particle.

The scattering, extinction, and absorption cross-sections can be calculated as the summation of the scattering coefficients as [156]

$$C_{\text{sca}} = \frac{2\pi}{k^2} \sum_{n=1}^{\infty} (2n+1) \left(|a_n|^2 + |b_n|^2 \right), \tag{2.10}$$

$$C_{\text{ext}} = \frac{2\pi}{k^2} \sum_{n=1}^{\infty} (2n+1)\, Re\,(a_n + b_n), \tag{2.11}$$

$$C_{\text{abs}} = C_{\text{ext}} - C_{\text{sca}}. \tag{2.12}$$

Also, the ratio of the above cross-sections to the geometrical cross-section gives the scattering, extinction, and absorption efficiency factors of the scatterer:

$$Q_{\text{sca}} = \frac{C_{\text{sca}}}{\pi a^2}, \tag{2.13}$$

$$Q_{\text{ext}} = \frac{C_{\text{ext}}}{\pi a^2}, \tag{2.14}$$

$$Q_{\text{abs}} = \frac{C_{\text{abs}}}{\pi a^2}. \tag{2.15}$$

Figure 2.7 shows the individual contribution of the electric and magnetic dipoles and quadrupoles to the scattering cross-section of a sphere with a

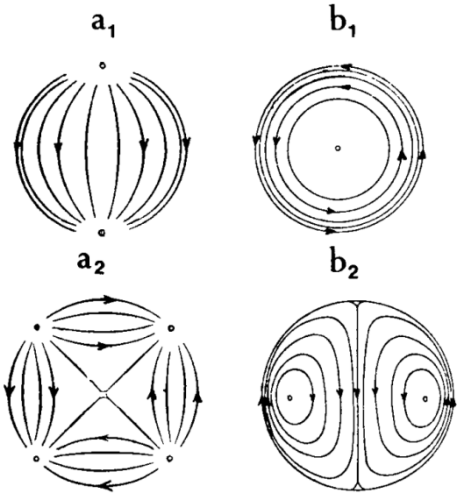

FIGURE 2.6: The patterns of electric and magnetic fields corresponding to the two first Mie coefficients [156], [157]

radius of 220 nm made of $Al_{0.18}Ga_{0.82}As$. We select the composition 18% of Al to avoid the two-photon absorption effect in the meta-atom at the wavelengths of operation. As can be seen from the figure, the total spectrum exhibits sharp resonances, especially for the magnetic quadrupole term (b_2). These sharp resonances are expected to enhance nonlinear optical interactions.

2.4 Multipolar analysis

The analysis of the electric and magnetic fields produced by spatially localized electric charges and currents can be effectively performed using multipole expansion [158], [159]. No matter how complicated the charge and current distributions are, the fields that they generate may be envisaged as the superposition of the fields produced by each multipole. Generally, the light-matter interaction for small scatterers (here meta-atoms) depends on two characteristics: first, the behavior of the individual scatterer illuminated by light, and second, the collective interaction of meta-atoms. In both cases, the analysis can be performed by a multipole decomposition.

The multipole moments of any given meta-atom can be calculated using one of two fundamental methods namely the expansion of the scattered field and the induced current. The outcomes from both strategies are the same. In this thesis, we use the expansion of current to calculate the electric and magnetic multipole moments. However, we also use some conclusions from the former

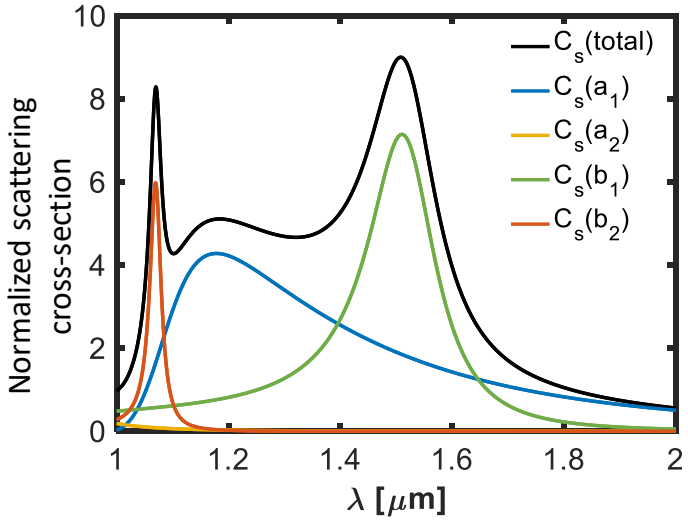

FIGURE 2.7: The scattering cross-section spectrum and multipolar contributions based on Mie theory for an AlGaAs sphere illuminated in z-direction. The radius of the sphere is 220 nm. $C_s\,(a_1)$ and $C_s\,(a_2)$ ($C_s\,(b_1)$ and $C_s\,(b_2)$) represent the contributions to the scattering cross-section due to the electric (magnetic) dipole and quadrupole moments, respectively.

method as well. That is why we briefly discuss the first approach and then we explain the multipole expansion of current in more detail. Before going further, let us describe a simple picture of the scattering process in terms of Maxwell's equations. One can write Maxwell's equations for the total electric and magnetic fields as

$$\begin{cases} \nabla \times \mathbf{E}_t = -i\omega\mu\mathbf{H}_t, \\ \nabla \times \mathbf{H}_t = -i\omega\varepsilon_0\left(\varepsilon_h + \triangle\varepsilon\left(r\right)\right)\mathbf{E}_t, \end{cases} \tag{2.16}$$

in which E_t and H_t are the total electric and magnetic field, respectively, ε_h represents the permittivity of the host medium, and $\triangle\varepsilon\left(r\right) = \varepsilon_d - \varepsilon_h$. In the scattering process, the total electric field is considered as the sum of the incident and scattered field, therefore, the above equations can be written as

$$\begin{cases} \nabla \times \left(\mathbf{E}_\mathrm{inc} + \mathbf{E}_\mathrm{sca}\right) = -i\omega\mu\left(\mathbf{H}_{inc} + \mathbf{H}_\mathrm{sca}\right), \\ \nabla \times \left(\mathbf{H}_\mathrm{inc} + \mathbf{H}_\mathrm{sca}\right) = -i\omega\varepsilon_0\left(\varepsilon_h + \triangle\varepsilon\left(r\right)\right)\left(\mathbf{E}_\mathrm{inc} + \mathbf{E}_\mathrm{sca}\right), \end{cases} \tag{2.17}$$

in which E_inc and E_sca represent the incident field and scattered fields, respectively. Note that for the incident fields, we can write

$$\begin{cases} \nabla \times \mathbf{E}_\mathrm{inc} = -i\omega\mu\mathbf{H}_\mathrm{inc}, \\ \nabla \times \mathbf{H}_\mathrm{inc} = i\omega\varepsilon_0\varepsilon_h\mathbf{E}_\mathrm{inc}. \end{cases} \tag{2.18}$$

Therefore, the scattered fields and the induced current (**J**) can be obtained as

$$\begin{cases} \nabla \times \mathbf{E}_{\text{sca}} = -i\omega\mu\mathbf{H}_{\text{sca}}, \\ \nabla \times \mathbf{H}_{\text{sca}} = i\omega\varepsilon_0 \left(\varepsilon_h + \triangle\varepsilon\left(r\right)\right)\mathbf{E}_{\text{sca}} + i\omega\varepsilon_0\triangle\varepsilon\left(r\right)\mathbf{E}_{\text{inc}}, \\ \nabla \times \mathbf{H}_{\text{sca}} = i\omega\varepsilon_0\varepsilon_h\mathbf{E}_{\text{sca}} + i\omega\varepsilon_0\triangle\varepsilon\left(r\right)\left(\mathbf{E}_{\text{inc}} + \mathbf{E}_{\text{sca}}\right), \end{cases} \tag{2.19}$$

where **J** is defined as

$$\mathbf{J} = i\omega\varepsilon_0\triangle\varepsilon\left(\mathbf{E}_{\text{inc}} + \mathbf{E}_{\text{sca}}\right). \tag{2.20}$$

Equations (2.19) and (2.20) show how the induced current contributes to the scattered fields.

2.4.1 Multipole expansion of the scattered field

The scattered field can be expanded in terms of vector spherical harmonics (VSH) as [156]

$$\mathbf{E}_{\text{sca}}\left(\mathbf{r},\omega\right) = k^2\sum_{n=1}^{\infty}\sum_{m=-n}^{n} E_{nm}\left[a_{nm}\left(\omega\right)\mathbf{N}_{nm}^{(3)}\left(\mathbf{r},\omega\right) + ib_{nm}\left(\omega\right)\mathbf{M}_{nm}^{(3)}\left(\mathbf{r},\omega\right)\right], \tag{2.21}$$

in which a_{nm} and b_{nm} are the scattered field VSH coefficients corresponding to the electric and magnetic multipole moments, respectively. $\mathbf{N}_{nm}^{(3)}$ and $\mathbf{M}_{nm}^{(3)}$ represent the vector spherical harmonics. VSH can be written in terms of Bessel and Hankel functions. The coefficient E_{nm} is calculated as

$$E_{nm} = \left|\mathbf{E}_{\text{inc}}\right|\sqrt{\frac{2n+1}{4\pi}}\sqrt{\frac{(n-m)!}{(n+m)!}}\left(-1\right)^m; \tag{2.22}$$

the multipole coefficients can be calculated through the orthogonality of VSHs as

$$a_{nm} = \frac{\int_0^{2\pi}\int_0^{\pi}\mathbf{E}_{\text{sca}}\left(r=a,\theta,\varphi,\omega\right)\left[\mathbf{N}_{nm}^{(3)}\left(r=a,\theta,\varphi,\omega\right)\right]^*\sin\theta\,\mathrm{d}\theta\,\mathrm{d}\varphi}{k^2E_{nm}\int_0^{2\pi}\int_0^{\pi}\left|\mathbf{N}_{nm}^{(3)}\left(r=a,\theta,\varphi,\omega\right)\right|^2\sin\theta\,\mathrm{d}\theta\,\mathrm{d}\varphi}, \tag{2.23}$$

$$b_{nm} = \frac{\int_0^{2\pi}\int_0^{\pi}\mathbf{E}_{\text{sca}}\left(r=a,\theta,\varphi,\omega\right)\left[\mathbf{M}_{nm}^{(3)}\left(r=a,\theta,\varphi,\omega\right)\right]^*\sin\theta\,\mathrm{d}\theta\,\mathrm{d}\varphi}{ik^2E_{nm}\int_0^{2\pi}\int_0^{\pi}\left|\mathbf{M}_{nm}^{(3)}\left(r=a,\theta,\varphi,\omega\right)\right|^2\sin\theta\,\mathrm{d}\theta\,\mathrm{d}\varphi}. \tag{2.24}$$

In this approach, to calculate a_{nm} and b_{nm}, the scattered field ($\mathbf{E}_{\text{sca}}$) is required to be calculated first numerically e.g. by COMSOL.

2.4.2 Multipole expansion of current

A spatially localized electric current density ($\mathbf{J}(\mathbf{r},t)$) in momentum space can be written as [160]

$$\begin{aligned}\mathbf{J}(r,t) &= \mathrm{Re}\left[\frac{1}{\sqrt{2\pi}}\int_{0^+}^{\infty} e^{-i\omega t}\mathbf{J}_\omega(\mathbf{r})\,\mathrm{d}\omega\right] \\ &= \mathrm{Re}\left[\frac{1}{\sqrt{2\pi}}\int_{0^+}^{\infty} e^{-i\omega t}\int \frac{\mathrm{d}^3\mathbf{p}}{\sqrt{(2\pi)^3}}\mathbf{J}_\omega(\mathbf{p})\,e^{i\mathbf{p}.\mathbf{r}}\right]. \end{aligned} \tag{2.25}$$

The orthonormal bases (multipolar functions) in momentum space are defined as

$$\mathbf{X}_{jm}(\hat{\mathbf{p}}) = \frac{1}{\sqrt{j(j+1)}}\mathbf{L}Y_{jm}, \tag{2.26}$$

$$\mathbf{Z}_{jm}(\hat{\mathbf{p}}) = i\hat{\mathbf{p}}\times\mathbf{X}_{jm}(\hat{\mathbf{p}}), \tag{2.27}$$

$$\mathbf{W}_{jm}(\hat{\mathbf{p}}) = \hat{\mathbf{p}}Y_{jm}(\hat{\mathbf{p}}), \tag{2.28}$$

where $\mathbf{L} = \frac{1}{i}(\mathbf{r}\times\nabla)$ represents the angular momentum operator. Y_{jm} and j_j denote the spherical harmonics and spherical Bessel functions, respectively. Now, let us call the part of $\mathbf{J}$ satisfying the condition $|p| = \frac{\omega}{c}$ as $\mathbf{J}^{'}$. Then this part can be written in terms of the basis as

$$\mathbf{J}^{'} = \sum_{jm} a_{jm}\mathbf{Z}_{jm}(\hat{\mathbf{p}}) + b_{jm}\mathbf{X}_{jm}(\hat{\mathbf{p}}) + c_{jm}\mathbf{W}_{jm}(\hat{\mathbf{p}}), \tag{2.29}$$

where a_{jm} and b_{jm} correspond to the transversal electromagnetic wave radiated by $\mathbf{J}^{'}$. The coefficient c_{jm} is related to the longitudinal part of the radiated field which is zero (because the electromagnetic wave is transversal). Therefore, the multipole decomposition can be performed by a_{jm} and b_{jm}, known as electric and magnetic multipole coefficients. These coefficients can be found by projection as

$$a_{jm} = <Z_{jm}\left|J^{'}\right.> = \int \mathrm{d}\hat{\mathbf{p}}\ \mathbf{Z}_{jm}^{\dagger}\mathbf{J}^{'}(\hat{\mathbf{p}}), \tag{2.30}$$

$$b_{jm} = <X_{jm}\left|J^{'}\right.> = \int \mathrm{d}\hat{\mathbf{p}}\ \mathbf{Z}_{jm}^{\dagger}\mathbf{J}^{'}(\hat{\mathbf{p}}), \tag{2.31}$$

where

$$\mathbf{J}^{'}(\hat{\mathbf{p}}) = \frac{1}{\sqrt{(2\pi)^3}} \int \mathrm{d}^3\mathbf{r}\, \mathbf{J}_\omega(\mathbf{r})\, e^{-i\frac{\omega}{c}\hat{\mathbf{p}}.\mathbf{r}}. \tag{2.32}$$

Therefore, equations (2.30) and (2.31) in the momentum and coordinate space can be written as [159]

$$\frac{\sqrt{(2\pi)^3}}{4\pi} a_{jm} = \sum_{\bar{l}\bar{m}} (-i)^{\bar{l}} \int \mathrm{d}\hat{\mathbf{p}}\, \mathbf{Z}^{\dagger}_{jm}(\hat{\mathbf{p}})\, Y_{\bar{l}\bar{m}}(\hat{\mathbf{p}}) \int \mathrm{d}^3\mathbf{r}\, \mathbf{J}_\omega(\mathbf{r})\, Y^{*}_{\bar{l}\bar{m}}(\hat{\mathbf{r}})\, j_{\bar{l}}(kr)\,, \tag{2.33}$$

$$\frac{\sqrt{(2\pi)^3}}{4\pi} b_{jm} = \sum_{\bar{l}\bar{m}} (-i)^{\bar{l}} \int \mathrm{d}\hat{\mathbf{p}}\, \mathbf{X}^{\dagger}_{jm}(\hat{\mathbf{p}})\, Y_{\bar{l}\bar{m}}(\hat{\mathbf{p}}) \int \mathrm{d}^3\mathbf{r}\, \mathbf{J}_\omega(\mathbf{r})\, Y^{*}_{\bar{l}\bar{m}}(\hat{\mathbf{r}})\, j_{\bar{l}}(kr)\,. \tag{2.34}$$

The only nonvanishing terms in Eqs. (2.33) and (2.34) are $\bar{l} = j-1, j+1$ and $\bar{l} = j$, respectively [160]. Note that $j = 1$ and $j = 2$ represent the dipole and quadrupole terms, respectively.

In the next sections, we explain some exact formulations for the electric and magnetic multipole moments in both spherical and Cartesian coordinates using Eqs. (2.33) and (2.34). Here, the multipolar moments are derived up to the quadrupolar terms. These multipolar moments will become crucial later in determining the polarizabilities and the corresponding contributions to the reflection coefficients.

Electric dipole moment

The electric dipole moment *i.e.* $j = 1$ or $\bar{l} = \{0, 2\}$ can be written as [160]

$$\begin{bmatrix} a_{11} \\ a_{10} \\ a_{1-1} \end{bmatrix}_{j=1} = \begin{bmatrix} a_{11} \\ a_{10} \\ a_{1-1} \end{bmatrix}_{\bar{l}=0} + \begin{bmatrix} a_{11} \\ a_{10} \\ a_{1-1} \end{bmatrix}_{\bar{l}=2} = -\frac{1}{\pi\sqrt{3}} \int d^3\mathbf{r}\mathbf{J} j_0(kr)$$
$$-\frac{k^2}{2\pi\sqrt{3}} \int d^3\mathbf{r} \left[3\left(\mathbf{r}^{\dagger}\mathbf{J}(\mathbf{r})\right)\mathbf{r} - r^2\mathbf{J}(\mathbf{r})\right] \frac{j_2(kr)}{(kr)^2}. \tag{2.35}$$

Now, let us represent the current and the position vectors in the spherical basis as

$$\mathbf{J} = \begin{bmatrix} J_1 \\ J_0 \\ J_{-1} \end{bmatrix}, \quad \mathbf{r} = \begin{bmatrix} r_1 \\ r_0 \\ r_{-1} \end{bmatrix}. \tag{2.36}$$

Note that these quantities are represented in Eq. (2.36) in spherical basis, not in spherical-polar basis. A spherical basis is required for describing spherical tensors in terms of complex numbers and standard bases (*i.e.* $\mathbf{e}_x$, $\mathbf{e}_y$ and $\mathbf{e}_z$, see Appendix A for the relation between these two types of bases).

If we write the separate components of Eq. (2.35) explicitly, we obtain:

$$\begin{aligned} a_{11} \;=\; & -\frac{1}{\pi\sqrt{3}} \int \mathrm{d}^3\mathbf{r}\, J_1 j_0\left(kr\right) + \frac{k^2}{2\pi\sqrt{3}} \int \mathrm{d}^3\mathbf{r} \left[3r_1^2 J_{-1} - 3r_0 r_1 J_0 \right. \\ & \left. + J_1 \left(r_0^2 + r_{-1} r_0 \right) \right] \frac{j_2\left(kr\right)}{\left(kr\right)^2}, \end{aligned} \tag{2.37}$$

$$\begin{aligned} a_{10} \;=\; & -\frac{1}{\pi\sqrt{3}} \int \mathrm{d}^3\mathbf{r}\, J_0 j_0\left(kr\right) + \frac{k^2}{2\pi\sqrt{3}} \int \mathrm{d}^3\mathbf{r} \left[3r_{-1} r_0 J_1 + 3r_0 r_1 J_{-1} \right. \\ & \left. - 2J_0 \left(r_0^2 + r_{-1} r_0 \right) \right] \frac{j_2\left(kr\right)}{\left(kr\right)^2}, \end{aligned} \tag{2.38}$$

$$\begin{aligned} a_{1-1} \;=\; & -\frac{1}{\pi\sqrt{3}} \int \mathrm{d}^3\mathbf{r}\, J_{-1} j_0\left(kr\right) + \frac{k^2}{2\pi\sqrt{3}} \int \mathrm{d}^3\mathbf{r} \left[J_{-1} \left(r_0^2 + r_{-1} r_0 \right) \right. \\ & \left. - 3r_{-1} r_0 J_0 + 3J_1 r_{-1}^2 \right] \frac{j_2\left(kr\right)}{\left(kr\right)^2}. \end{aligned} \tag{2.39}$$

On the other hand, the induced electric ($\mathbf{p}$) and magnetic dipole ($\mathbf{m}$) moments in Cartesian coordinates can be determined in terms of a_{nm} and b_{nm} as [158]

$$\mathbf{p} = \begin{bmatrix} p_x \\ p_y \\ p_z \end{bmatrix} = C_1^e \begin{bmatrix} \frac{(a_{1-1} - a_{11})}{\sqrt{2}} \\ \frac{(a_{1-1} + a_{11})}{\sqrt{2}i} \\ a_{10} \end{bmatrix}, \tag{2.40}$$

therefore, the Cartesian components can be obtained as

$$p_x = \frac{-1}{i\omega}\left\{\int \mathrm{d}^3\mathbf{r}\, J_x j_0(kr) + \frac{k^2}{2}\int \mathrm{d}^3\mathbf{r}\left[3(\mathbf{r}.\mathbf{J})\,x - r^2 J_x\right]\frac{j_2(kr)}{(kr)^2}\right\}, \tag{2.41}$$

$$p_y = \frac{-1}{i\omega}\left\{\int \mathrm{d}^3\mathbf{r}\, J_y j_0(kr) + \frac{k^2}{2}\int \mathrm{d}^3\mathbf{r}\left[3(\mathbf{r}.\mathbf{J})\,y - r^2 J_y\right]\frac{j_2(kr)}{(kr)^2}\right\}, \tag{2.42}$$

$$p_z = \frac{-1}{i\omega}\left\{\int \mathrm{d}^3\mathbf{r}\, J_z j_0(kr) + \frac{k^2}{2}\int \mathrm{d}^3\mathbf{r}\left[3(\mathbf{r}.\mathbf{J})\,z - r^2 J_z\right]\frac{j_2(kr)}{(kr)^2}\right\}, \tag{2.43}$$

where $C_1^e = \frac{\sqrt{3}\pi}{i\omega}$ can be calculated by comparing the expanded scattered field to the multipole moments in the far field (when $kr \to \infty$).

Magnetic dipole moment

The magnetic dipole moment *i.e.*, $j = 1$ or $\bar{l} = \{1\}$, can be obtained as

$$\begin{bmatrix} b_{11} \\ b_{10} \\ b_{1-1} \end{bmatrix}_{j=1} = \begin{bmatrix} b_{11} \\ b_{10} \\ b_{1-1} \end{bmatrix}_{\bar{l}=1}$$

$$= -\frac{\sqrt{3}k}{2\pi}\int \mathrm{d}^3\mathbf{r}\;\mathbf{r}\times\mathbf{J}(kr)\,\frac{j_1(kr)}{kr}. \tag{2.44}$$

On the other hand, the induced magnetic dipole ($\mathbf{m}$) moments can be determined in terms of a_{nm} and b_{nm} as [158]

$$\mathbf{m} = \begin{bmatrix} m_x \\ m_y \\ m_z \end{bmatrix} = C_1^m \begin{bmatrix} \frac{(b_{1-1}-b_{11})}{\sqrt{2}} \\ \frac{(b_{1-1}+b_{11})}{\sqrt{2}i} \\ b_{10} \end{bmatrix}. \tag{2.45}$$

If we write out the separate terms of Eq. (2.44), we obtain

$$b_{11} = -\frac{\sqrt{3}k}{2\pi}\int \mathrm{d}^3\mathbf{r}\,(\mathbf{r}\times\mathbf{J})_1\,\frac{j_1(kr)}{kr}, \tag{2.46}$$

$$b_{10} = -\frac{\sqrt{3}k}{2\pi}\int \mathrm{d}^3\mathbf{r}\,(\mathbf{r}\times\mathbf{J})_0\,\frac{j_1(kr)}{kr}, \tag{2.47}$$

$$b_{1-1} = -\frac{\sqrt{3}k}{2\pi}\int \mathrm{d}^3\mathbf{r}\,(\mathbf{r}\times\mathbf{J})_{-1}\,\frac{j_1(kr)}{kr}. \tag{2.48}$$

The multipoles components in Cartesian coordinate can be obtained from Eq. (2.45) as

$$m_x = \frac{3}{2}\int \mathrm{d}^3\mathbf{r}\,(\mathbf{r}\times\mathbf{J})_x\,\frac{j_1(kr)}{kr}, \tag{2.49}$$

$$m_y = \frac{3}{2}\int \mathrm{d}^3\mathbf{r}\,(\mathbf{r}\times\mathbf{J})_y\,\frac{j_1(kr)}{kr}, \tag{2.50}$$

$$m_z = \frac{3}{2}\int \mathrm{d}^3\mathbf{r}\,(\mathbf{r}\times\mathbf{J})_z\,\frac{j_1(kr)}{kr}, \tag{2.51}$$

where $C_1^m = \frac{-\sqrt{3}\pi}{k}$ can be calculated by comparing the expanded scattered field to the formulations of the multipole moments in the far field (when $kr \to \infty$).

Magnetic quadrupole moment

Equation (2.34) (for $j = 2$, or $\bar{l} = j = 2$) can be used to calculate the magnetic quadrupole moment in spherical coordinates. It yields

$$b_{2m} = \frac{4\pi}{\sqrt{(2\pi)^3}}\sum_{\bar{m}=-2}^{2}\int \mathrm{d}\hat{\mathbf{p}}\;\mathbf{X}_{2m}^{\dagger}(\hat{\mathbf{p}})\,Y_{2\bar{m}}(\hat{\mathbf{p}})\int \mathrm{d}^3\mathbf{r}\,\mathbf{J}_\omega(\mathbf{r})\,Y_{2\bar{m}}^{*}(\hat{\mathbf{r}})\,j_2(kr)\,. \tag{2.52}$$

Using the above equation, we get

$$b_{22} = \sqrt{\frac{5}{2\pi^2}}\int \mathrm{d}^3\mathbf{r}\hat{r}_1\,(J_1\hat{r}_0 - J_0\hat{r}_1)\,j_2(kr)\,, \tag{2.53}$$

$$b_{21} = \sqrt{\frac{5}{4\pi^2}}\int \mathrm{d}^3\mathbf{r}\,[\hat{r}_1\,(J_1\hat{r}_{-1} - J_{-1}\hat{r}_1) + \hat{r}_0\,(J_1\hat{r}_0 - J_0\hat{r}_1)]\,j_2(kr)\,, \tag{2.54}$$

$$b_{20} = \sqrt{\frac{15}{4\pi^2}} \int \mathrm{d}^3\mathbf{r}\hat{r}_0 \left(J_1\hat{r}_{-1} - J_{-1}\hat{r}_1\right) j_2\left(kr\right), \tag{2.55}$$

$$b_{2-1} = \sqrt{\frac{5}{4\pi^2}} \int \mathrm{d}^3\mathbf{r} \left[\hat{r}_{-1}\left(J_1\hat{r}_{-1} - J_{-1}\hat{r}_1\right) + \hat{r}_0\left(J_0\hat{r}_{-1} - J_{-1}\hat{r}_0\right)\right] j_2\left(kr\right), \tag{2.56}$$

$$b_{2-2} = \sqrt{\frac{5}{2\pi^2}} \int \mathrm{d}^3\mathbf{r}\hat{r}_{-1}\left(J_0\hat{r}_{-1} - J_{-1}\hat{r}_0\right) j_2\left(kr\right). \tag{2.57}$$

Next, we utilize the following transformation between the spherical and Cartesian coordinates to express the magnetic quadrupole moments in Cartesian coordinates [158]:

$$Q^m_{xx} = C^m_2 \left[\frac{b_{22} + b_{2-2}}{2} - \frac{1}{\sqrt{6}} b_{20}\right], \tag{2.58}$$

$$Q^m_{xy} = Q^m_{yx} = C^m_2 \left[\frac{b_{2-2} b_{22}}{2i}\right], \tag{2.59}$$

$$Q^m_{xz} = Q^m_{zx} = C^m_2 \left[\frac{b_{2-1} b_{21}}{2}\right], \tag{2.60}$$

$$Q^m_{yz} = Q^m_{zy} = C^m_2 \left[\frac{b_{2-1} b_{21}}{2i}\right], \tag{2.61}$$

$$Q^m_{yy} = C^m_2 \left[-\left(\frac{b_{22} + b_{2-2}}{2}\right) - \frac{1}{\sqrt{6}} b_{20}\right], \tag{2.62}$$

$$Q^m_{zz} = -Q^m_{xx} - Q^m_{yy}, \tag{2.63}$$

in which $C^m_2 = \frac{6\pi\sqrt{10}}{ik^2}$. Note that Q^m is a symmetric and traceless tensor, therefore the number of quadrupolar moments reduces to five independent components. By substituting Eqs. (2.53)–(2.57) into Eqs. (2.58)–(2.63), the magnetic quadrupolar moments in Cartesian coordinate can be obtained as

$$Q^m_{xx} = 15 \int \mathrm{d}^3\mathbf{r} \left\{x\left(\mathbf{r} \times \mathbf{J}\right)_x + x\left(\mathbf{r} \times \mathbf{J}\right)_x\right\} \frac{j_2\left(kr\right)}{\left(kr\right)^2}, \tag{2.64}$$

$$Q_{xy}^{m} = 15 \int \mathrm{d}^3\mathbf{r} \left\{ x \left(\mathbf{r} \times \mathbf{J}\right)_y + y \left(\mathbf{r} \times \mathbf{J}\right)_x \right\} \frac{j_2 \left(kr\right)}{\left(kr\right)^2}, \tag{2.65}$$

$$Q_{xz}^{m} = 15 \int \mathrm{d}^3\mathbf{r} \left\{ x \left(\mathbf{r} \times \mathbf{J}\right)_z + z \left(\mathbf{r} \times \mathbf{J}\right)_x \right\} \frac{j_2 \left(kr\right)}{\left(kr\right)^2}, \tag{2.66}$$

$$Q_{yy}^{m} = 15 \int \mathrm{d}^3\mathbf{r} \left\{ y \left(\mathbf{r} \times \mathbf{J}\right)_y + y \left(\mathbf{r} \times \mathbf{J}\right)_y \right\} \frac{j_2 \left(kr\right)}{\left(kr\right)^2}, \tag{2.67}$$

$$Q_{yz}^{m} = 15 \int \mathrm{d}^3\mathbf{r} \left\{ y \left(\mathbf{r} \times \mathbf{J}\right)_z + z \left(\mathbf{r} \times \mathbf{J}\right)_x \right\} \frac{j_2 \left(kr\right)}{\left(kr\right)^2}, \tag{2.68}$$

$$Q_{zz}^{m} = 15 \int \mathrm{d}^3\mathbf{r} \left\{ z \left(\mathbf{r} \times \mathbf{J}\right)_z + z \left(\mathbf{r} \times \mathbf{J}\right)_z \right\} \frac{j_2 \left(kr\right)}{\left(kr\right)^2}. \tag{2.69}$$

Electric quadrupole moment

Equation (2.33) (for $j = 2$ or $\bar{l} = \{1,3\}$) can be used to calculate the electric quadrupole moment in spherical coordinates. Therefore, we obtain

$$a_{2m} = a_{em}^{\bar{l}=1} + a_{em}^{\bar{l}=3}, \tag{2.70}$$

where

$$a_{2m}^{\bar{l}=1} = -\frac{4\pi i}{\sqrt{\left(2\pi\right)^3}} \sum_{\bar{m}=-1}^{1} \int \mathrm{d}\hat{\mathbf{p}}\, \mathbf{Z}_{2m}^{\dagger} \left(\hat{\mathbf{p}}\right) Y_{1\bar{m}} \left(\hat{\mathbf{p}}\right) \int \mathrm{d}^3\mathbf{r}\, \mathbf{J}_{\omega} \left(\mathbf{r}\right) Y_{1\bar{m}}^{*} \left(\hat{\mathbf{r}}\right) j_1 \left(kr\right), \tag{2.71}$$

$$a_{2m}^{\bar{l}=3} = -\frac{4\pi i}{\sqrt{\left(2\pi\right)^3}} \sum_{\bar{m}=-1}^{1} \int \mathrm{d}\hat{\mathbf{p}}\, \mathbf{Z}_{2m}^{\dagger} \left(\hat{\mathbf{p}}\right) Y_{3\bar{m}} \left(\hat{\mathbf{p}}\right) \int \mathrm{d}^3\mathbf{r}\, \mathbf{J}_{\omega} \left(\mathbf{r}\right) Y_{3\bar{m}}^{*} \left(\hat{\mathbf{r}}\right) j_1 \left(kr\right). \tag{2.72}$$

Here, we show the process for $\bar{l} = 1$, and we only mention the final result for the case $\bar{l} = 3$. After some algebraic manipulation, we get

$$a_{22}^{\bar{l}=1} = \frac{3ki}{\pi\sqrt{10}} \int \mathrm{d}^3\mathbf{r} \left(J_1 r_1\right) \frac{j_1 \left(kr\right)}{kr}, \tag{2.73}$$

$$a_{21}^{\bar{l}=1} = \frac{3ki}{\pi\sqrt{10}}\frac{1}{\sqrt{2}}\int \mathrm{d}^3\mathbf{r}\,(J_1 r_0 + J_0 r_1)\,\frac{j_1(kr)}{kr}, \tag{2.74}$$

$$a_{20}^{\bar{l}=1} = \frac{3ki}{\pi\sqrt{10}}\frac{1}{\sqrt{6}}\int \mathrm{d}^3\mathbf{r}\,(J_1 r_{-1} + J_{-1} r_1 + 2J_0 r_0)\,\frac{j_1(kr)}{kr}, \tag{2.75}$$

$$a_{2-1}^{\bar{l}=1} = \frac{3ki}{\pi\sqrt{10}}\frac{1}{\sqrt{2}}\int \mathrm{d}^3\mathbf{r}\,(J_{-1} r_0 + J_0 r_{-1})\,\frac{j_1(kr)}{kr}, \tag{2.76}$$

$$a_{2-2}^{\bar{l}=1} = \frac{3ki}{\pi\sqrt{10}}\int \mathrm{d}^3\mathbf{r}\,(J_{-1} r_{-1})\,\frac{j_1(kr)}{kr}. \tag{2.77}$$

We utilize the following transformation between spherical and Cartesian coordinates to get the electric quadrupole moments in Cartesian coordinates [158]:

$$Q_{xx}^e = C_2^e\left[\frac{a_{22}+a_{2-2}}{2} - \frac{1}{\sqrt{6}}a_{20}\right], \tag{2.78}$$

$$Q_{xy}^e = Q_{yx}^e = C_2^e\left[\frac{a_{2-2}-a_{22}}{2i}\right], \tag{2.79}$$

$$Q_{xz}^e = Q_{zx}^e = C_2^e\left[\frac{a_{2-1}-a_{21}}{2}\right], \tag{2.80}$$

$$Q_{yz}^e = Q_{zy}^e = C_2^e\left[\frac{a_{2-1}-a_{21}}{2i}\right], \tag{2.81}$$

$$Q_{yy}^e = C_2^e\left[-\left(\frac{a_{22}+a_{2-2}}{2}\right) - \frac{1}{\sqrt{6}}a_{20}\right], \tag{2.82}$$

$$Q_{zz}^e = -Q_{xx}^e - Q_{yy}^e, \tag{2.83}$$

in which $C_2^e = \frac{6\pi\sqrt{10}}{ck^2}$. Note that Q^e is a symmetric and traceless tensor, therefore the number of quadrupolar moments reduces to five independent components. The same approach can be used for $\bar{l} = 3$. By substituting Eqs. (2.73)– (2.77) into Eqs (2.78)– (2.83), the total electric quadrupolar moments (also adding the corresponding terms for $\bar{l} = 3$) in Cartesian coordinates can be obtained in the general form as

$$Q^{e}_{\alpha\beta} = Q^{e(\bar{l}=1)}_{\alpha\beta} + Q^{e(\bar{l}=3)}_{\alpha\beta}, \tag{2.84}$$

where

$$Q^{e(\bar{l}=1)}_{\alpha\beta} = -\frac{3}{i\omega}\left\{\int \mathrm{d}^3\mathbf{r}\left[3\left(r_\beta J_\alpha + r_\alpha J_\beta\right) - 2\left(\mathbf{r}.\mathbf{J}\right)\delta_{\alpha\beta}\right]\right\}\frac{j_1\left(kr\right)}{kr}, \tag{2.85}$$

$$Q^{e(\bar{l}=3)}_{\alpha\beta} = -\frac{6k^2}{i\omega}\left\{\int \mathrm{d}^3\mathbf{r}\left[5r_\alpha r_\beta\left(\mathbf{r}.\mathbf{J}\right) - \left(r_\alpha J_\beta + r_\beta J_\alpha\right)r^2 - r^2\left(\mathbf{r}.\mathbf{J}\right)\delta_{\alpha\beta}\right]\right\}\frac{j_3\left(kr\right)}{\left(kr\right)^3}, \tag{2.86}$$

in which $\alpha, \beta = \{x, y, z\}$.

2.4.3 Scattering cross-section in terms of electric and magnetic multipoles

The total scattering cross-section of a scatterer in terms of multipolar decomposition can be written as [159]

$$\begin{aligned} \mathrm{C}_{sca}\left(\text{total}\right) \;=\; & \frac{k^4}{6\pi\varepsilon_0\left|E_{inc}\right|^2}\left[\sum\left(\left|p_\alpha\right|^2 + \left|\frac{m_\alpha}{c}\right|^2\right)\right. \\ & \left. + \frac{1}{120}\sum\left(\left|kQ^e_\alpha\right|^2 + \left|\frac{Q^m_\alpha}{c}\right|^2\right)\right], \end{aligned} \tag{2.87}$$

where $\alpha = \{x, y, z\}$. Figure 2.8 shows the contribution of each multipole to the scattering cross-section of a disk-shaped scatterer made of $Al_{0.18}Ga_{0.82}As$. The scatterer is illuminated by an x-polarized light with the k vector directed toward the z-direction. The multipoles are calculated numerically by COMSOL through Eqs. (2.41)–(2.43), (2.49)–(2.51), (2.64)–(2.69) and (2.85)–(2.86).

2.5 Bianisotropy

Dielectric materials in optics can be characterized by their polarizabilities. Putting it in simple terms, the polarizability is the coefficient of proportionality between the induced electric or magnetic multipoles and the exciting electric or magnetic fields. For an isotropic scatterer, the relation between the

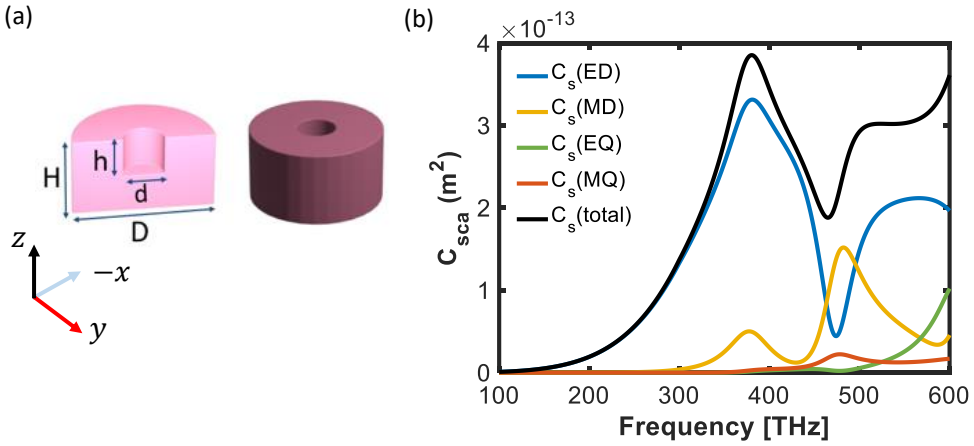

FIGURE 2.8: (a) Schematic of the scatterer with a coaxial cylindrical hole and its cross-sectional view with the geometrical dimensions. The geometrical dimensions are $d = 150$ nm, $D = 300$ nm, $h = 75$ nm, $H = 150$ nm (b) $C_s\,(ED)$ and $C_s\,(EQ)$ ($C_s\,(MD)$ and $C_s\,(MQ)$) represent the contribution of the scattering cross-section due to the electric (magnetic) dipole and quadrupole moments, respectively.

induced electric and magnetic dipoles and the exciting fields can be written as [161], [162]

$$\mathbf{p} = \varepsilon_0 \alpha_{ee}.\mathbf{E}_{\text{loc}}, \tag{2.88}$$

$$\mathbf{m} = \alpha_{mm}.\mathbf{H}_{\text{loc}}, \tag{2.89}$$

where α_{ee}, α_{mm} are scalar quantities representing electric-electric and magnetic-magnetic polarizability. $\mathbf{E}_{\text{loc}}$ and $\mathbf{H}_{\text{loc}}$ represent the local Electric and magnetic fields. On the other hand, the above relations for an anisotropic scatterer are written in the same form but with tensor polarizabilities of $\bar{\bar{\alpha}}_{ee}$ and $\bar{\bar{\alpha}}_{mm}$ which are 3×3 matrices. In contrast to isotropic and anisotropic scatterers, the induced electric and magnetic multipoles in bianisotropic scatterers are not only dependent on the exciting electric ($\mathbf{E}$) and magnetic ($\mathbf{H}$) fields individually, but they are also affected by both $\mathbf{E}$ and $\mathbf{H}$ simultaneously. In this regard, assuming a deeply subwavelength scatterer, the only induced moments are electric and magnetic dipole moments, which can be expressed as

$$\mathbf{p} = \varepsilon_0 \bar{\bar{\alpha}}_{ee}.\mathbf{E}_{\text{loc}} + \varepsilon_0 \eta \bar{\bar{\alpha}}_{em}.\mathbf{H}_{\text{loc}}, \tag{2.90}$$

$$\mathbf{m} = \eta^{-1}\bar{\bar{\alpha}}_{me}.\mathbf{E}_{\text{loc}} + \bar{\bar{\alpha}}_{mm}.\mathbf{H}_{\text{loc}}, \tag{2.91}$$

where $\bar{\bar{\alpha}}_{me}$ and $\bar{\bar{\alpha}}_{em}$ are electric-magnetic and magnetic-electric polarizability tensors. The scatterer is called bianisotropic when the coefficients $\bar{\bar{\alpha}}_{me}$ and $\bar{\bar{\alpha}}_{em}$ are nonzero. The parameter η represents the impedence of free space and is equal to $\sqrt{\mu_0/\varepsilon_0} = 376.73$. The above equations can be expressed in a matrix form as

$$\begin{pmatrix} \frac{p_x}{\varepsilon_0} \\ \frac{p_y}{\varepsilon_0} \\ \frac{p_z}{\varepsilon_0} \\ \eta m_x \\ \eta m_y \\ \eta m_z \end{pmatrix} = \begin{pmatrix} \alpha_{ee}^{xx} & \alpha_{ee}^{xy} & \alpha_{ee}^{xz} & \alpha_{em}^{xx} & \alpha_{em}^{xy} & \alpha_{em}^{xz} \\ \alpha_{ee}^{yx} & \alpha_{ee}^{yy} & \alpha_{ee}^{yz} & \alpha_{em}^{yx} & \alpha_{em}^{yy} & \alpha_{em}^{yz} \\ \alpha_{ee}^{zx} & \alpha_{ee}^{zy} & \alpha_{ee}^{zz} & \alpha_{em}^{zx} & \alpha_{em}^{zy} & \alpha_{em}^{zz} \\ \alpha_{me}^{xx} & \alpha_{me}^{xy} & \alpha_{me}^{xz} & \alpha_{mm}^{xx} & \alpha_{mm}^{xy} & \alpha_{mm}^{xz} \\ \alpha_{me}^{yx} & \alpha_{me}^{yy} & \alpha_{me}^{yz} & \alpha_{mm}^{yx} & \alpha_{mm}^{yy} & \alpha_{mm}^{yz} \\ \alpha_{me}^{zx} & \alpha_{me}^{zy} & \alpha_{me}^{zz} & \alpha_{mm}^{zx} & \alpha_{mm}^{zy} & \alpha_{mm}^{zz} \end{pmatrix} \begin{pmatrix} E_x \\ E_y \\ E_z \\ \eta H_x \\ \eta H_y \\ \eta H_z \end{pmatrix}. \tag{2.92}$$

Note that the polarizability matrix is the characteristic of the scatterer, and it is only dependent on the material and geometry of the scatterer.

To fundamentally understand how the joint contribution of the exciting electric and magnetic fields emerge in the induced electric and magnetic dipoles, we consider the electromagnetic behavior of an Ω-twisted (helix) scatterer made of metal or dielectric, see Fig. 2.9.

Let us assume that a plane wave propagating in the z-direction illuminates the scatterer. Based on Fig. 2.9, the electric field in the x-direction (E_x) induces dipole moment of p_x in the straight part of the scatterer. Also, a current is generated due to p_x giving rise to the current flow in the loop-shape part of the scatterer. This current induces a magnetic dipole moment in the x-direction (m_x). These induced electric and magnetic dipole moments are related to α_{ee}^{xx} and α_{me}^{xx}, respectively. See the inset in Fig. 2.9 to understand the meaning of each superscript and subscript for the polarizability. Other components of the polarizability tensor can be obtained when different polarization of the electric field is applied. For a y-polarized electric field, the magnetic component induces a magnetic dipole moment in the x-direction (m_x). Due to the Lenz's law, a current flows in the loop that generates an electric dipole in the straight part of the scatterer. These induced magnetic

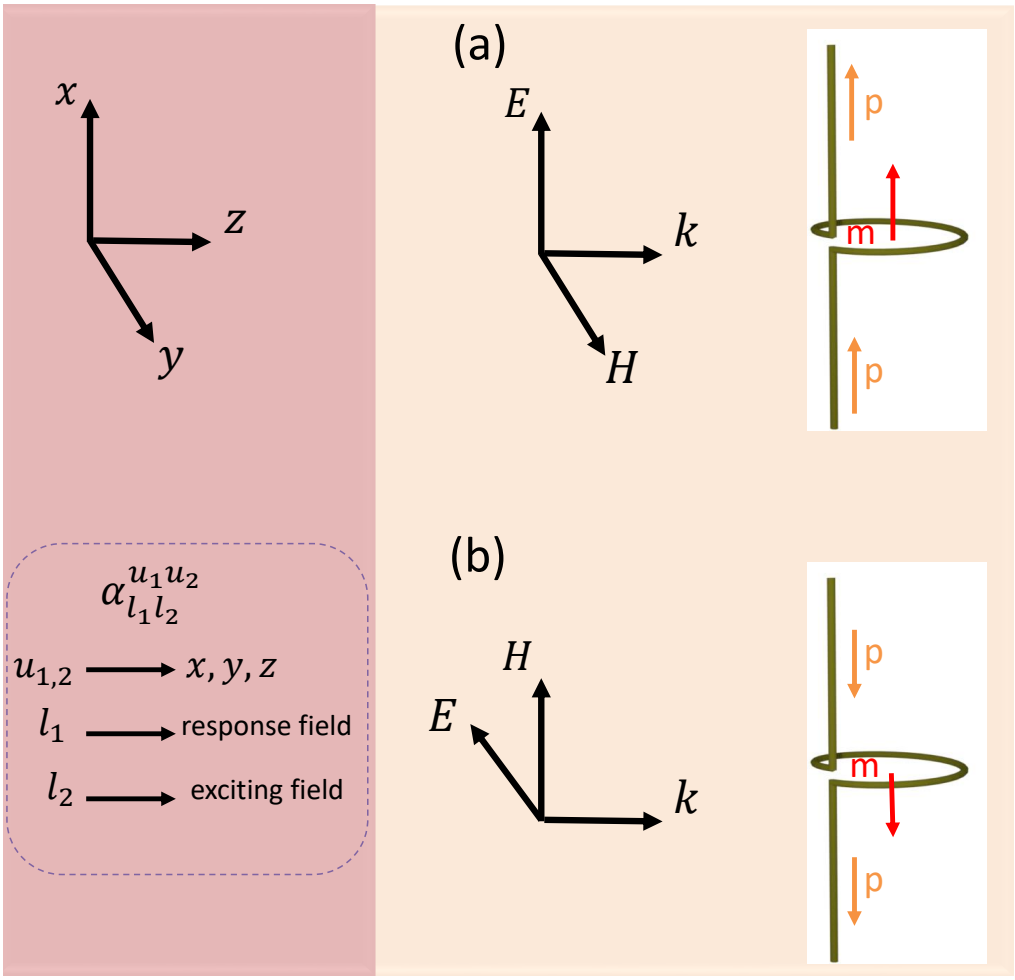

FIGURE 2.9: Schematic of a helical (Ω-twisted) scatterer made of dielectric illuminated by (a) x-polarized and (b) y-polarized light. The inset shows the notation for the polarizability. The superscript and subscript represent the axes and the fields, respectively.

and electric dipole moments are related to α_{mm}^{xx} and α_{em}^{xx}, respectively. Finally, the total polarizability tensor can be expressed as

$$\begin{bmatrix} \overline{\overline{\alpha}}_{ee} & \overline{\overline{\alpha}}_{em} \\ \overline{\overline{\alpha}}_{me} & \overline{\overline{\alpha}}_{mm} \end{bmatrix} = \begin{bmatrix} \begin{pmatrix} \alpha_{ee}^{xx} & 0 & 0 \\ 0 & 0 & 0 \\ 0 & 0 & 0 \end{pmatrix} & \begin{pmatrix} \alpha_{em}^{xx} & 0 & 0 \\ 0 & 0 & 0 \\ 0 & 0 & 0 \end{pmatrix} \\ \begin{pmatrix} -\alpha_{em}^{xx} & 0 & 0 \\ 0 & 0 & 0 \\ 0 & 0 & 0 \end{pmatrix} & \begin{pmatrix} \alpha_{mm}^{xx} & 0 & 0 \\ 0 & 0 & 0 \\ 0 & 0 & 0 \end{pmatrix} \end{bmatrix}. \tag{2.93}$$

For dielectric meta-atoms, by violating the inversion symmetry, a strong bianisotropic response can be obtained. Biasotropic metasurfaces have previously shown asymmetric linear optical functions. Further, Alaee, *et al*. demonstrated how breaking an all-dielectric meta-atom's symmetry causes bianisotropy, which allows a geometrically controllable magnetoelectric coupling, see Fig. 2.10 [148]. An array of these meta-atoms produces different reflection phases, see Fig. 2.11. Interestingly, this bianisotropic meta-atom can provide a 2π phase change in the reflection spectrum for the forward and backward illuminations.

2.5.1 Calculation of polarizability tensor

First, let us assume that an x-polarized plane wave directed in z-direction as $E_x = E_0 e^{-ik_z z}$ illuminates the scatterer. It induces electric and magnetic moments p^+ and m^+ inside the scatterer. Next, assuming an x-polarized plane wave directed in $(-z)$-direction as $E_x = E_0 e^{+ik_z z}$, we obtain the induced electric and magnetic moments p^- and m^- inside the scatterer, see blue triads in Fig. 2.12. Note that there is a π phase shift between the magnetic fields of the forward and backward illumination. Therefore, for the matrix equation (2.92), one can obtain [163]

$$\begin{cases} p_x^+ = \varepsilon_0 \alpha_{ee}^{xx} E_0 + \varepsilon_0 \eta \alpha_{em}^{xy} H_0 \\ p_y^+ = \varepsilon_0 \alpha_{ee}^{yx} E_0 + \varepsilon_0 \eta \alpha_{em}^{yy} H_0 \\ p_z^+ = \varepsilon_0 \alpha_{ee}^{zx} E_0 + \varepsilon_0 \eta \alpha_{em}^{zy} H_0 \\ m_x^+ = \eta^{-1} \alpha_{me}^{xx} E_0 + \alpha_{mm}^{xy} H_0 \\ m_y^+ = \eta^{-1} \alpha_{me}^{yx} E_0 + \alpha_{mm}^{yy} H_0 \\ m_z^+ = \eta^{-1} \alpha_{me}^{zx} E_0 + \alpha_{mm}^{zy} H_0 \end{cases} \tag{2.94}$$

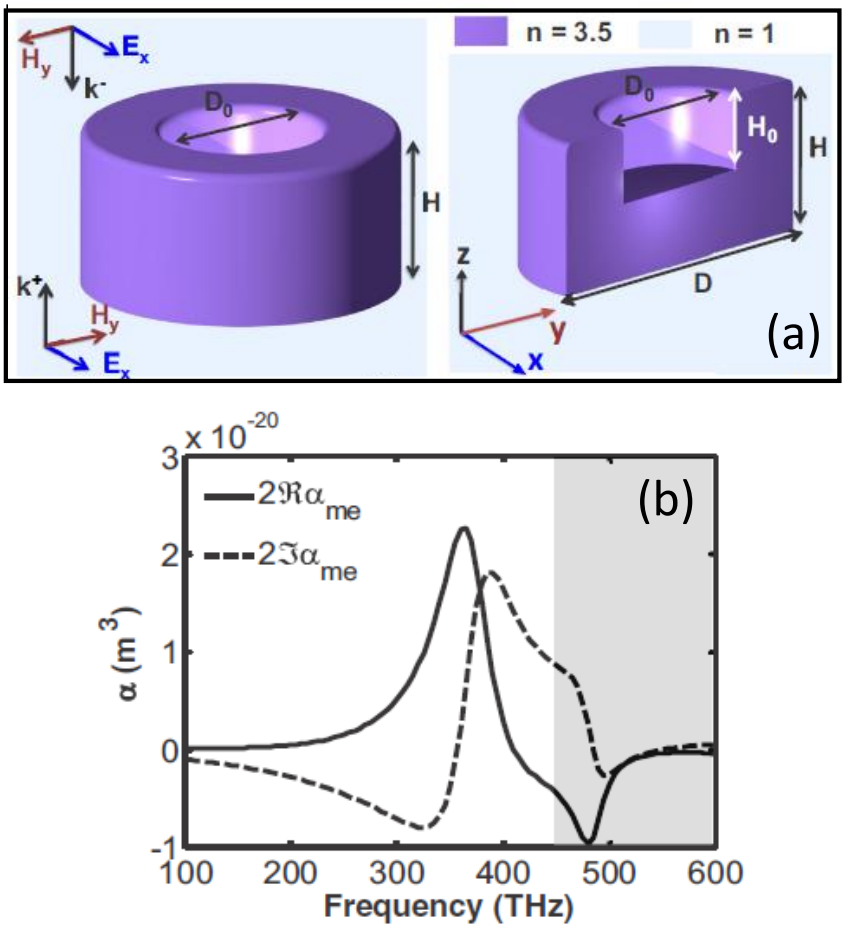

FIGURE 2.10: (a) Schematic of the scatterer (or the meta-atom) with a coaxial cylindrical hole and its cross-sectional view with the geometrical dimensions. The meta-atom is made of silicon. The geometrical dimensions are $d = 150$ nm, $D = 300$ nm, $h = 75$ nm, $H = 150$ nm. (b) Real and imaginary parts of the magnetoelctric polarizability. The figure is reprinted from [148].

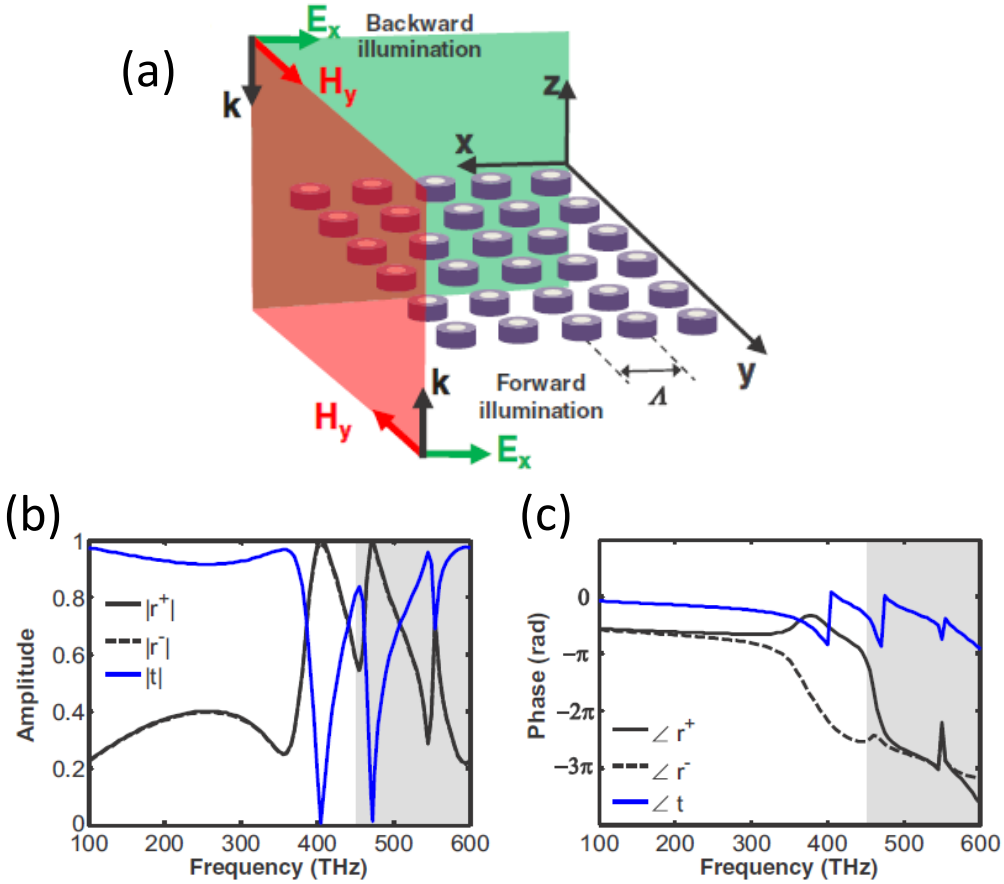

FIGURE 2.11: (a) Schematic of an array of meta-atoms (metasurface) made of the meta-atom shown in Fig 2.10. The metasurface is illuminated from $+z$ (forward) and $-z$ (backward) direction. (b) The amplitude of reflection ($|r^+|$ and $|r^-|$) and the transmission ($|t|$) spectrum for opposite illumination directions shown in (a). The forward and backward amplitudes are denoted by $(+)$ and $(-)$ superscripts. (c) The same plots as in (b), but for the respective phases. The figure is reprinted from [148].

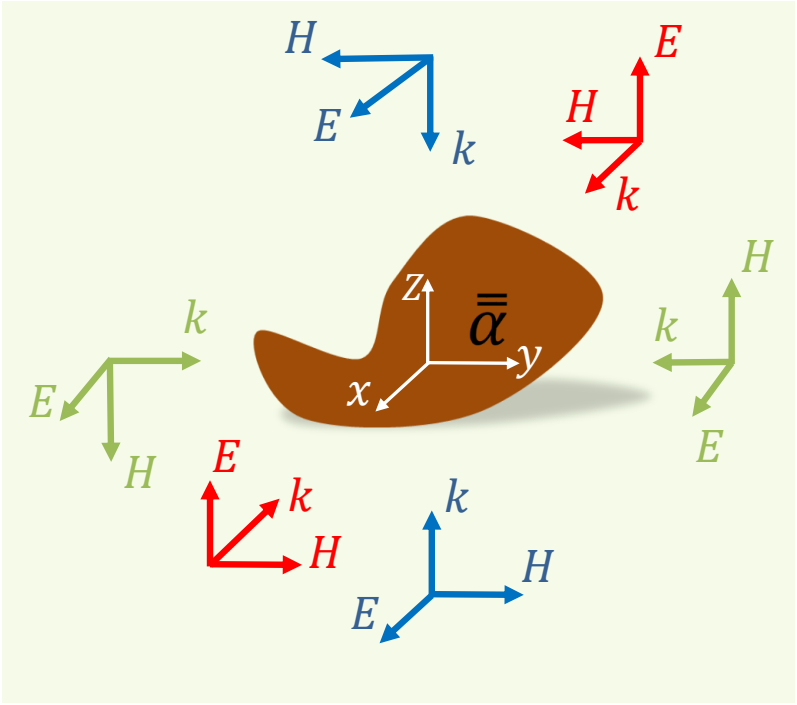

FIGURE 2.12: Schematic of the scatterer and different excitation directions to retrieve all the components of the polarizability tensor ($\bar{\bar{\alpha}}$). Note that the coordinates with the same color have magnetic fields in opposite directions.

$$\begin{cases} p_x^- = \varepsilon_0 \alpha_{ee}^{xx} E_0 - \varepsilon_0 \eta \alpha_{em}^{xy} H_0 \\ p_y^- = \varepsilon_0 \alpha_{ee}^{yx} E_0 - \varepsilon_0 \eta \alpha_{em}^{yy} H_0 \\ p_z^- = \varepsilon_0 \alpha_{ee}^{zx} E_0 - \varepsilon_0 \eta \alpha_{em}^{zy} H_0 \\ m_x^- = \eta^{-1} \alpha_{me}^{xx} E_0 - \alpha_{mm}^{xy} H_0 \\ m_y^- = \eta^{-1} \alpha_{me}^{yx} E_0 - \alpha_{mm}^{yy} H_0 \\ m_z^- = \eta^{-1} \alpha_{me}^{zx} E_0 - \alpha_{mm}^{zy} H_0 \end{cases} . \tag{2.95}$$

Adding and subtracting each multipole component with its counterpart in the opposite direction yields

$$\alpha_{ee}^{ix} = \frac{p_i^+ + p_i^-}{2\varepsilon_0}, \ \alpha_{em}^{iy} = \frac{p_i^+ - p_i^-}{2\varepsilon_0}, \tag{2.96}$$

$$\alpha_{me}^{ix} = \frac{m_i^+ + m_i^-}{2}\eta, \ \alpha_{mm}^{iy} = \frac{m_i^+ - m_i^-}{2}\eta, \tag{2.97}$$

where $i = x, y$ and z. Other components of the polarizability tensor can be obtained by different propagation directions of the illuminating light, *e.g.* the red and green triads in Fig. 2.12.

Based on the above equations, the dipole moments can be calculated numerically through COMSOL Multiphysics. We solve a scattered field problem in the frequency domain with COMSOL using perfectly-matched layer (PML) boundary conditions. We find the solution for two illumination scenarios by a plane wave in the $+z$ and $-z$ direction. After that, the polarizabilities can be obtained from Eqs. (2.96) and (2.97). The absolute values of the electric and magnetic fields of the illuminating light are assumed to be 1 and $1/\eta$, respectively. Figure 2.13 shows the retrieved polarizabilities for a meta-atom made of $Al_{0.18}Ga_{0.82}As$ illuminated by x-polarized light. The geometrical dimensions are $H = 150$ nm, $D = 300$ nm, $h = 75$ nm and $d = 150$ nm. As can be seen from the figure, the magnetoelectric polarizability is nonzero and comparable with the electric-electric and magnetic-magnetic polarizabilities. Therefore, the meta-atom demonstrates the bianisotropy effect. The magnetoelectric coupling can be adjusted by altering the meta-atom's geometrical properties, such as the height h or the diameter d.

2.6 Bound states in the continuum (BICs)

The idea of bound state in the continuum (BIC) was first proposed by John von Neumann and Eugene Wigner in 1929 [42], [139] in the context of quantum mechanics. Although here we want to explain optical bound states in the continuum (not quantum mechanical ones), it would be pedagogical to start with a quantum mechanical example.

Let us start with the Schrodinger equation (in reduced units) [164]

$$\left(-\frac{1}{2}\nabla^2 + V\right)\psi = E\psi, \tag{2.98}$$

in which ψ, E, and V represent the wave function, energy, and potential, respectively. The solution ψ to the Schrodinger equation describes the probability of finding a particle with energy E in the presence of potential V. Eq. (2.98) can be simply rewritten as

$$V = E + \frac{1}{2}\left[\frac{\nabla^2\psi}{\psi}\right]. \tag{2.99}$$

A possible solution for Eq. (2.99) can be expressed as

$$\psi_0(r) = \frac{\sin(kr)}{kr},\ E = \frac{1}{2}k^2, \tag{2.100}$$

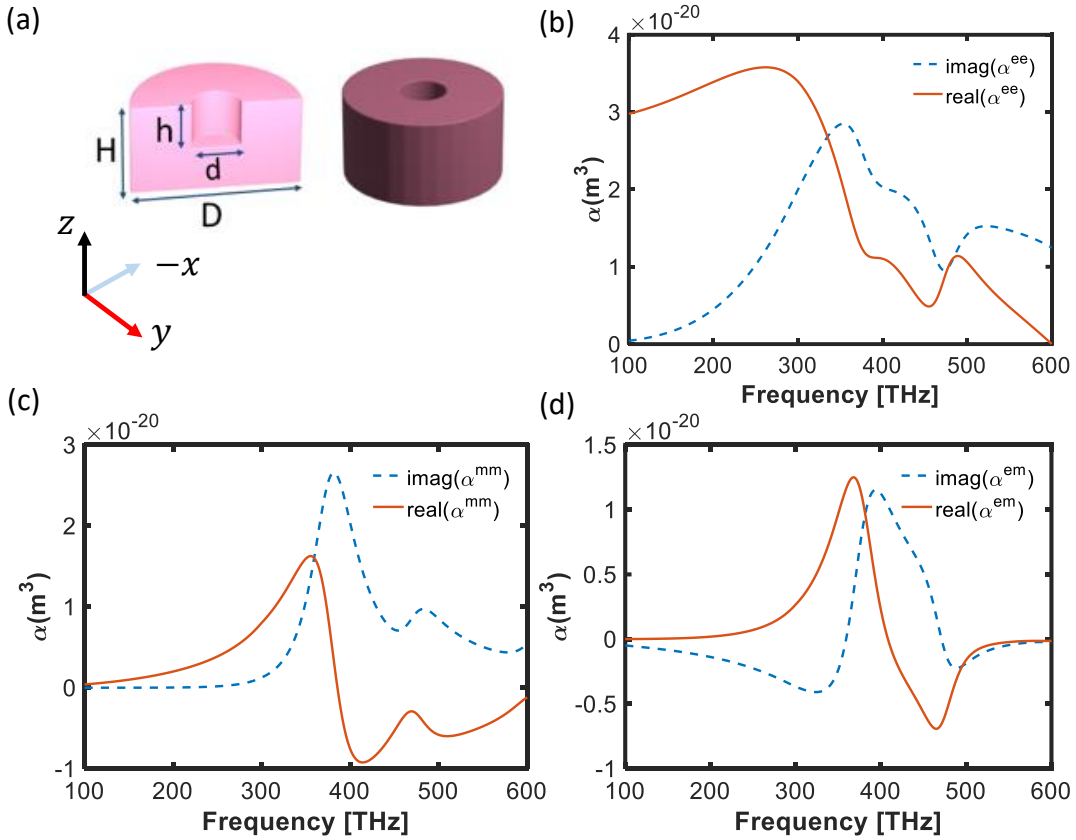

FIGURE 2.13: (a) Schematic of the scatterer (or the meta-atom) with a coaxial cylindrical hole and its cross-sectional view with the geometrical dimensions. The meta-atom is made of AlGaAs. The geometrical dimensions are $d = 150$ nm, $D = 300$ nm, $h = 75$ nm, $H = 150$ nm. (b–d) show the real and imaginary parts of the electric-electric, magnetic-magnetic and electric-magnetic polarizabilities, respectively. As can be seen from (c), the magnetoelectric coupling is nonzero and comparable with the coefficients α^{ee} and α^{mm}.

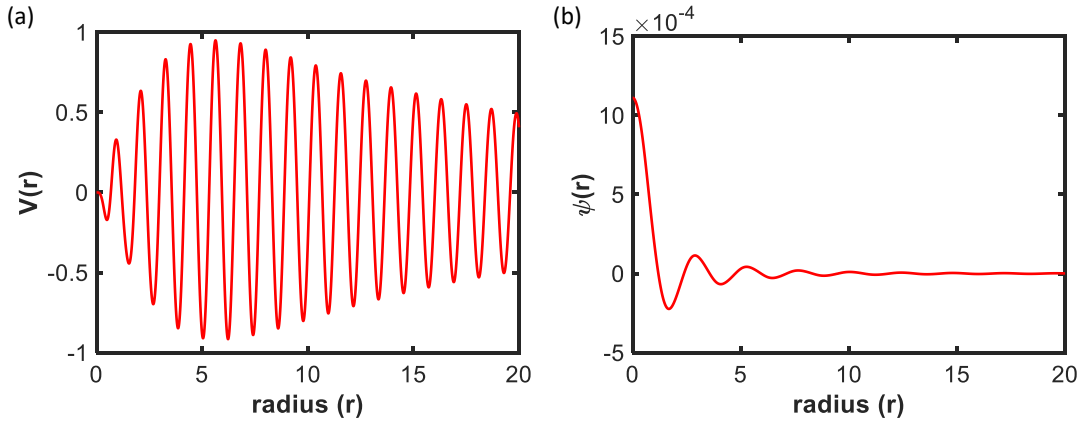

FIGURE 2.14: (a) The applied oscillating potential with the maximum around unity. (b) The bounded wave function obtained for the parameter values $A = 30$, $k = \sqrt{7}$, and $E = 3.5$.

where $V = 0$. However, this solution to the Schrodinger equation is not integrable. In their seminal work, Neumann and Wigner demonstrated that the solution in the form

$$\psi(r) = \psi_0(r) f(r) \tag{2.101}$$

which is the amplitude-modulated version of Eq. (2.100) can be introduced as an integrable solution. Next, the function $f(r)$ was defined as

$$f(r) = \left\{ A^2 + [2kr - \sin(2kr)]^2 \right\}^{-1}, \tag{2.102}$$

in which A is a constant. The potential $V(r)$ can be expressed as

$$\begin{aligned} V(r) &= -\frac{64k^2A^2sin^4(kr)}{\left[A^2 + (2kr - sin(2kr))^2\right]^2} \\ &\quad + \frac{48k^2sin^4(kr) - 8k^2(2kr - sin(2kr))sin(2kr)}{A^2 + (2kr - sin(2kr))^2}. \end{aligned} \tag{2.103}$$

Figure 2.14 shows the potential and the wave function for the parameter values $A = 30$, $k = \sqrt{7}$, $E = 3.5$. As can be seen from part (b) of Fig. 2.14, the bound state can be obtained for the values of E larger than the maximum of the potential (~ 1), *i.e.*, which represents a bound state in the continuum.

Let us now have a comparison between the quantum mechanical picture and optics. Let us assume a quantum well with some discrete bound energy eigenstates. Above the maximum potential, the continuum of states exists, see Fig. 2.15 (a). A similar case can be considered in optics using a three-layer slab waveguide. To find the dispersion diagram, the Helmholtz equation with proper boundary conditions should be solved and three different regions *i.e.* discrete guided mode, forbidden region, and continuum can be defined, see Fig. 2.15 (b). The similarity between the quantum and optical systems can further be understood through a comparison of the Schrodinger equation

$$-\frac{\hbar^2}{2m}\nabla^2\psi + V(x)\,\psi = E\psi \tag{2.104}$$

and Helmholtz equation

$$\nabla^2\psi + \left(k_0^2 n^2 - \beta^2\right)\psi = 0, \tag{2.105}$$

where β is the propagation constant in the z-direction, and $\hbar$, m, and E are the reduced Planck constant, the mass of the particle, and the energy eigenvalue, respectively. Equations (2.104) and (2.105) give rise to discrete energy levels and discrete propagation constants, respectively. In the quantum well, bound states exist when $E < \max\{V\}$, while the guided mode in the waveguide occurs when $n_{\text{cladding}} < n_{\text{effective}} < n_{\text{core}}$. Therefore, the bound state in the continuum for a waveguide is defined as a mode that is above the light line $\omega = c_2\beta$ (where $c_2 = c/n_2$ and c is the speed of light in vacuum), however, it still remains localized (or bounded), see Fig. 2.15. Interestingly, for the optical case, the bound state can be obtained for waveguides with specific geometry and dimensions. For example, it has been earlier obtained for photonic crystal waveguides [165]–[167].

BICs are generally divided into two types, namely *symmetry-protected* and *resonance-trapped* (Friedrich-Wintgen) BICs. These modes exhibit infinite lifetime or equivalently an infinite quality factor. In the former, the normal radiation to the free space is prohibited due to the symmetry incompatibility between the discrete BIC mode and the continuum (a small breaking of the meta-atom symmetry provides a leakage channel to the free space). This is the reason why it is called symmetry-protected. In the latter, the radiation to the free space is hindered by a destructive interference of out-of-plane waves.

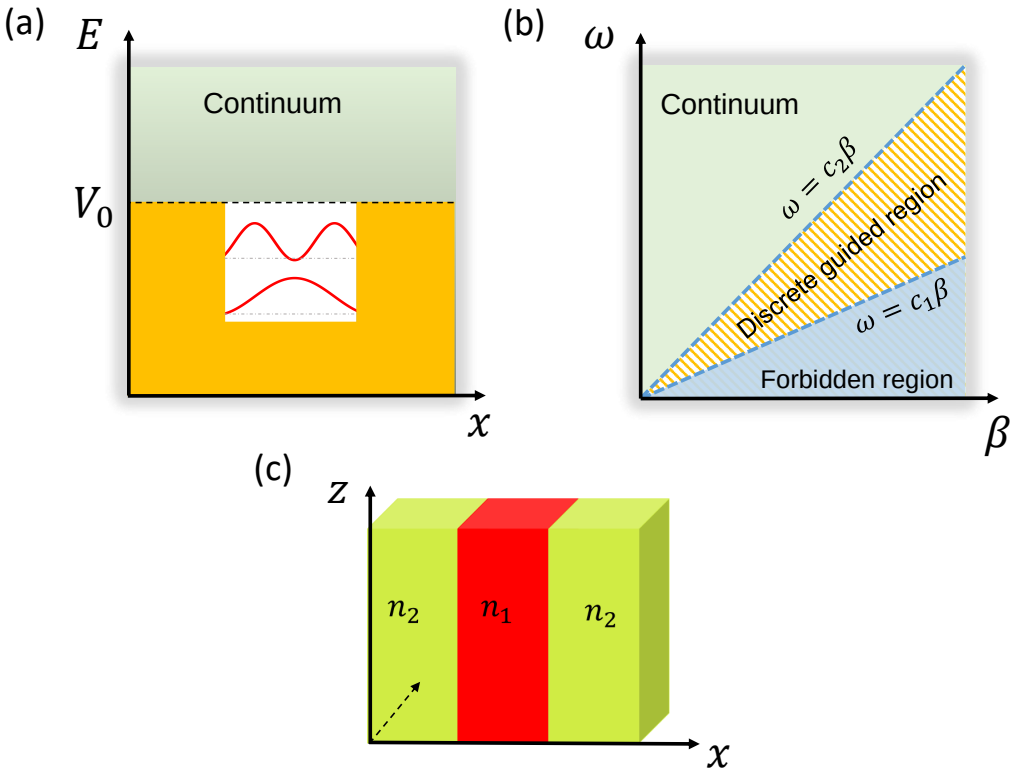

FIGURE 2.15: (a) The energy diagram for a quantum well with a constant applied potential (V_0). It shows some discrete eigenstates (red curves) and the continuum (the light green region). (b) The dispersion diagram for a three-layer slab waveguide showing discrete guided mode, forbidden region and the continuum. c_1 and c_2 represent c/n_1 and c/n_2, where n_1 and n_2 are the refractive indices of the core and claddings, respectively.

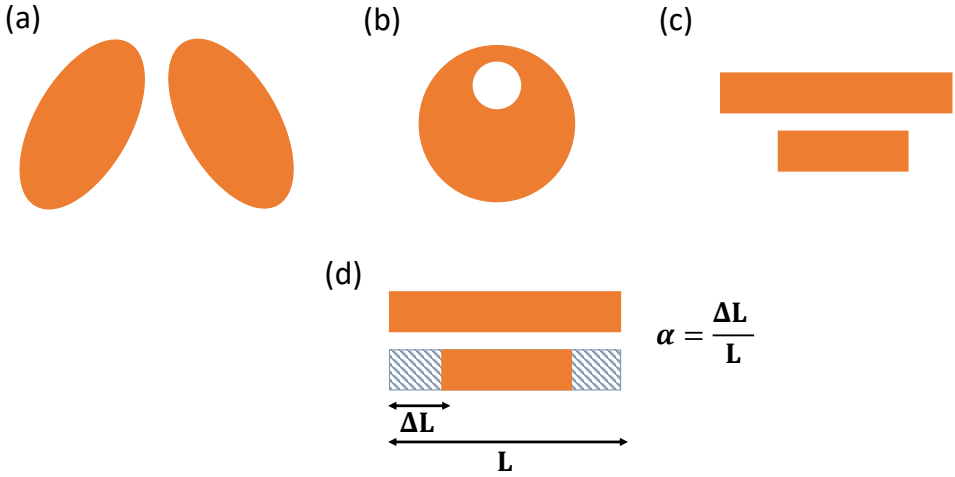

FIGURE 2.16: (a)–(c) Schematic of different shapes (top view) of meta-atoms exhibiting symmetry-protected quasi-BIC. (d) Schematic showing how the asymmetry parameter (α) is defined for the case (c). This parameter is important to demonstrate the inverse quadratic relation with the Q-factor. This figure is partially reproduced from Ref. [168].

Although ideally, BICs imply an infinite Q-factor, a finite Q-factor can be observed by breaking the symmetry of the meta-atoms, resulting in quasi-BICs.

For the case of symmetry-protected BICs, the BIC modes were well-studied in the work by Koshelev, *et al*. [168]. They demonstrated symmetry-protected quasi-BIC modes for the metasurfaces with different shapes of meta-atoms, see Fig. 2.16. It can be proved that the quality factor (Q) is related to the inverse quadratic of the asymmetry parameter (α) for the symmetry-protected quasi-BIC modes [168].

Also, for the case of resonance-trapped BICs, M. Rybin, *et al*. demonstrated a very high Q-factor for a dielectric nanoparticle based on the Mie resonance and a continuous adjustment of the aspect ratio of the particle [169]. For the specific dimensions of the particle, the destructive interference between different leaky modes at the far field causes a high-Q mode.

In the next chapter, we use the concept of quasi-BIC for the AlGaAs metasurfaces composed of meta-atoms shown in Fig. 2.13 to enhance the asymmetric generation of second harmonics.

Chapter 3

Nonlinear bianisotropic metasurfaces

In this chapter, we investigate and explore the nonlinear response of bianisotropic dielectric metasurfaces. We theoretically demonstrate an extremely asymmetric second harmonics generation based on the quasi-BICs modes. The results of this effort have been published in ACS Photonics [112]. The project has been performed by Ehsan Mobini (the Ph.D. candidate) in collaboration with Dr. Rasoul Alaee under supervision of Prof. Ksenia Dolgaleva.

Given the importance of the role of dielectric metasurfaces in the field of nonlinear holography, exploring asymmetric nonlinear optical responses using bianisotropy along with quasi-BICs can become a suitable solution for achieving a tunable asymmetric second-harmonic response with a high degree of control over its strength that depends on the asymmetry parameter (α). We show that around four orders of magnitude second-harmonic power difference for the forward and backward illuminations can be obtained by altering the geometrical parameters corresponding to the quasi-bound states in the continuum (quasi-BIC). The idea we propose here for obtaining asymmetric nonlinear responses is not limited to second-harmonic generation; it can be also used for the asymmetric third-harmonic generation, higher-order harmonic generations, and other parametric nonlinear optical processes.

We provide deep insight into the physical origin of the asymmetric nonlinear behavior of the bianisotropic matasurfaces based on the multipolar decomposition, asymmetrical field enhancement, and different nonlinear polarization currents for the forward and backward illuminating light.

3.1 Multipolar reflection coefficient

In this section, we explain how the reflection coefficient can be obtained in terms of electric and magnetic multipoles decomposition. This result is useful to understand the mechanism of light-matter interaction in metasurfaces. One can obtain polarization in terms of electric and magnetic multipoles. First, the polarization $\mathbf{P}$ can be expressed as [170]

$$\mathbf{P}(\mathbf{r}) = \int \mathbf{P}(\mathbf{r}^{'})\,\delta(\mathbf{r}-\mathbf{r}^{'})\,\mathrm{d}\mathbf{r}^{'}, \tag{3.1}$$

where δ is the Dirac delta function around $\mathbf{r}_0$ (at the center of mass of the particle). The Dirac delta function can be expanded in a Taylor series as

$$\delta(\mathbf{r}-\mathbf{r}^{'}-\mathbf{\Delta r}) \simeq \delta(\mathbf{r}-\mathbf{r_0}) - (\Delta\mathbf{r}.\nabla)\,\delta(\mathbf{r}-\mathbf{r_0}) + \frac{1}{2}\,(\Delta\mathbf{r}.\nabla)^2\,\delta(\mathbf{r}-\mathbf{r_0}) - \ldots, \tag{3.2}$$

in which $\Delta\mathbf{r} = \mathbf{r}^{'} - \mathbf{r_0}$. Then for an array of dielectric scatterers, the multipole decomposition of polarization $\mathbf{P}$ up to quadrupole moments can be obtained by applying Eq. (3.2) to (3.1) as

$$\begin{aligned}\mathbf{P}(\mathbf{r}) \;\simeq\; & \sum_l \Big\{ \mathbf{p}\delta\,(\mathbf{r}-\mathbf{r}_l) + \frac{i}{\omega}\,[\nabla\times\mathbf{m}\delta\,(\mathbf{r}-\mathbf{r}_l)] - \frac{1}{6}\,\mathbf{Q}^e\,\nabla\delta\,(\mathbf{r}-\mathbf{r}_l) \\ & -\frac{i}{6\omega}\Big[\nabla\times\,\mathbf{Q}^m\,\nabla\delta\,(\mathbf{r}-\mathbf{r}_l)\Big]\Big\},\end{aligned} \tag{3.3}$$

where $\mathbf{r}_l = \Lambda(l_x\mathbf{e}_x + l_y\mathbf{e}_y)$, l_x and l_y are integer numbers, $\delta\,(\mathbf{r}-\mathbf{r}_l)$ is the Dirac delta function around the center of mass of each meta-atom, and Λ is the periodicity of the array. The effective induced current can be calculated using $\mathbf{J} = -i\omega\frac{\mathbf{P}}{\Lambda^2}$ as

$$\begin{aligned}\mathbf{J} \;\simeq\; & \frac{-i\omega}{\Lambda^2}\sum_l \Big\{ \mathbf{p}\delta\,(\mathbf{r}-\mathbf{r}_l) + \frac{i}{\omega}\,[\nabla\times\mathbf{m}\delta\,(\mathbf{r}-\mathbf{r}_l)] - \frac{1}{6}\,\mathbf{Q}^e\,\nabla\delta\,(\mathbf{r}-\mathbf{r}_l) \\ & -\frac{i}{6\omega}\Big[\nabla\times\,\mathbf{Q}^m\,\nabla\delta\,(\mathbf{r}-\mathbf{r}_l)\Big]\Big\}.\end{aligned} \tag{3.4}$$

Finally, the scattered electric field in terms of multipole moments can be calculated as [171], [172]

$$\begin{aligned}\mathbf{E}^{\mathrm{sca}}(\mathbf{r}) \simeq & \frac{ik_0}{2\varepsilon_0\Lambda^2}\Bigg([\mathbf{n}\times(\mathbf{p}\times\mathbf{n})]+\frac{1}{c_0}[\mathbf{m}\times\mathbf{n}] \\ & +\frac{ik_0}{6}\left[\mathbf{n}\times\left(\mathbf{n}\times Q^e\cdot\mathbf{n}\right)\right]+\frac{ik_0}{6c_0}\left[\mathbf{n}\times Q^m\cdot\mathbf{n}\right]\Bigg),\end{aligned} \tag{3.5}$$

where k_0 , c_0 and $\mathbf{n}$ denote the wavevector in the host medium, the light velocity in vacuum and the unit vector pointing in the direction of r, respectively. If a normal incidence plane wave $\mathbf{E} = E_0 e^{ik_0 z}\mathbf{e}_x$ (where $\mathbf{n} = \mathbf{e}_z$) illuminates the metasurface, the reflection coefficient can be calculated as [171]

$$r = \frac{E^{\mathrm{sca}}}{E_0} \simeq \frac{ik_0}{2E_0\Lambda^2\varepsilon_0}\left(p_x - \frac{1}{c_0}m_y + \frac{ik_0}{6}Q^e_{xz} - \frac{ik_0}{6c_0}Q^m_{yz}\right). \tag{3.6}$$

3.2 Nonlinear bianisotropic metasurfaces

Let us begin with an $Al_{0.18}Ga_{0.82}As$ bianisotropic metasurface composed of cylindrical meta-atoms with a coaxial cylindrical hole with height h, as shown Fig. 3.1 (a). We select the composition 18% of Al to avoid the two-photon absorption effect in the metasurface at the wavelengths of operation. The metasurface is illuminated by a linearly polarized light in $\pm z$ directions ($\mathbf{k}_{\mathrm{FW/BW}} = \pm k_0\mathbf{e}_z$, where $+$ and $-$ denote forward and backward illuminations, respectively). Such a meta-atom design with magnetoelectric coupling exhibits an asymmetric linear response for the forward and backward illuminations [148], [173]. In particular, this asymmetry for *lossless reciprocal* meta-atoms manifests itself as different phases of the reflection coefficients for the forward and backward illuminations [148], [173], [174] while the reflection amplitudes are identical for the forward and backward illuminations. The reflection coefficient is given in terms of the induced multipoles up to the quadrupole orders by [171]

$$r = \frac{ik_0}{(2\varepsilon_0 E_0\Lambda^2)}\left[p_x - \frac{m_y}{c_0} + \frac{ik_0}{6}Q^{\mathrm{e}}_{xz} - \frac{ik_0}{6}\frac{Q^{\mathrm{m}}_{yz}}{c_0}\right], \tag{3.7}$$

where k_0, ε_0 and E_0 denote the wave vector in free space, the permittivity of the vacuum and the amplitude of the incident electric field, respectively, while Λ is the periodicity in x and y directions. The parameters p_x (Q^{e}_{xz}), m_y (Q^{m}_{yz}) represent the effective electric and magnetic dipole (quadrupole) moments, respectively [159].

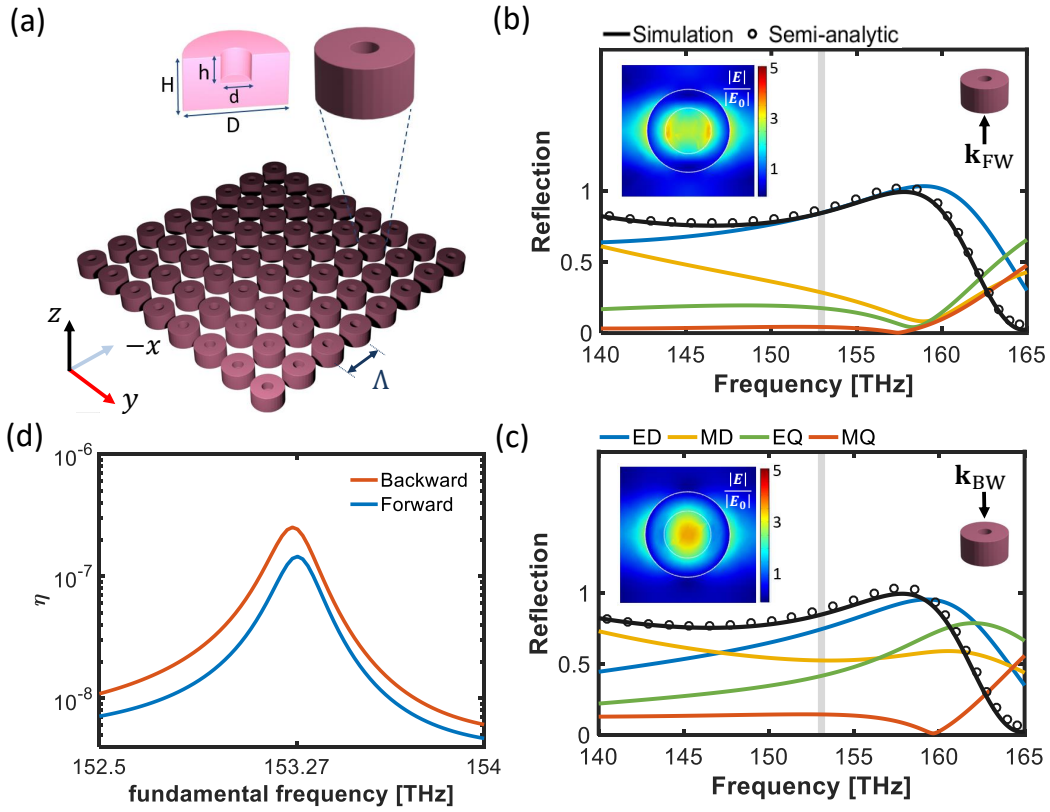

FIGURE 3.1: Linear and nonlinear responses of the bianisotropic metasurface. (a) Schematic of the bianisotropic metasurface with a coaxial cylindrical hole and its cross-sectional view with the geometrical dimensions. The metasurface is illuminated by a linearly polarized light with the wave vector $\mathbf{k}_{\mathrm{FW/BW}} = \pm k_0 \mathbf{e}_z$, where $+$ and $-$ indicate forward and backward illuminations, respectively. (b)–(c) The reflection spectrum and multipolar contributions for the forward and backward illumination directions, respectively. The semi-analytic reflection is obtained using Eq. (3.7). The insets show the normalized electric field $|\mathbf{E}| \,/\, |\mathbf{E}_0|$ in the middle of the meta-atom (xy-plane), where $|\mathbf{E}_0|$ is the amplitude of the incident field. The grey shaded bar shows the frequency at which the SH conversion efficiency is investigated. ED (MD) and EQ (MQ) indicate the contributions of the electric (magnetic) dipole and quadrupole moments, respectively. (d) The second-harmonic conversion efficiencies $\eta = P_{\mathrm{SHG}}/P_{\mathrm{pump}}$ for the forward and backward illumination directions. The geometrical parameters of the bianisotropic metasurface are $d = 420\,\mathrm{nm}$, $D = 760\,\mathrm{nm}$, $h = 360\,\mathrm{nm}$, $H = 720\,\mathrm{nm}$ and $\Lambda = 1260\,\mathrm{nm}$, where Λ is the periodicity of the metasurface in x and y directions.

Figure 3.1 (b)–(c) depicts the reflection obtained through numerical simulation and semi-analytical method for the forward and backward illumination directions, respectively. We solve a full field problem in the frequency domain with COMSOL Multiphysics using perfectly-matched layer (PML) boundary conditions, periodic boundary conditions, and two exciting ports to simulate the reflection spectrum, the ratio of nonlinear polarisation currents, and the induced multipoles. Then, to calculate the conversion efficiencies, we solve a scattering problem with the nonlinear polarisation current as the source of second harmonics at frequency 2ω. Finally, the nonlinear simulation is followed by the calculation of the second-harmonic power by integrating the Poynting vector on two virtual planes located at the top and bottom of the unit cell, surrounding the meta-atom. The semi-analytic approach is based on the multipolar decomposition of the polarization current using Eq. (3.7). The agreement between the simulation and semi-analytic method is shown in Figure 3.1 (b)–(c). Although the forward and backward reflections are identical, the multipolar contributions for the opposite illumination directions (*i.e.*, $\mathbf{k}_{\mathrm{FW/BW}}$) are quite different. In particular, in the case of backward illumination, the magnetic dipole contribution becomes comparable to the electric dipole contribution. In fact, different field distributions in the meta-atom (or different polarization currents) produce different induced multipoles [see the insets of Fig. 3.1 (b)–(c)]. Note that the metasurface is reciprocal as we have identical transmission spectra for the forward and backward illuminations and also the permittivity of the meta-atoms is time-invariant here [175].

We use COMSOL Multiphysics based on finite element methods to perform numerical simulations in two steps to obtain the second-harmonic generation. First, Maxwell's equations are solved to calculate the bianisotropic structure's field distributions and linear response. Second, the previously obtained nonlinear polarization current is used as a source of 2ω in a scattering problem to generate second harmonics.

All three components of the nonlinear polarization vector for AlGaAs crystal, with a zinc-blende structure and symmetry $\bar{4}3m$ can be obtained through Eq. (2.4). Because the periodicity of the lattice is greater than the radiated wavelength at 2ω, the second-harmonic radiation generated by the bianisotropic metasurface is governed by diffraction. The vectorial components

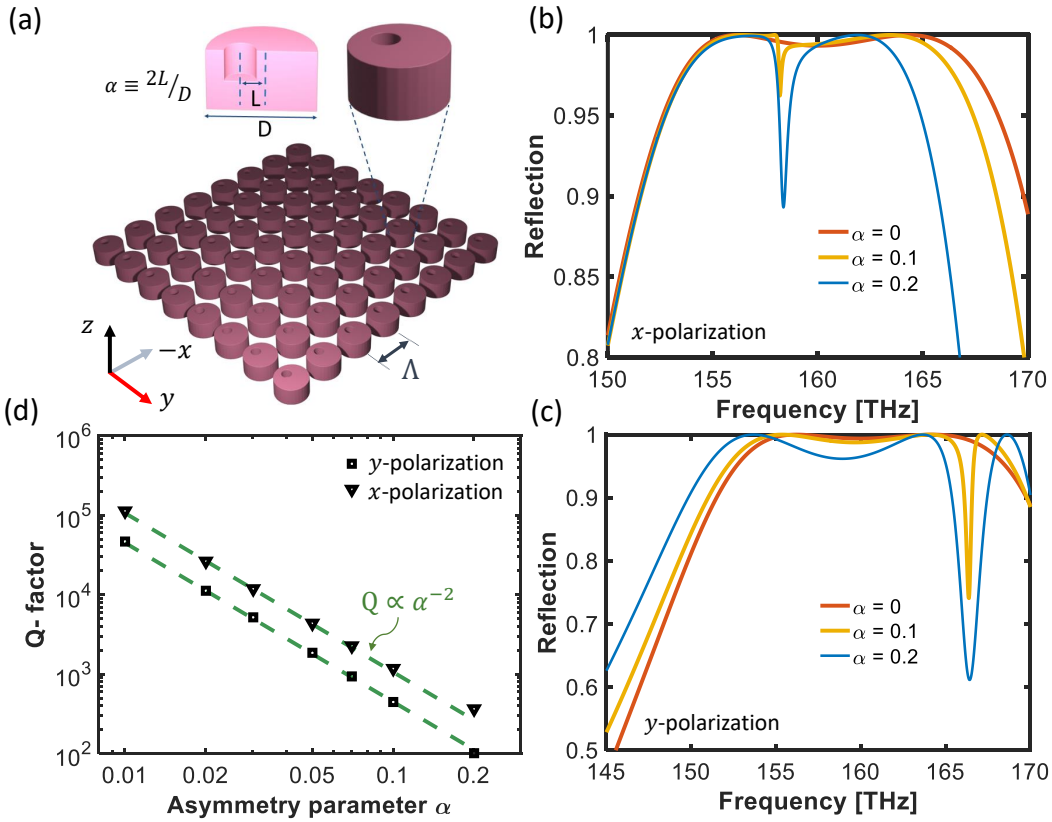

FIGURE 3.2: Linear response of the bianisotropic metasurface based on bound states in the continuum. (a) Schematic of the bianisotropic metasurface (and its cross-sectional view) with a broken symmetry characterized by the asymmetry parameter $\alpha = 2L/D$, where L is the shift distance between the axis of the cylinder and the hole. (b)–(c) The reflection spectrum with the x- and y-polarization of the illuminating light for three different values of the asymmetry parameter: $\alpha = 0, 0.1, 0.2$. (d) The Q-factor as a function of the asymmetry parameter α for the x- and y-polarization of the illuminating light obtained from the eigenmode analysis and Eq. (3.9). The inverse quadratic dependence of the Q-factor on the asymmetry parameter $Q \propto \alpha^{-2}$ shows that our proposed metasurface (schematically shown in (a)) exhibits the symmetry-protected quasi-BICs [168].

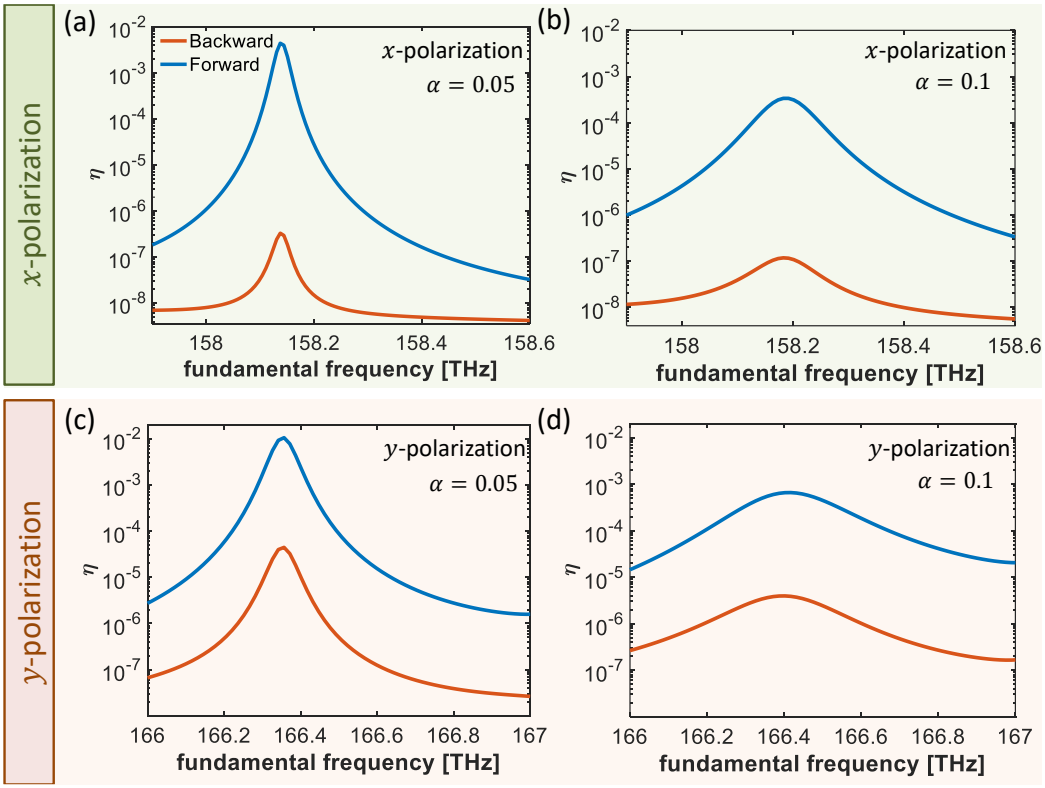

FIGURE 3.3: Second harmonic (SH) conversion efficiencies of the bianisotropic metasurface based on bound states in the continuum. (a)–(b) The calculated SH conversion efficiencies for two different values of the asymmetry parameter, i.e., $\alpha = 0.05$ and 0.1 and $x-$polarization of illuminating light. The blue and red curves denote forward and backward conversion efficiencies, respectively. (c)–(d) Same as (a)–(b) for y-polarization.

of the nonlinear polarisation current can be calculated in the frequency domain as

$$\begin{cases} J_x = -i(2\omega)\varepsilon_0\chi^{(2)}E_y(\omega)\,E_z(\omega)\,, \\ J_y = -i(2\omega)\varepsilon_0\chi^{(2)}E_z(\omega)\,E_x(\omega)\,, \\ J_z = -i(2\omega)\varepsilon_0\chi^{(2)}E_x(\omega)\,E_y(\omega)\,. \end{cases} \tag{3.8}$$

The insets of Fig. 3.1 (b)–(c) show that the generated electric fields inside the bianisotropic meta-atoms for the backward and forward illumination directions are different, resulting in different nonlinear polarization currents. As a result, we expect to achieve different conversion efficiencies of second-harmonic generation $\eta = P_{\text{SHG}}/P_{\text{pump}}$, where P_{SHG} and P_{pump} are the radiated power at 2ω and the pump power at ω, respectively. The calculated conversion efficiency for backward illumination is nearly two times greater than that for the forward illumination, as shown in Fig. 3.1 (d). It should be noted that we assumed a pump intensity of $1\,\text{MW}/\text{cm}^2$.

3.3 Nonlinear bianisotropic metasurfaces based on bound states in the continuum

In this section, we propose a robust method for enhancing and controlling the conversion efficiency of second-harmonic generation for opposite illuminations in bianisotropic metasurfaces. Optical BICs with sharp resonances are a powerful concept for fortifying asymmetric features of bianisotropic metasurfaces in the nonlinear regime. In the same vein, we apply in-plane asymmetry to the bianisotropic meta-atom to obtain quasi-BIC modes and calculate the corresponding second-harmonic conversion efficiencies.

Let us assume a bianisotropic meta-atom with geometrical dimension $d = 270\,\text{nm}$, $D = 900\,\text{nm}$, $h = 360\,\text{nm}$, $H = 720\,\text{nm}$, and $\Lambda = 1260\,\text{nm}$, see Fig. 3.2 (a). The asymmetry parameter is defined as $\alpha = 2L/D$, where L represents the shift distance between the axis of the cylinder and the hole. We have optimized the structure dimensions so that it exhibits maximum bianisotropic response as well as the BIC effect. Furthermore, the dimensions are chosen to have appropriate resonances, avoiding two-photon absorption in $Al_{0.18}Ga_{0.82}As$.

Figures 3.2 (b) and (c) show the reflection coefficients for three different values of the asymmetry parameter and two polarizations of the illuminating light. It can be seen from the figure that the resonance linewidth increases as the asymmetry parameter increases, facilitating the coupling channel of light to the free space. Furthermore, the Q-factor can be calculated using the metasurface's eigenmode analysis as

$$Q = \frac{\text{Re}\,(\omega_r)}{2\text{Im}\,(\omega_r)}, \tag{3.9}$$

where ω_r is the complex eigenvalue. Figure 3.2 (d) depicts the Q-factor versus the asymmetry parameter for both x- and y-polarization, where the inverse quadratic dependence of the Q-factor on the asymmetry parameter $Q \propto \alpha^{-2}$ identifies the prominent resonances as symmetry-protected quasi-BICs [168]. According to the multipolar decomposition, the BIC modes for the forward- and backward-illuminating light are caused by the interference of electric and magnetic dipole and quadrupole moments, see Fig. 3.4.

To investigate the asymmetric nonlinear response of our metasurface with quasi BICs, we calculated the second-harmonic conversion efficiencies for

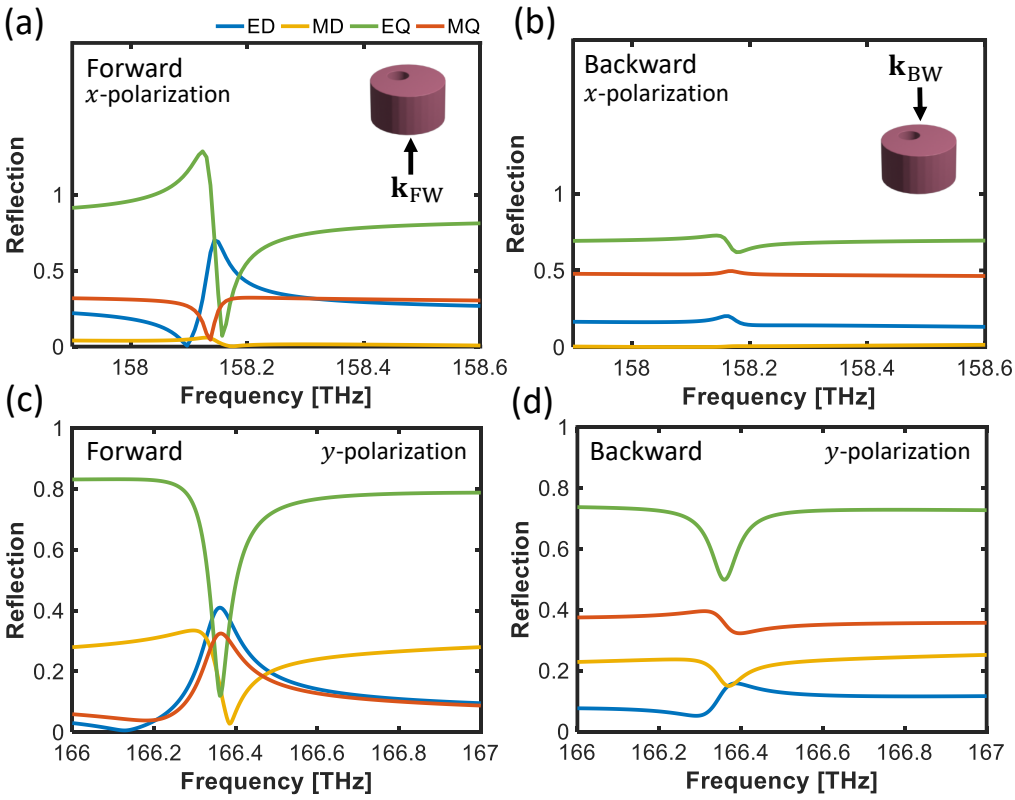

FIGURE 3.4: The multipolar decomposition of the reflection coefficient for the bianisotropic metasurface up to quadrupolar terms for the x- and y-polarization. The asymmetry parameter (α) is 0.05.

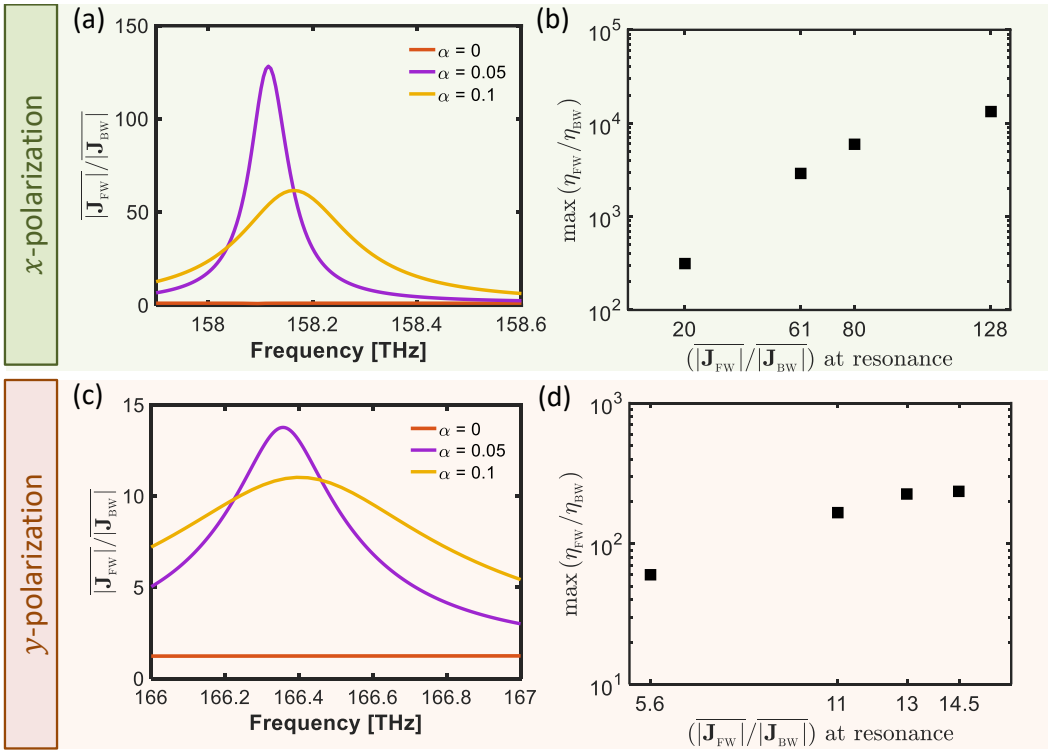

FIGURE 3.5: (a) The factor $\overline{|\mathbf{J}_{\mathrm{FW}}|}/\overline{|\mathbf{J}_{\mathrm{BW}}|}$ obtained from Eq. (3.10) as a function of frequency for $x-$polarization and three different values of the asymmetry parameter, where the bar over the current ($\mathbf{J}_{\mathrm{FW/BW}}$) indicates the average in the volume [see Eq. (3.10)]. (b) Maximum ratio of conversion efficiencies $\{\eta_{FW}/\eta_{BW}\}$ as a function of factor $\overline{|\mathbf{J}_{\mathrm{FW}}|}/\overline{|\mathbf{J}_{\mathrm{BW}}|}$. Each $\overline{|\mathbf{J}_{\mathrm{FW}}|}/\overline{|\mathbf{J}_{\mathrm{BW}}|}$ (or each black square) is associated with a specific value of α; the black squares are corresponding to $\alpha = 0.2, 0.1, 0.07, 0.05$, from left to right, respectively. (c)–(d) Same as (a)–(b) for $y-$polarization.

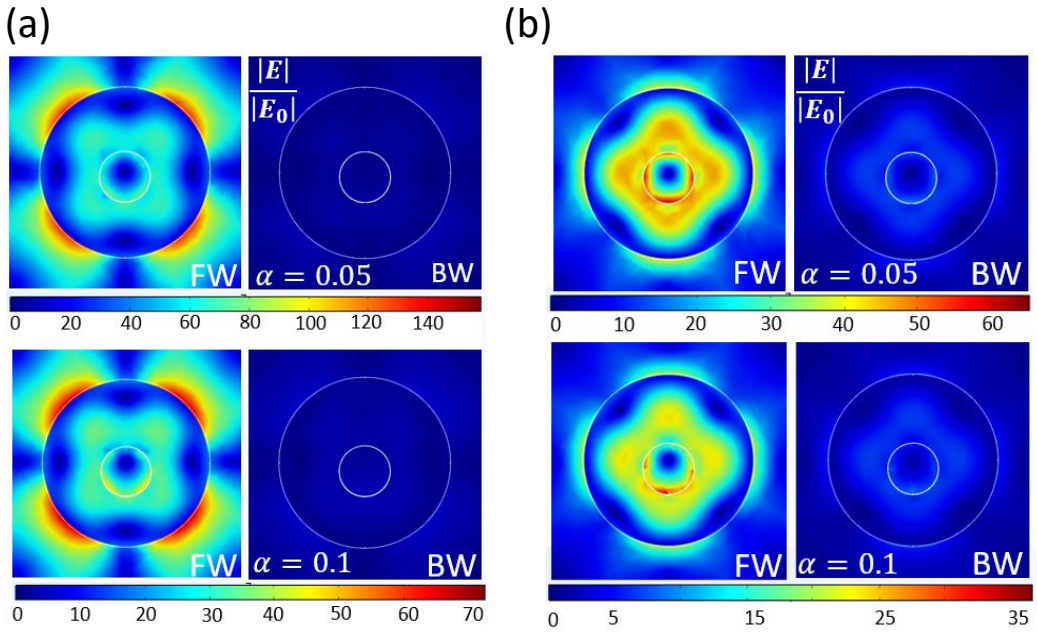

FIGURE 3.6: (a) The normalized electric field in the middle of the meta-atom in xy-plane (shown in Fig. 3.2 (a)) for two different values of the asymmetry parameter, i.e., $\alpha = 0.05$ and 0.1 for $x-$ polarization. The normalized electric field distributions in the middle of the meta-atom are illustrated for forward and backward illumination direction at the resonance frequency. (b) Same as (a) for $y-$polarization.

the opposite illumination directions and two different values of the asymmetry parameter (i.e., $\alpha = 0.05$ and 0.1) and polarizations [see Fig. 3.3]. For the opposite directions of illumination at the frequency of quasi-BIC modes, our results show a high conversion efficiency and a giant ratio of imbalanced second harmonics. The second-harmonic conversion efficiency decreases as the asymmetry parameter increases for both polarizations, which is caused by an increase in the resonance linewidth [e.g., compare Fig. 3.3 (a) and (b)]. We get a giant ratio of forward to backward second-harmonic intensities, $\eta_{FW}/\eta_{BW} \approx 10^4$ for x-polarization. For illuminating light with y-polarization, this ratio drops by at least two orders of magnitude. Interestingly, being dual quasi-BICs in terms of illuminating light polarisation adds one more degree of freedom to the proposed design of the meta-atom for manipulation and control of the ratio η_{FW}/η_{BW}.

To comprehend the underlying physical mechanism of the asymmetric second-harmonic generation in our bianisotropic metasurface, we investigate the nonlinear polarization current as the source of second harmonics for opposite illumination directions. The average nonlinear polarization current at frequency 2ω is related to the electric field components at the fundamental frequency as

$$\begin{aligned} \overline{|J_j|} &= \frac{2\omega\varepsilon_0\chi^{(2)}}{V} \\ &\times \int_V \sqrt{\left|E_{x_j}(\omega)\,E_{y_j}(\omega)\right|^2 + \left|E_{z_j}(\omega)\,E_{x_j}(\omega)\right|^2 + \left|E_{y_j}(\omega)\,E_{z_j}(\omega)\right|^2}\,\mathrm{d}V \end{aligned} \tag{3.10}$$

where $j = \{\mathrm{BW}, \mathrm{FW}\}$ and the average in the volume of the meta-atom (V) is indicated by the bar above the current. Although the right-hand side of Eq. (3.10) can be fully characterized in terms of electric field components obtained through the linear simulation, it provides an insight into the nonlinear optical response of the structure via its relationship to the nonlinear polarization current components (i.e., J_x, J_y, J_z).

Figures 3.5 (a) and (c) depict the factor $\overline{|\mathbf{J}_{\mathrm{FW}}|}/\overline{|\mathbf{J}_{\mathrm{BW}}|}$ for three different values of the asymmetry parameter and $x-$ and $y-$ polarizations, respectively. For different polarizations, the factor $\overline{|\mathbf{J}_{\mathrm{FW}}|}/\overline{|\mathbf{J}_{\mathrm{BW}}|}$ resonates at the frequency of the quasi-BIC modes. As the asymmetry parameter is increased, the resonances become weaker. Furthermore, it can be seen from the calculations above that for certain moderate values of the asymmetry parameter, i.e.,

α, it can be realized that the ratio of second-harmonic power for the forward and backward directions rises when the factor $\overline{|\mathbf{J}_{\mathrm{FW}}|}/\overline{|\mathbf{J}_{\mathrm{BW}}|}$ increases (or equivalently when the asymmetry parameter decreases) [see Fig. 3.5 (b) and Fig. 3.5 (d)]. Note that the maximum ratio of the conversion efficiencies, i.e. $\max(\eta_{FW}/\eta_{BW})$ cannot be fitted to the ratio of the nonlinear polarization currents for the forward and backward directions $(\overline{|\mathbf{J}_{\mathrm{FW}}|}/\overline{|\mathbf{J}_{\mathrm{BW}}|})^2$. This is because the conversion efficiency is also affected by the spatial and spectral characteristics of the second-harmonic mode [176].

Importantly, we find that the maximum induced nonlinear polarisation currents inside meta-atoms at quasi-BIC resonances coincide with the maximum asymmetry of second-harmonic generation. It basically means that there is a big difference in the field strength inside the meta-atoms for the forward and backward illuminations. To investigate this, the normalised field distributions in the xy-plane (in the middle of the meta-atom) are shown in Fig. 3.6 (a) and Fig. 3.6 (b), with significantly different field enhancement factors for two opposite illumination directions. For the x-polarization (y-polarization), the field enhancement of 140 (60) and 70 (35) can be obtained with $\alpha = 0.05$ and 0.1, respectively, for the forward-illuminating light. These values fall to 13 (14) and 8 (7) for the backward-illuminating light [compare Fig. 3.6 (a) and Fig. 3.6 (b)]. Fundamentally, it confirms the collaborative role of bianisotropy and the quasi-BIC modes in the highly asymmetric SHG in the proposed metasurface.

3.3.1 The effect of bianisotropy on the directional SH generation

In this subsection, we explore another effect of bianisotropy on the directional SH generation through simulations and compare the results with those for the anisotropic metasurface, see the different meta-atoms in Fig. 3.7 (a-left). Here, the directionality is defined as the ratio of the second-harmonic power (P^{SH}) at the upper and lower virtual planes, see Fig. 3.7 (a-right). It can be seen from Fig. 3.7 (b) that the largest value of directionality for the anisotropic metasurface is around 6. This value can be increased to 70 when using the bianisotropic metasurface.

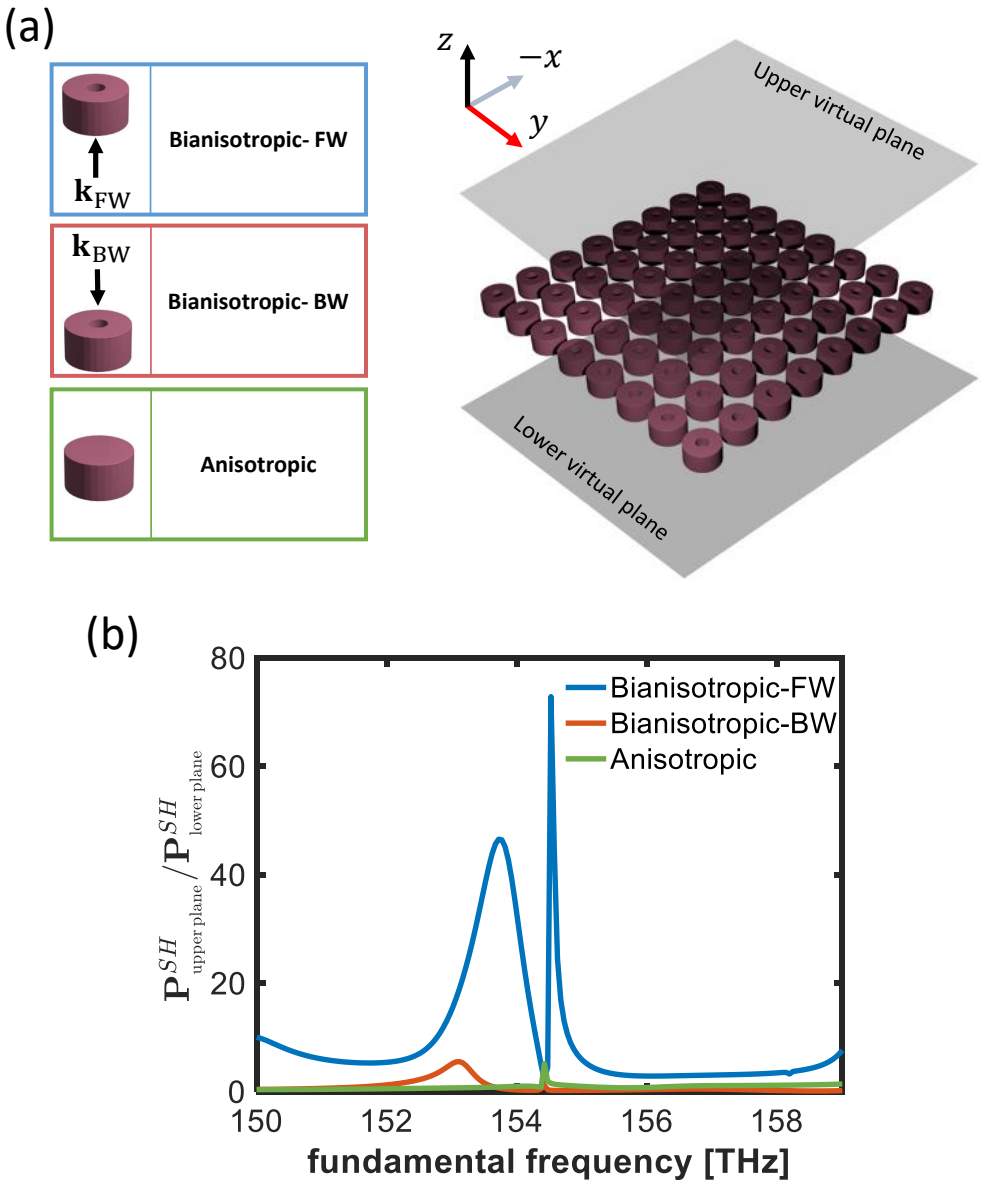

FIGURE 3.7: (a-left) The bianisotropic and anisotropic meta-atoms. (a-right) The virtual planes at which the SH power is calculated. (b) The ratio of the second-harmonic power at the upper and lower virtual planes for the bianisotropic and anisotropic metasurfaces.

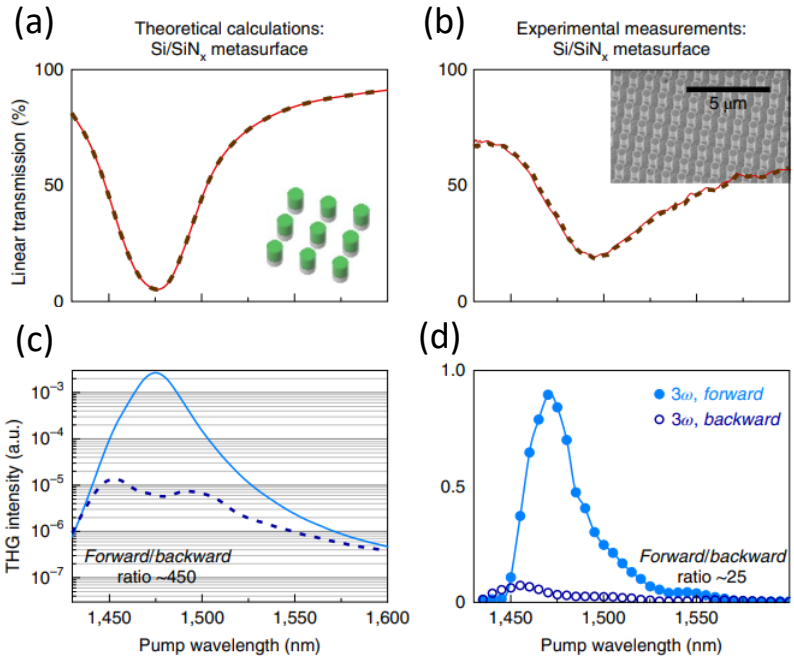

FIGURE 3.8: (a)–(b) The simulated and experimental transmission spectra, respectively, for the bilayer metasurface made of silicon and silicon nitride. The solid line and dashed line show forward and backward illuminations, respectively. (c)–(d) The simulated and experimental results for the third-harmonic generation. Reprinted by permission from Nature [177], ©2022.

3.3.2 Recent demonstration of the effect of bianisotropy on the asymmetric third-harmonic generation

Recently, Sergey S. Kruk, *et al*. demonstrated experimentally the effect of bianisotropy on the third-harmonic generation in dielectric metasurfaces using two different materials [177], see Fig. 3.8 (a). They used a bilayer metasurface made of silicon and silicon nitride. Therefore the out-of-plane symmetry is broken by the difference in the materials for the forward and backward illuminations. Experimentally, they obtained the ratio of 25 for the backward to forward THG, see Fig. 3.8 (b)–(d).

3.4 Fabrication development of the designed AlGaAs metasurface in our group

To follow the idea of asymmetric second-harmonic generation based on bianisotropic $Al_{0.18}Ga_{0.82}As$ metasurfaces, Kaustubh Vyas (another Ph.D. student in our group at uOttawa) made an initial attempt to fabricate $Al_{0.18}Ga_{0.82}As$

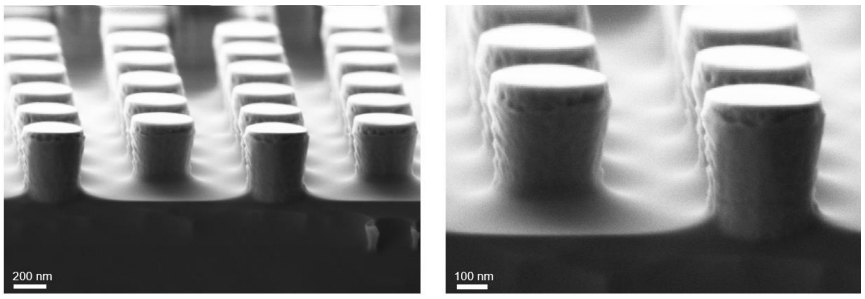

FIGURE 3.9: SEM image of $Al_{0.18}Ga_{0.82}As$ pillars fabricated by Kaustubh Vyas in our group at Ottawa [179].

pillars. An optimized wet etching using 5% HF was used to remove the top cladding leaving the higher concentration core layer untouched. The standard top-down fabrication was then used to fabricate the cylindrical pillars (this process is described later in Chapter 5, Section 5.3). The inverse of the holes was patterned using a positive-tone resist ZEP520a, which left standing pillars after the development. An optimized Cl_2- and BCl_3-based plasma etching recipe was used to etch the cylindrical pillars, as shown in Fig. 3.9. The next step is to make use of RIE lag to create holes inside the pillars using a single-step plasma etching.

Our theoretical analysis was performed for the metasurface suspended in the air. However, in reality, to mount the device, the metasurface is placed on a substrate. Therefore, the future plan for the fabrication is to embed the metasurface in a homogeneous surrounding medium *e.g.* silica. To this end, the wafer bonding technique [178] can be used to bond AlGaAs and silica. Then the process is followed by E-beam writing for patterning the array of meta-atoms and etching. Finally, silicon oxide is deposited on the top of the metasurface. Prior to that, simulation for the realistic structure should be performed because it is necessary to design a finite-size metasurface along with investigating the effect of using limited numbers of meta-atoms on the Q-factor [35].

3.5 Conclusions

We theoretically demonstrated a giant asymmetric second-harmonic generation produced by bianisotropy and quasi-BIC modes in nonlinear metasurfaces with broken in-plane symmetry. We analyzed our findings using the induced multipole moments and nonlinear polarization currents as the source

of nonlinearity. We discovered that the sharp resonances of the quasi-BIC modes can be used to boost the nonlinear polarization currents, which coincides with a very asymmetric field enhancement inside the meta-atoms due to bianisotropy. Our approach to achieving asymmetric nonlinear response is not limited to the second-harmonic generation; it can also be extended to the third- and higher-order harmonic generations, as well as other parametric nonlinear optical processes [180], [181]. Our findings have the potential to be applied to nonlinear holography.

Chapter 4

Generation and propagation of nonlinear optical waves in optical waveguides

Nonlinear optics describes how high-intensity coherent light interacts with a nonlinear medium, inducing the contributions to the medium's polarization scaling as several powers of the light's electric field strength. The first manifestation of nonlinear optical interactions was reported in 1961 by Franken *et al.* [182], where they demonstrated the generation of second harmonics from a quartz crystal illuminated by a pulsed ruby laser (694 nm). Since then, the realm of nonlinear optics has expanded to include numerous nonlinear media and phenomena, targeting the realization of highly efficient and scalable nonlinear optical devices with engineered nonlinear optical responses.

The goal of this theoretical work in this chapter is to develop means for modeling the nonlinear propagation of light in optical waveguides with the accompanying phenomena such as self-phase modulation (SPM) and four-wave mixing (FWM). For this reason, we first provide the theoretical background and derive some of the relevant equations *i.e.* nonlinear Schrodinger equations (NLSE) from the first principle, and then rely on numerical tools (MATLAB) to solve them.

4.1 Propagation of electromagnetic waves in a nonlinear medium

Let us start with Maxwell's equations in a source-free medium in the form [183]

$$\nabla \times \mathbf{E} = -\frac{\partial \mathbf{B}}{\partial t}, \tag{4.1}$$

$$\nabla \times \mathbf{H} = \frac{\partial \mathbf{D}}{\partial t}, \tag{4.2}$$

$$\nabla \cdot \mathbf{D} = 0, \tag{4.3}$$

$$\nabla \cdot \mathbf{B} = 0, \tag{4.4}$$

where **E**, **H**, **D** and **B** denote electric field vector, magnetic field vector, electric flux density, and magnetic flux density, respectively. The vectors **D** and **B** are defined as

$$\mathbf{D} = \varepsilon_0 \mathbf{E} + \mathbf{P}, \tag{4.5}$$

$$\mathbf{B} = \mu_0 \mathbf{H}, \tag{4.6}$$

where **P** and ε_o represent induced electric polarization and vacuum permittivity, respectively. The wave equation can be obtained as

$$\nabla \times \nabla \times \mathbf{E} = -\mu_0 \varepsilon_0 \frac{\partial^2 \mathbf{E}}{\partial t^2} - \mu_0 \frac{\partial^2 \mathbf{P}}{\partial t^2}, \tag{4.7}$$

where μ_0 represents vacuum permeability. Assuming

$$\mathbf{P}(\mathbf{r}, t) = \mathbf{P_L}(\mathbf{r}, t) + \mathbf{P_{NL}}(\mathbf{r}, t), \tag{4.8}$$

(where $\mathbf{P_L}$ and $\mathbf{P_{NL}}$ are the linear and nonlinear contributions to the polarization vector), the wave equation can be written as

$$\nabla^2 \mathbf{E} - \mu_0 \varepsilon_0 \frac{\partial^2 \mathbf{E}}{\partial t^2} - \mu_0 \frac{\partial^2 \mathbf{P_L}}{\partial t^2} = \mu_0 \frac{\partial^2 \mathbf{P}_{\mathrm{NL}}}{\partial t^2}. \tag{4.9}$$

4.2 Dispersion

A key parameter in the propagation of electromagnetic waves is dispersion. Here, we merely consider two kinds of dispersion *i.e*. material dispersion and waveguide dispersion. The material dispersion (chromatic dispersion) is the change of the refractive index as a result of the change in wavelength. On the other hand, the waveguide dispersion is related to the change in the $effective$ index of the waveguide (n_{eff}) when the wavelength changes ($n_{\text{eff}} = \beta/k_0$ and β and k_0 represent the propagation constant of the waveguide and the wave number in free space, respectively). This dispersion depends on the waveguide cross-section geometry and the core and cladding refractive index contrast, and its impact becomes significant for the waveguides with narrower widths. Due to dispersion, different spectral components experience different speeds of propagation leading to group-velocity dispersion (GVD). This characteristic restricts the nonlinear interaction length in the waveguide due to the temporal walk-off between the interacting wavelengths (as the spectral difference between the interacting wavelengths increases, the temporal overlap between the pulses decreases).

Mathematically, GVD is defined as the second derivative of the propagation constant β with respect to the angular frequency. In this thesis, the parameter GVD is calculated through the dispersion parameter (D) as

$$GVD = -\frac{\lambda^2}{2\pi c} D, \tag{4.10}$$

where the parameter D is defined as

$$D = \frac{\partial \tau_g}{\partial \lambda} \tag{4.11}$$

in which $\tau_g = \partial\beta/\partial\omega$ is the group delay. The parameter D is extracted from a numerical solver *e.g*. Lumerical.

4.3 Propagation of electromagnetic waves inside a χ^3 nonlinear waveguide

In order to understand the $\chi^{(3)}$ effects in a waveguide, it is necessary to employ the mathematical equation of propagating waves, namely, the nonlinear Schrodinger equation (NLSE). Let us start with the Helmholtz equation in the

form

$$\nabla \times \nabla \times \mathbf{E} + \frac{1}{c_0^2}\frac{\partial^2 \mathbf{E}}{\partial t^2} + \mu_0 \frac{\partial^2 \mathbf{P}_L}{\partial t^2} = -\mu_0 \frac{\partial^2 \mathbf{P}_{NL}}{\partial t^2}, \tag{4.12}$$

where c_0 and $\mathbf{P}_{NL}$ are the nonlinear part of the polarization and the speed of light in vacuum, respectively. Using the slowly varying envelope approximation (SVEA) and taking the Fourier transform of the above equation, it can be written as [183]

$$\nabla^2 \tilde{E} + \varepsilon(\omega)\frac{\omega^2}{c^2}\tilde{E} = 0, \tag{4.13}$$

where $\varepsilon = \varepsilon_L + \varepsilon_{NL}$.

Next, we employ the method of separation of variables as

$$\tilde{E}(r, \omega - \omega_0) = F(x, y)\,\tilde{A}(z, \omega - \omega_0)\, e^{i\beta_0 z}, \tag{4.14}$$

where $\tilde{A}$ is a slowly varying function and β_0 is the propagation constant in the medium. The above equation gives rise to two equations for the variables F and $\tilde{A}$:

$$\frac{\partial^2 F}{\partial x^2} + \frac{\partial^2 F}{\partial y^2} + \left[\varepsilon(\omega)\frac{\omega^2}{c^2} - \tilde{\beta}(\omega)\right] F = 0, \tag{4.15}$$

$$2i\beta_0 \frac{\partial \tilde{A}}{\partial z} + \left(\beta^2 - \beta_0^2\right)\tilde{A} = 0, \tag{4.16}$$

where $\varepsilon(\omega) = (n + \triangle n)^2$. The change in the refractive index $(\triangle n)$ is attributed to the nonlinearity and loss in the waveguide, which can be expressed as

$$\triangle n \simeq n_2 |E|^2 + i\frac{\alpha}{2k_0}. \tag{4.17}$$

Now, assuming $\triangle n$ as a small perturbation and using the first-order perturbation, its effect on the propagation constant (β) can be calculated as

$$\triangle \beta = \frac{\frac{\omega}{c}\int_{-\infty}^{+\infty} \triangle n\, |F(x, y)|^2 \,\mathrm{d}x\mathrm{d}y}{\int_{-\infty}^{+\infty} |F(x, y)|^2 \,\mathrm{d}x\mathrm{d}y}. \tag{4.18}$$

In fact, the parameter $\triangle \beta$ is the response to the perturbation of P_{NL} in the Helmholz equation.

Substituting Eq. (4.18) into (4.17) gives rise to

$$\triangle\beta = i\frac{\alpha}{2} + \frac{\omega n_2}{c}\left|\tilde{A}\right|^2 \frac{\int_{-\infty}^{+\infty}|F(x,y)|^4\,\mathrm{d}x\mathrm{d}y}{\int_{-\infty}^{+\infty}|F(x,y)|^2\,\mathrm{d}x\mathrm{d}y}. \tag{4.19}$$

The term $\left(\beta^2 - \beta_0^2\right)$ can be approximated as $2\beta_0\left(\beta - \beta_0\right)$, where β can be written in the form of a Taylor series expansion as

$$\beta(\omega) = \beta_0 + (\omega - \omega_0)\beta_1 + \frac{1}{2}(\omega - \omega_0)^2\beta_2 + \frac{1}{6}(\omega - \omega_0)^3\beta_3 + \ldots. \tag{4.20}$$

Here β_1, β_2 and β_3 are dispersion parameters that can be obtained as

$$\beta_1 = \frac{\mathrm{d}\beta}{\mathrm{d}\omega} = \frac{1}{v_g}, \tag{4.21}$$

$$\beta_2 = \frac{\mathrm{d}^2\beta}{\mathrm{d}\omega^2} = \frac{\mathrm{d}}{\mathrm{d}\omega}\left(\frac{1}{v_g}\right) \equiv GVD, \tag{4.22}$$

and

$$\beta_3 = \frac{\mathrm{d}^3\beta}{\mathrm{d}\omega^3} \equiv TOD, \tag{4.23}$$

in which v_g represents the group velocity i.e. the velocity at which the pulse envelope propagates. The parameters β_2 and β_3 are the group-velocity dispersion (GVD) and the third-order dispersion (TOD), respectively. Substituting the first three terms of Eq. (4.20) into Eq. (4.16), and taking the inverse Fourier transform, we get

$$\frac{\partial A}{\partial z} + \beta_1\frac{\partial A}{\partial t} + \frac{i}{2}\beta_2\frac{\partial^2 A}{\partial t^2} + \frac{\alpha}{2}A = i\gamma|A|^2 A, \tag{4.24}$$

where

$$\gamma = \frac{n_2\omega_0}{cA_{\text{eff}}} \tag{4.25}$$

is the nonlinear coefficient. A_{eff} denotes the effective mode area and is defined as

$$A_{\text{eff}} = \frac{\left[\int_{-\infty}^{+\infty}|F(x,y)|^2\,\mathrm{d}x\mathrm{d}y\right]^2}{\int_{-\infty}^{+\infty}|F(x,y)|^4\,\mathrm{d}x\mathrm{d}y}. \tag{4.26}$$

This effective mode area can be calculated using the transversal distribution of the electric field in a waveguide by a numerical solver e.g. COMSOL and Lumerical. Equation (4.24) can be simplified further if one uses a retarded frame of solving as $T = t - z/v_g$:

$$\frac{\partial A}{\partial z} + \frac{i}{2}\beta_2 \frac{\partial^2 A}{\partial T^2} + \frac{\alpha}{2}A = i\gamma |A|^2 A. \tag{4.27}$$

The above equation is called the nonlinear Schrodinger equation (NLSE) that describes many $\chi^{(3)}$ effects such as self-phase modulation (SPM) and four-wave mixing (FWM).

4.4 Kerr effect

A light with a strong intensity can change the refractive index of a material. This nonlinear optical phenomenon is called the optical Kerr effect. The real part of the intensity-dependent refractive index n can be calculated as

$$n = n_0 + n_2 I, \tag{4.28}$$

in which n_0, n_2 denote the linear refractive index and the nonlinear refractive index, respectively. The parameter $I = 2n_0\varepsilon_0 c |\mathbf{E}|^2$ represents the light intensity. The nonlinear refractive index can be calculated as

$$n_2 = \frac{3\mathrm{Re}\left(\chi^{(3)}\right)}{4n_0^2\varepsilon_0 c}. \tag{4.29}$$

4.5 Self-phase modulation

Self-phase modulation (SPM) describes the spectrum variation of a propagating pulse in a Kerr medium as a result of its own intensity. In the temporal frame, it manifests itself just as a phase shift which is dependent on the intensity of the pulse. This phenomenon is essential for optical switching and super-continuum generation (SCG) [67], [184], [185].

To see the pure effect of SPM on a propagating pulse in a waveguide, let us ignore the effect of GVD and the linear loss in the NLSE. In this case, Eq. (4.27) can be written as

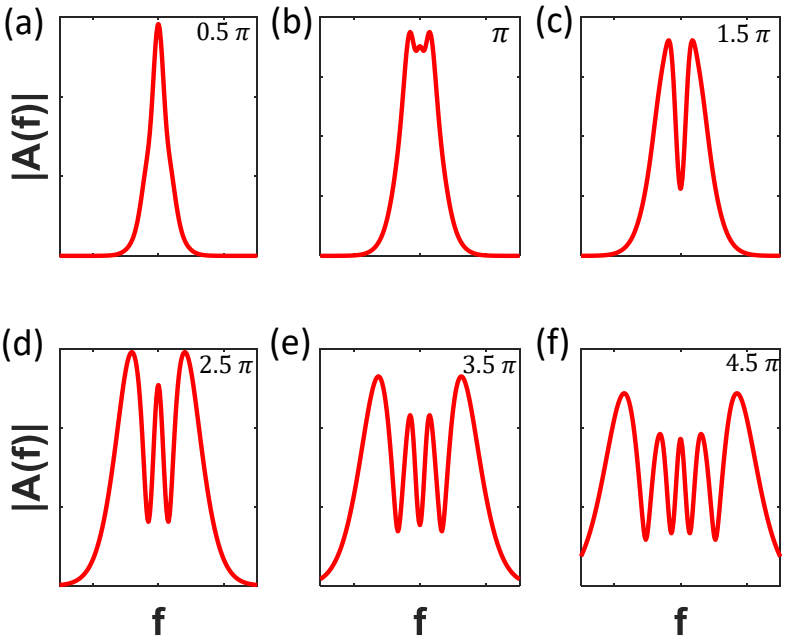

FIGURE 4.1: (a)–(f). The spectrum modification through the SPM phenomena for different values of the nonlinear phase shift: 0.5π, π, 1.5π, 2.5π, 3.5π and 4.5π. The parameter f represents optical frequency.

$$\frac{\partial A}{\partial z} = i\gamma |A|^2 A. \tag{4.30}$$

The solution to the above equation can be written in the form

$$A(z,t) = A(0,t)e^{i\gamma |A(0,t)|^2 z}. \tag{4.31}$$

As can be seen from Eq. (4.31), the temporal shape of the pulse during the propagation remains intact and only some nonlinear phase shift is gained. The power of the exponential term is called the nonlinear phase shift (φ_{NL}). Figure 4.1 shows the pulse spectrum for different values of the nonlinear phase shift.

Note that the effect of the linear loss can be readily added to the NLSE's solution by assuming the solution in the form

$$A(z,t) = A(0,t)e^{\left(\frac{-\alpha}{2}z\right)}e^{i\gamma |A(0,t)|^2 z}.$$

In general, the nonlinear phase shift for a varying intensity in a waveguide can be calculated as

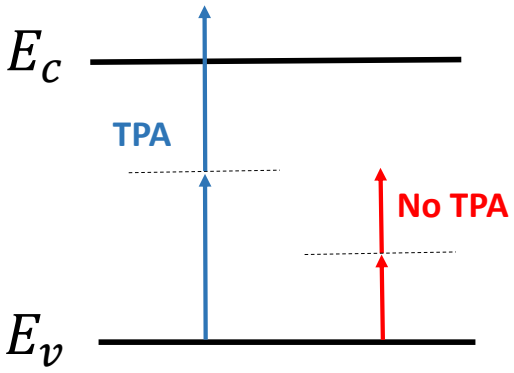

FIGURE 4.2: Schematic of the two-photon absorption effect. E_c and E_v represent the energy level of the conduction and the valence band, respectively. The dashed lines show the virtual energy levels.

$$\varphi_{\mathrm{NL}} = k_0 n_2 \int_0^L I(z)\, dz,$$

where $I(z)$ is the light intensity.

4.6 Two-photon absorption

Two-photon absorption (TPA) is a nonlinear absorption that occurs when the energy of incident photons is smaller than the bandgap but higher than or comparable to half-the-bandgap. As a result, some electrons in the valence band can transit to the conduction band (as free carriers) by a simultaneous two-photon excitation, see Fig. 4.2. Furthermore, other effects such as free-carrier absorption (FCA) and free-carrier dispersion (FCD) can occur consequently. The TPA is an intensity-dependent loss and can be calculated as

$$\alpha_{\mathrm{TPA}} = \beta_{\mathrm{TPA}} I, \tag{4.32}$$

where β_{TPA} represent the two-photon absorption coefficient. Therefore, the intensity of light propagating inside the waveguide can be calculated as the solution of the following equation:

$$\frac{\mathrm{d}I}{\mathrm{d}z} = (\alpha_0 + \alpha_{\mathrm{TPA}})\, I = \alpha_0 I + \beta_{\mathrm{TPA}} I^2. \tag{4.33}$$

For $\mathrm{In_xGa_{1-x}As_{1-y}P_y}$ (on the InP substrate), the energy for the fundamental absorption edge (Eg) at the temperature 300 K can be calculated as [106]

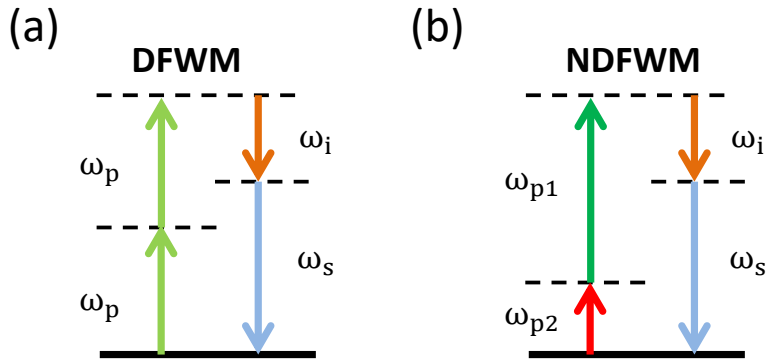

FIGURE 4.3: The energy diagrams representing (a) degenerate FWM (DFWM) and (b) non-degenerate FWM (NDFWM). The dashed lines show virtual energy states.

$$E_g(\text{eV}) = 0.75 + 0.46y + 0.14y^2. \tag{4.34}$$

Based on the above equation, for instance for $y = 0.7$, InGaAsP has the band-gap energy of $E_g = 1.1406$ (eV). As a result, the TPA effect is expected at the wavelength 1550 nm ($\sim$0.7999 eV).

4.7 Four-wave mixing (FWM)

Another nonlinear effect based on $\chi^{(3)}$ is four-wave mixing (FWM) in which an additional spectral component can be generated, see Figure 4.3. In the quantum picture, the frequency ω_i of the idler is related to the pump (ω_p) and signal frequencies (ω_s) according to $\omega_i = 2\omega_p - \omega_s$ (*i.e.* the case of degenerate four-wave mixing (DFWM), see Figure 4.3 (a)) and $\omega_i = \omega_{p_1} + \omega_{p_2} - \omega_s$ (*i.e.* the case of non-degenerate four-wave mixing (NDFWM), see Figure 4.3 (b)). The two initial waves (in the case of degenerate FWM) are called pump and signal, and the new frequency component is known as an idler. This phenomenon is essential for all-optical wavelength conversion and frequency combs.

The mathematical description of FWM in a waveguide can be performed using NLSE in the following form (tailored to a degenerate FWM): [183], [186]

$$\begin{aligned} \frac{\partial A_p}{\partial z} + \frac{i\beta_2^p}{2}\frac{\partial^2 A_p}{\partial t^2} &= \frac{-1}{2}\alpha_p A_p + i\left(\gamma_p + i\frac{\beta_{\text{TPA}}}{2A_{\text{eff}}}\right) \\ &\times \left(|A_p|^2 + |2A_s|^2 + 2|A_i|^2\right) A_p + 2i\gamma_p A_s A_i A_p^* e^{i\triangle\beta z}, \end{aligned} \tag{4.35}$$

$$\frac{\partial A_s}{\partial z} + d_s \frac{\partial A_s}{\partial t} + \frac{i\beta_2^s}{2}\frac{\partial^2 A_s}{\partial t^2} = \frac{-1}{2}\alpha_s A_s + i\left(\gamma_s + i\frac{\beta_{\text{TPA}}}{2A_{\text{eff}}}\right) \times \left(|A_s|^2 + |2A_p|^2 + 2|A_i|^2\right) A_s + i\gamma_s A_p^2 A_i^* e^{i\triangle\beta z}, \tag{4.36}$$

$$\frac{\partial A_i}{\partial z} + d_i \frac{\partial A_i}{\partial t} + \frac{i\beta_2^i}{2}\frac{\partial^2 A_i}{\partial t^2} = \frac{-1}{2}\alpha_i A_i + i\left(\gamma_i + i\frac{\beta_{\text{TPA}}}{2A_{\text{eff}}}\right) \times \left(|A_i|^2 + |2A_p|^2 + 2|A_s|^2\right) A_i + i\gamma_i A_p^2 A_s^* e^{i\triangle\beta z}, \tag{4.37}$$

where β_{TPA} is the TPA coefficient. The three equations describe the nonlinear propagation of the pump, signal, and idler waves, respectively. The parameters $d_{i,s}$ show the walk-off parameter defined as $d_{i,s}$=$\beta_{1,i,s} - \beta_{1p}$. It can be understood from the above equations that the conversion efficiency of the FWM process is dependent on the pump intensity, the nonlinearity of the waveguide, phase mismatch, overall losses in the waveguide, and the interaction length of the waveguide.

The dependency of the output power of the generated idler on the pump and signal powers can be described as [187]–[189]

$$P_i^{\text{out}} = P_s\left(\gamma P_p L_{\text{eff}}\right)^2 e^{-\alpha L}\phi, \tag{4.38}$$

$$\phi = \frac{\alpha^2}{\alpha^2 + \triangle\beta^2}\left[1 + \frac{4e^{-\alpha L}\sin^2\left(\frac{\triangle\beta L}{2}\right)}{\left(1 - e^{-\alpha L}\right)^2}\right], \tag{4.39}$$

where P_i^{out}, $P_s\,(P_p)$, and ϕ represent the idler power at the output of the waveguide, the signal (pump) power at the input of the waveguide, and the phase matching parameter, respectively. The parameter $\triangle\beta$ denotes the phase mismatch between the idler, signal, and pump. This parameter is calculated as $\triangle\beta = \triangle\beta_{\text{lin}} + 2\gamma P_p$, in which the first and the second term represent the linear and nonlinear phase mismatch, respectively. The linear part can be obtained as $\triangle\beta_{\text{lin}} = 2\beta_p - \beta_s - \beta_i$.

4.8 Numerical solutions for the four-wave mixing equations

Since the nonlinear Schrodinger equation (NLSE) is a nonlinear partial differential equation that is not simply solvable analytically, a numerical method is essentially needed to find its solution. One of the most commonly used computational methods to analyze the pulse propagation in nonlinear dispersive media is the split-step Fourier transform. The assumption here is that over a short segment (from z to $z+h$) of our waveguide the dispersion and nonlinear effects behave independently. Therefore, we divide the nonlinear Schrodinger equations into the dispersion part and the nonlinear part. Besides, each segment of length h is divided again into two equal lengths. The linear operator acts over each subsegment in the frequency domain, while the nonlinear operator acts just locally at the central point of our calculation. The nonlinear and linear terms (dispersion) are solved using Runge-Kutta forth-order method and Fourier transform, respectively.

Based on the above method, we solved Eqs. (4.36), (4.37), and (4.38) using MATLAB for some representative parameters of the waveguide *i.e.* $A_{\text{eff}} = 0.5\ \mu\text{m}^2$, $n_2 = 1.9 \times 10^{-17}\text{m}^2/\text{W}$, $\beta_2 = 10^{-24}\ s^2/\text{m}$ (we assumed almost the same GVD for the signal, idler and pump), $\beta_{\text{TPA}} = 1$ cm/GW (case one) and $\beta_{\text{TPA}} = 10$ cm/GW (case two). We assume the pump and the signal pulses as *sech* pulses

$$A_{\text{signal}} = \sqrt{P_s}\,\text{sech}\left(\frac{t}{T_0}\right) \tag{4.40}$$

$$A_{\text{pump}} = \sqrt{P_p}\,\text{sech}\left(\frac{t}{T_0}\right) \tag{4.41}$$

in which the initial width (T_0) is 20 ps and the powers P_s and P_p are 0.1 and 1 W, respectively. Figures 4.4 and 4.5 show the evolution of the signal, idler, and the pump pulse for two different values of two-photon absorption coefficient *i.e.* $\beta_{\text{TPA}} = 1$ cm/GW (case one) and $\beta_{\text{TPA}} = 10$ cm/GW (case two), respectively. The linear loss was assumed as 5 dB/cm for both cases. The parameters here were chosen to be similar to those of an InGaAsP waveguide [190]. As can be seen from Fig. 4.5, the idler amplitude drops substantially due to an increase in the TPA coefficient compared to Fig. 4.4.

The method that we have developed can be used to investigate the effect of each parameter *e.g.* A_{eff}, GVD, β_{TPA}, and other parameters in the coupled

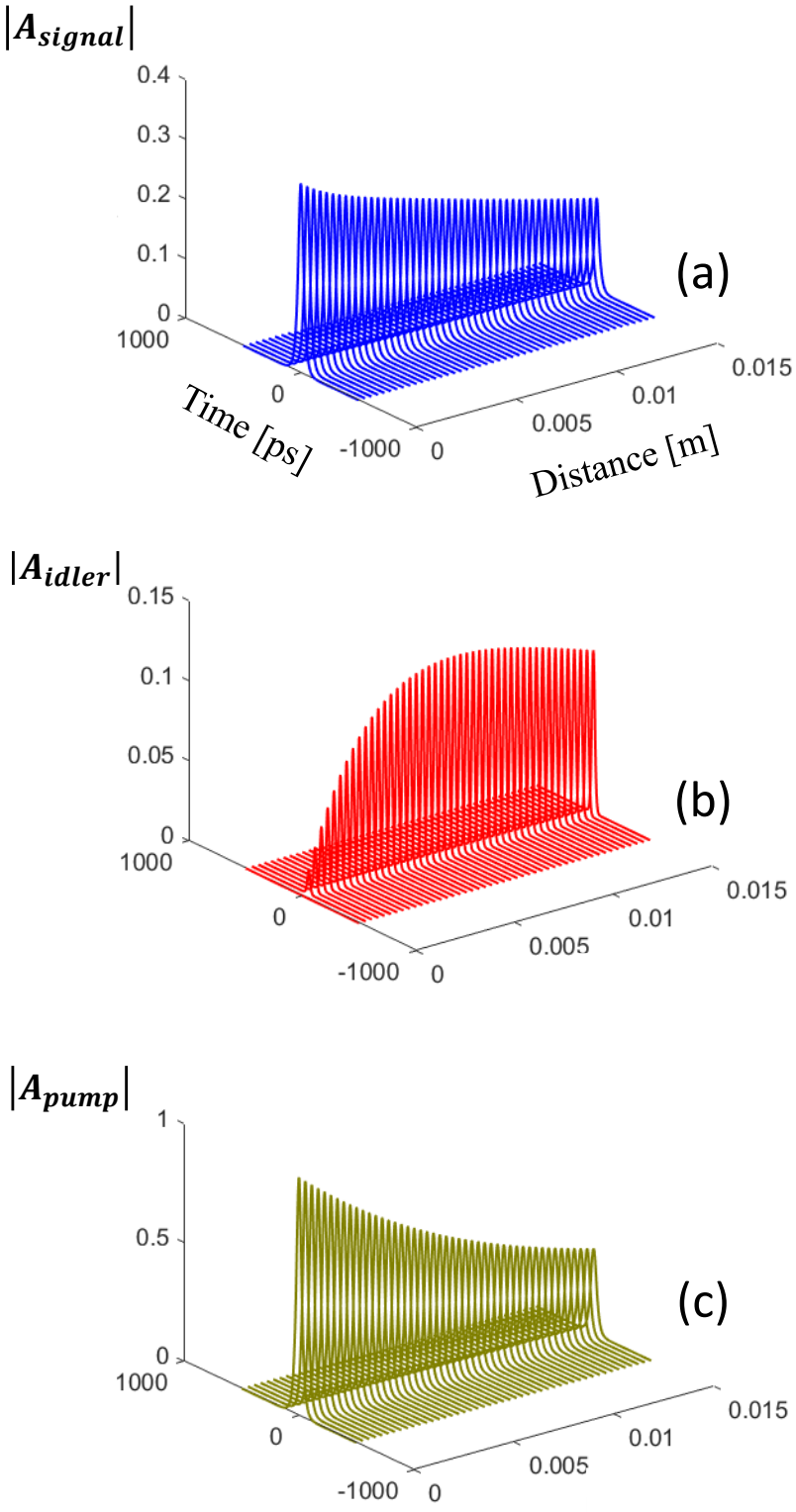

FIGURE 4.4: Simulation of FWM and nonlinear wave propagation in an optical waveguide. (a)–(c) Evolution of a sech pulse signal, idler, and a sech pulse pump, respectively, in a waveguide with $n_2 = 1.9 \times 10^{-17}\text{m}^2/\text{W}$, $\beta_{\text{TPA}} = 1$ cm/GW, $A_{\text{eff}} = 0.5\ \mu\text{m}^2$, $\beta_2 = 10^{-24}\ s^2/\text{m}$ and $\alpha = 5$ dB/cm.

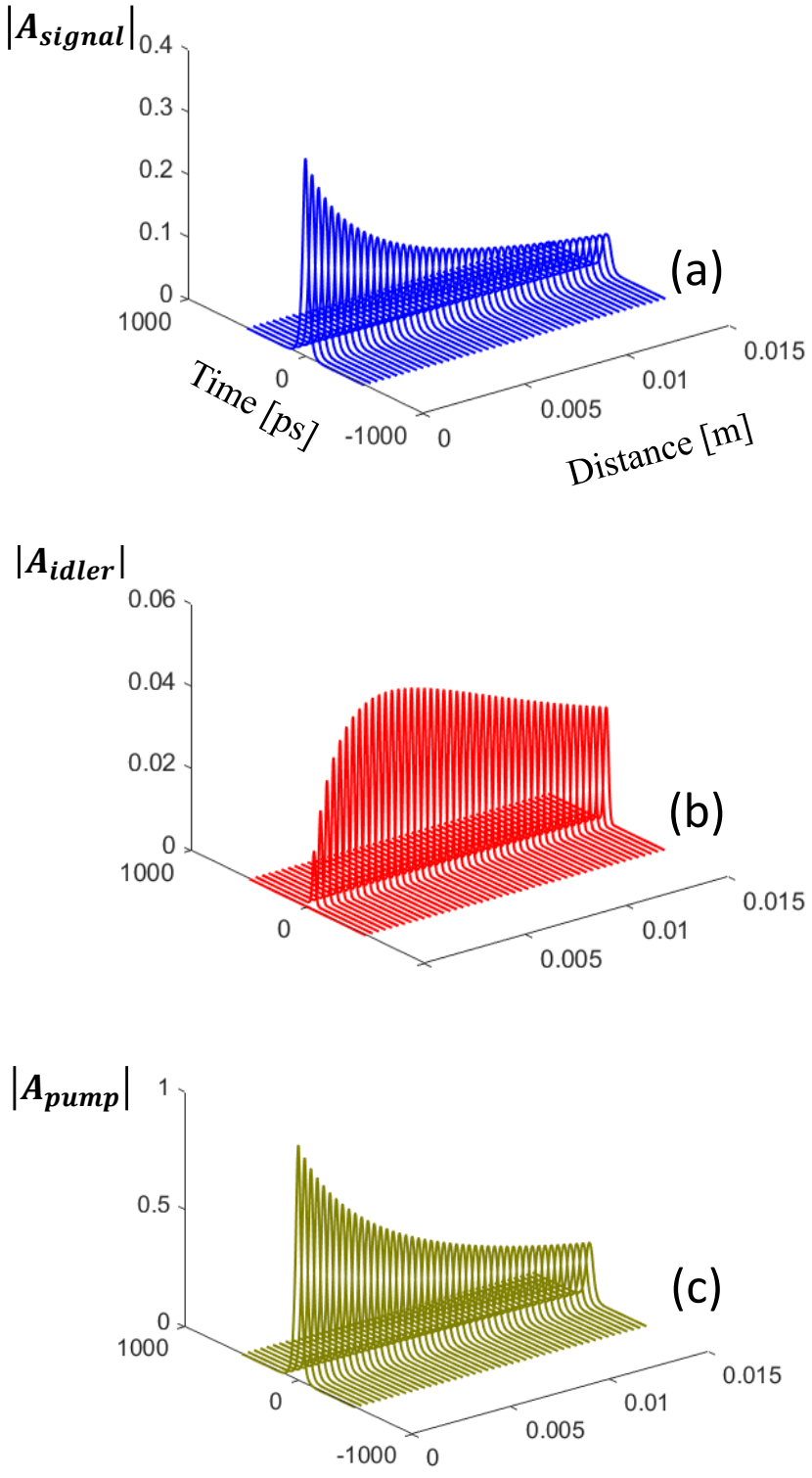

FIGURE 4.5: Simulation of FWM and nonlinear wave propagation in an optical waveguide. (a)–(c) Evolution of a sech pulse signal, idler, and a sech pulse pump, respectively, in a waveguide with $n_2 = 1.9 \times 10^{-17}$ m^2/W, $\beta_{\text{TPA}} = 10$ cm/GW, $A_{\text{eff}} = 0.5\ \mu\text{m}^2$, $\beta_2 = 10^{-24}\ s^2$/m and $\alpha = 5$ dB/cm.

equations on the FWM process in a nonlinear waveguide. Furthermore, it is also helpful to find the optimum length of a nonlinear waveguide to have maximum conversion efficiency.

Chapter 5

Nonlinear optical characterization of $In_{1-x}Ga_xAs_{1-y}P_y$ waveguides

Material selection

Indium Phosphide (InP) is an important alloy in active integrated photonics. InP/InGaAsP active devices such as lasers and optical detectors are commonly used in integrated photonics, for instance, InP/InGaAsP laser [103], [191], [192] and integrated InGaAsP/InP single-photon detectors [193], [194]. Therefore, it has been very encouraging to integrate passive nonlinear devices capable of extending the operation range of the existing InGaAsP laser sources and all-optical signal processing in InP-based transceivers to augment the functionalities of these existing InGaAsP devices.

In this chapter, we explore how InGaAsP/InP can be exploited to realize nonlinear passive waveguides on a chip. The optimal wavelength range of operation for InGaAsP passive nonlinear optical devices is at 2 μm or longer wavelengths which is dictated by the bandgap energy range [106]. The photon energy at these wavelengths falls below half-the-bandgap, and the influence of two-photon absorption is expected to be negligible. However, the experiments reported in this chapter were carried out in the wavelength range of 1480 nm to 1560 nm. This wavelength range was selected due to the availability of the laboratory equipment for the nonlinear optical characterization. Further, it is instructive to quantify optical nonlinearity of InP-based platforms in this wavelength range because this is the wavelength range of operation of optical communication networks where InP-based large-scale photonic integration is implemented [195]–[197]. In particular, incorporating passive InP nonlinear waveguides for all-optical signal processing and

wavelength conversion could be potentially a paradigm shift to the functionality of the existing transmitters and receivers by extending the operation wavelength of integrated optical lasers to longer wavelengths.

In this regard, $In_{1-x}Ga_xAs_{1-y}P_y$ with different compositions of phosphorous can provide good confinement of light with a small refractive index contrast with InP (from 0.1 for $y = 0.7$ to 0.4 for $y = 0.2$) at the wavelenght 1550 nm. InGaAsP can be grown on the native substrate of InP if the lattice-matching condition of $x = 0.47 - 0.47y$ is met [106]. Figure 5.1 shows the refractive index dispersion of InGaAsP for different compositions of phosphorous (P). It can be seen from this figure that the refractive index decreases when the concentration of P increases.

On the other hand, InGaAsP exhibits a large nonlinear refractive index (on the order of 10^{-13} cm^2/W) [190] which is comparable with that of AlGaAs (1.5×10^{-13} cm^2/W) [79]. However, there have been very few demonstrations of integrated nonlinear optical devices based on InGaAsP [190]. Further, there is lack of precise measurement of n_2 in InGaAsP waveguides. All these arguments serve as sufficient motivation for us to explore the nonlinear capabilities of InGaAsP for integration with InP active devices *e.g.* lasers and amplifiers on the same chip. To this end, in this chapter, we explore two different waveguide geometries based on a three-layer InGaAsP/InP heterostructure platform *i.e.* the half-core waveguide and nanowire. All devices we characterize here were fabricated by Kaustubh Vyas, another Ph.D. student in our group at uOttawa. The measurements were carried out jointly by Ehsan Mobini in collaboration with Dr. Daniel Espinosa, a postdoctoral researcher in our group at uOttawa. In the following section, we describe the waveguide geometries that we have been working with and compare them to the InGaAsP strip-loaded waveguides studied earlier in our group [190].

5.1 Different geometries of InGaAsP waveguides

Here, we describe three geometries of InGaAsP waveguides namely strip-loaded, half-core, and nanowire (see Fig. 5.2). However, for the rest of this thesis, we continue merely with the nonlinearity in the half-core and nanowire waveguides. The nonlinearity of strip-loaded waveguides has already been demonstrated by S. Saeidi *etal*. in a previous work of our group [190].

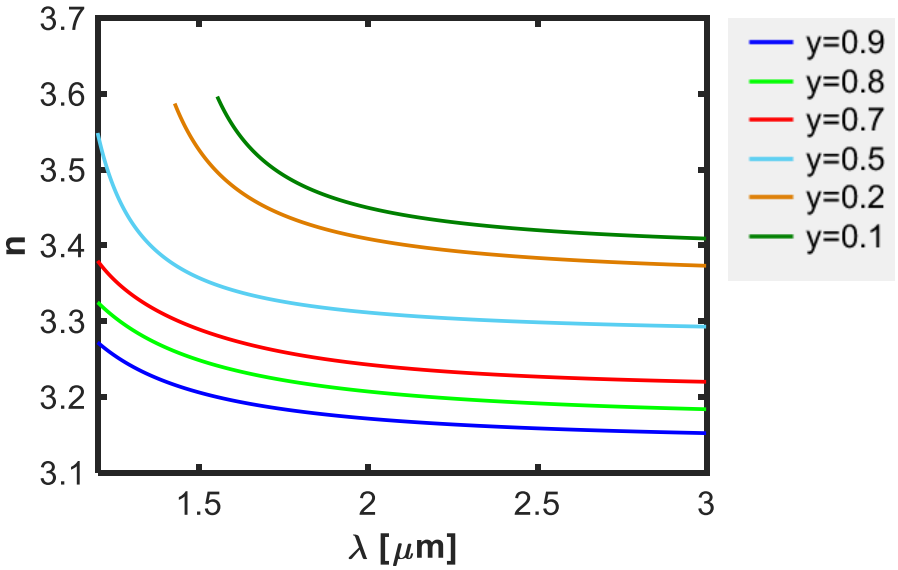

FIGURE 5.1: The refractive index dispersion for $In_{1-x}Ga_xAs_{1-y}P_y$ with different concentrations of P. This figure is reproduced from Ref. [106].

.

5.1.1 Strip-loaded waveguides

InGaAsP Strip-loaded waveguides are composed of three epitaxial layers in which the InGaAsP layer is sandwiched between two InP layers with a lower refractive index, see Fig. 5.2 (a). Therefore, the InGaAsP layer and the two InP layers act as the guiding layer and claddings, respectively. This configuration provides vertical confinement of light inside the core. The horizontal confinement is ensured by a ridge part on the top of the upper cladding. Strip-loaded waveguides exhibit low propagation loss coefficients because the waveguide core is not affected by the etching process [190]. However, for the strip-loaded waveguides, the dispersion engineering is challenging because the waveguide dispersion in such structures is very small compared to the material dispersion [92]. Further, strip-loaded waveguides have relatively large dimensions due to the moderate refractive index contrasts experienced by the guided modes in vertical and horizontal directions, and the resulting effective-mode areas are relatively large, which prevents achieving high intensities at small input power in the waveguides.

5.1.2 Nanowires

To address some of the issues of strip-loaded waveguides, Meier et al. [51] proposed a different waveguide geometry known as nanowire (see Fig. 5.2

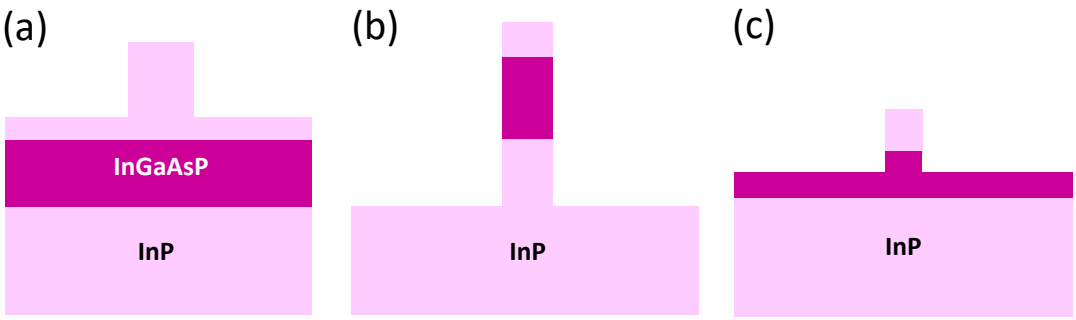

FIGURE 5.2: Different waveguide geometries for three-layer heterostructure waveguides: (a) strip-loaded waveguides, (b) nanowires, (c) half-core waveguides. The InGaAsP layer and the InP layers in all three types of waveguides act as the core and claddings, respectively.

(b)), in which the width of the waveguide ridge is relatively small (less than 1 µm) and the etch depth typically goes down deeply into the lower cladding. Therefore, this type of waveguides allows one to achieve a smaller effective mode area (< 0.5 µm^2) or a higher nonlinear coefficient. Another advantage of this waveguide geometry is that it offers flexibility in dispersion engineering because the waveguide dispersion becomes significant in such compact structures. Zero-GVD points have been demonstrated in this waveguide geometry in the Telecom C-band [51], [93]. However, due to the deep etching process and sharp refractive index contrast of the sidewalls with the surrounding air, this waveguide geometry can exhibit high propagationloss [93].

5.1.3 Half-Core Waveguides

By etching the nanowire's core half-way, a waveguide geometry can be obtained that is a trade-off between the strip-loaded and nanowire geometries, see Fig. 5.2 (c). Such a design exhibits a reduced propagation loss compared to the nanowire waveguides and a smaller effective mode area compared to the strip-loaded waveguides [93], thereby representing a compromise solution between the two aforementioned waveguide geometries. This waveguide geometry is known as half-core; it has been recently proposed and demonstrated by our research group in AlGaAs waveguides [189]. It typically exhibits the effective mode area of less than 2 µm^2 [189].

5.2 Design strategies: zero GVD and composition selection

In this section, we describe how we performed our initial design of two types of waveguides. It is remarkable that the original plan was to work with strip-loaded and nanowire waveguide geometries. It was not until recently that our group has proposed the half-core waveguide geometry, and the design was originally performed for the other two geometries. However, in the process of nanofabrication, we ran into a technical issue that forced us to etch our originally designed strip-loaded waveguides deeply, so that we ended up with half-core waveguides in practice. That is why **we present the waveguide design for the strip-loaded and nanowire geometries, but the experimental results for the half-core and nanowires.**

Our goal in designing the nanowire and strip-loaded waveguides was to minimize the GVD effect. Generally, waveguide design depends on three factors, namely waveguide geometry, dimensions, and the material composition. The nanowire design can exhibit zero GVD (ZGVD), however, in the case of strip-loaded waveguides, due to the lack of flexibility in dispersion engineering, it is not possible to achieve ZGVD. Another concern for these designs is the composition selection. We examined different compositions of phosphorous (y) in the waveguide core material ($In_{1-x}Ga_xAs_{1-y}P_y$) to achieve ZGVD at 1550 nm through several simulations. Note that, as mentioned earlier, the composition x can be obtained through the lattice-matching condition *i.e.* $x = 0.47 - 0.47y$. Our simulations were performed using Lumerical mode solution. For this purpose, the first step is to find the effective refractive index in a certain wavelength interval, then the dispersion parameter (D) can be obtained from Lumerical. Finally, the GVD is calculated from Eq. (4.10) using MATLAB. For all the simulations, we used perfectly matched layers (PML) as the boundary conditions. Our results demonstrate that ZGVD and small GVD become achievable for the nanowire and strip-loaded geometry, respectively, for the material composition $y = 0.7$, $x = 0.14$ and certain geometrical dimensions, as described in Table 5.1 and Fig. 5.3.

From performing several simulations for the case of nanowire with different widths (w), it can be realized that the ZGVD wavelength can be controlled well by changing the width of the nanowire waveguide, see Fig. 5.4 (a). Our simulation results have demonstrated that a blue-shift of ZGVD wavelength occurs with the reduction of the waveguide width, see Fig. 5.4 (a). It can be

Nanowire dimensions [μm]	Strip-loaded dimensions [μm]
height of the core = 0.8	height of the core = 0.5
width of the core = 0.5	upper cladding height = 0.1
upper cladding height = 0.3	ridge height = 0.9
lower cladding height = 0.6	ridge width = 1.5

TABLE 5.1: The geometrical dimensions of the $In_{0.86}Ga_{0.14}As_{0.3}P_{0.7}$ nanowire and strip-loaded waveguides for achieving ZGVD and small GVD, respectively (in the case of the strip-loaded waveguide, the main effective factor on GVD is the material composition, not the geometrical dimensions).

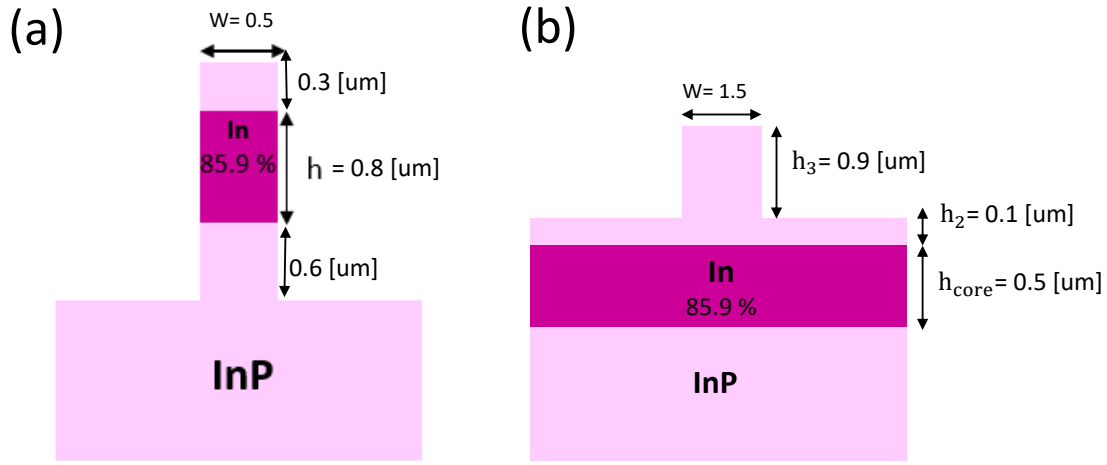

FIGURE 5.3: (a) The nanowire waveguide dimensions that allow one to achieve ZGVD around 1550 nm; (b) The strip-loaded waveguide dimensions that allow one to get small GVD. The material composition of $In_{1-x}Ga_xAs_{1-y}P_y$ is $y = 0.7$ and $x = 0.14$.

seen that for the width $w = 0.5$ μm and $h_{\text{core}} = 0.8$ μm the ZGVD around 1550 nm is achievable. For the strip-loaded waveguides, the GVD does not exhibit a significant change for different dimensions of the core and the ridge, see Fig. 5.4 (b). Note that for the case of the strip-loaded waveguide, the material composition has the main effect on the GVD, not the geometrical dimensions.

To obtain a better understanding concerning the role of the material composition in GVD engineering, we present the GVD variation as a function of wavelength for the composition $y = 0.5$ and $x = 0.23$. It can be seen from Fig. 5.5 (a) that for this composition, the ZGVD at $\lambda = 1550$ nm can be obtained at the expense of a narrower waveguide width ($w = 0.4$ μm for the case of nanowire), which is challenging from the fabrication point of view. For the case of strip-loaded waveguides, the GVD values for the composition

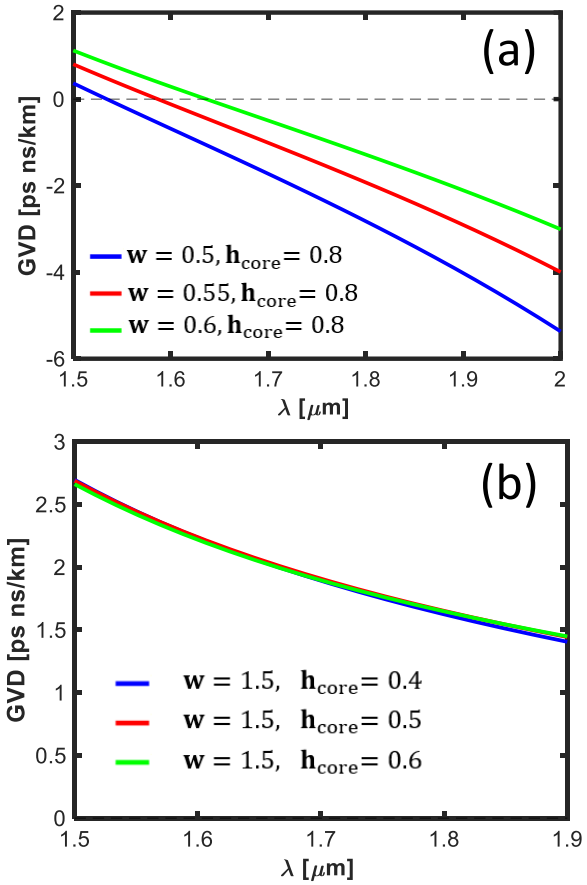

FIGURE 5.4: The group velocity dispersion diagrams ($In_{1-x}Ga_xAs_{1-y}P_y$ with the composition $y = 0.7$ and $x = 0.14$) with different widths and core heights for (a) nanowires, (b) strip-loaded waveguides. For the nanowire, ZGVD at 1.5 μm can be achieved for the waveguide width of 0.5 µm.

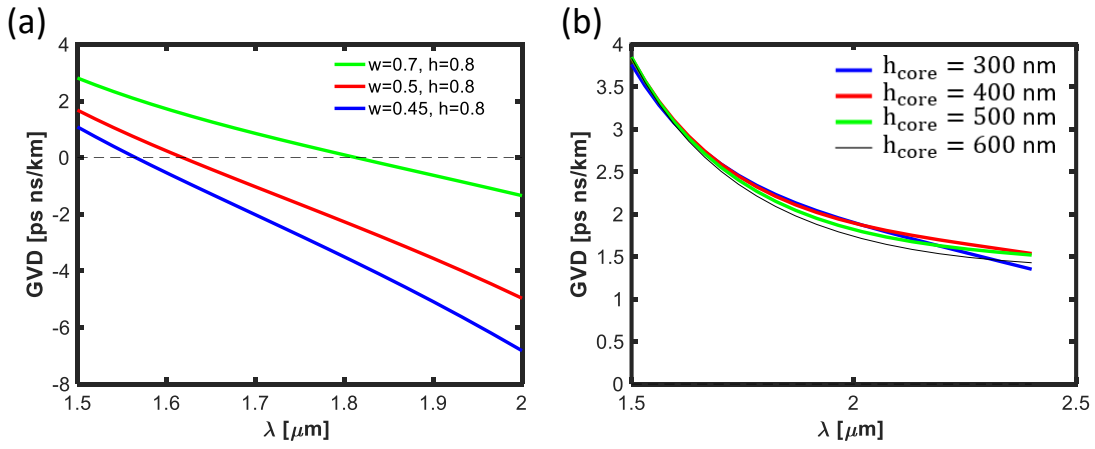

FIGURE 5.5: The group velocity dispersion diagrams ($In_{1-x}Ga_xAs_{1-y}P_y$ with composition $y = 0.5$ and $x = 0.23$) for (a) nanowires (b) strip-loaded waveguides. As can be seen from (a), the ZGVD at 1550 nm can be obtained for $w < 0.45$, which is challenging from the fabrication point of view.

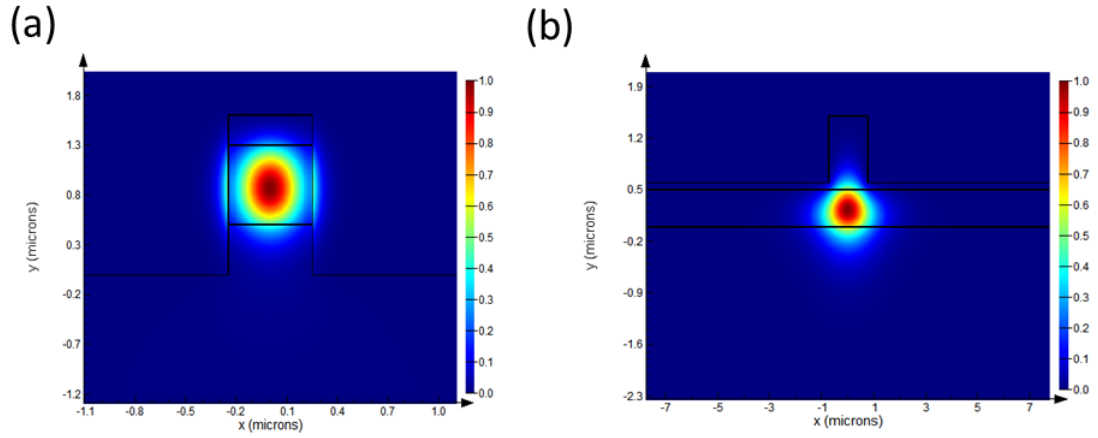

FIGURE 5.6: The fundamental TE mode profile (the electric field intensity) for (a) the nanowire and (b) strip-loaded waveguides. The effective mode areas are 0.39 μm^2 and 2.75 μm^2, respectively.

$y = 0.5$ become bigger than those for the composition $y = 0.7$, see Fig. 5.5 (b).

Based on the above reasons, we select the composition $y = 0.7$ and $x = 0.14$ in $In_{1-x}Ga_xAs_{1-y}P_y$ for our waveguide design.

Figure 5.6 (a)–(b) shows the electric field intensity (the fundamental mode profile) for the nanowire and strip-loaded waveguides, respectively, for the TE polarization. These modes exhibit the effective mode area of $A_{eff} = 0.39\,\mu m^2$ and 2.75 μm^2, respectively. As can be seen from this figure, a good light confinement can be obtained with the refractive index contrast of $\triangle n = 0.1$ between the $In_{0.86}Ga_{0.14}As_{0.3}P_{0.7}$ (core) and InP (cladding) at 1550 nm.

In practice, to couple light into and out of a nanowire waveguide, it is required to use tapered waveguides with the adiabatic change of the width, see Fig. 5.7 (a). Consequently, for the calculation of linear propagation loss in the waveguide, we need two extra waveguides known as taper-to-taper waveguide, see Fig. 5.7 (b), and reference waveguide with the width of the coupling regions, see Fig. 5.7 (c). These extra waveguides are useful for the characterization of the principal waveguides. In our chip, the width for the reference waveguide and all input/output coupling waveguides is 2 μm.

Figures 5.8 and 5.9 show the schematic representation of the designed waveguide chips with waveguides of different widths for the nanowire and the half-core waveguides, respectively.

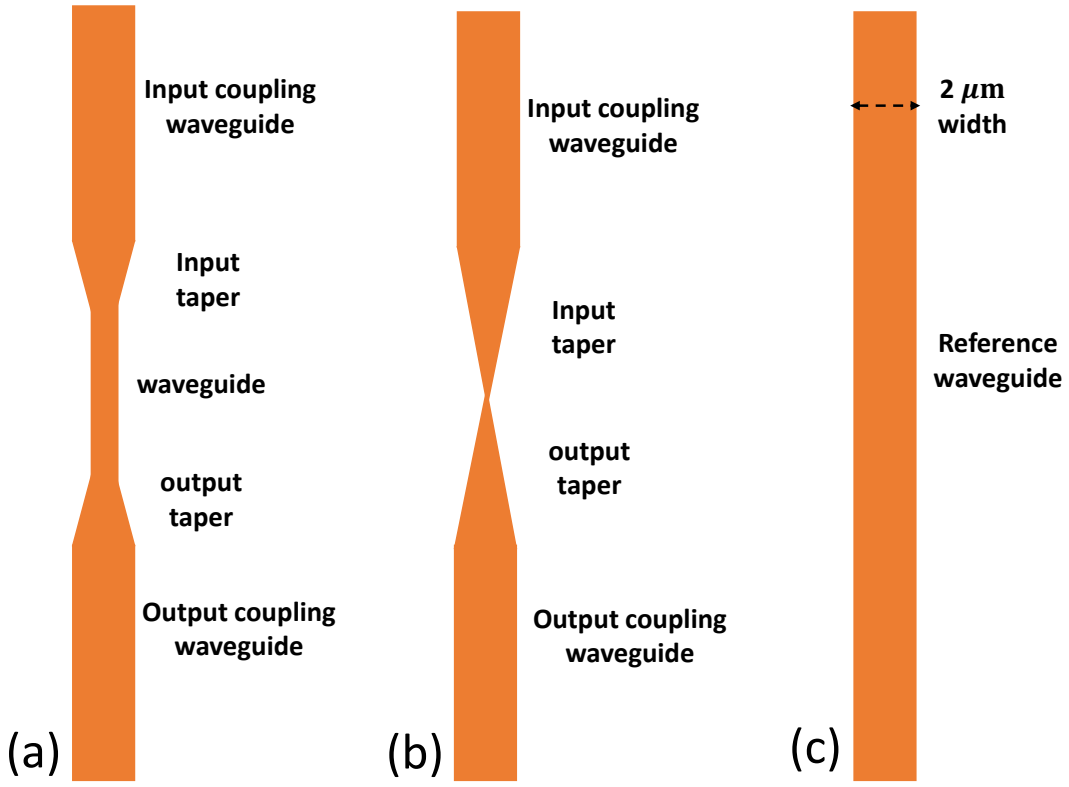

FIGURE 5.7: Schematic of (a) the nanowire waveguide structure, showing coupling-in and coupling-out 2-μm-wide regions, tapers, and the nanosection region with the dimensions corresponding to the design; (b) taper-to-taper structures that are used to evaluate the impact of the tapers, and (c) the reference waveguide with the width equal to that of the coupling regions (2 μm).

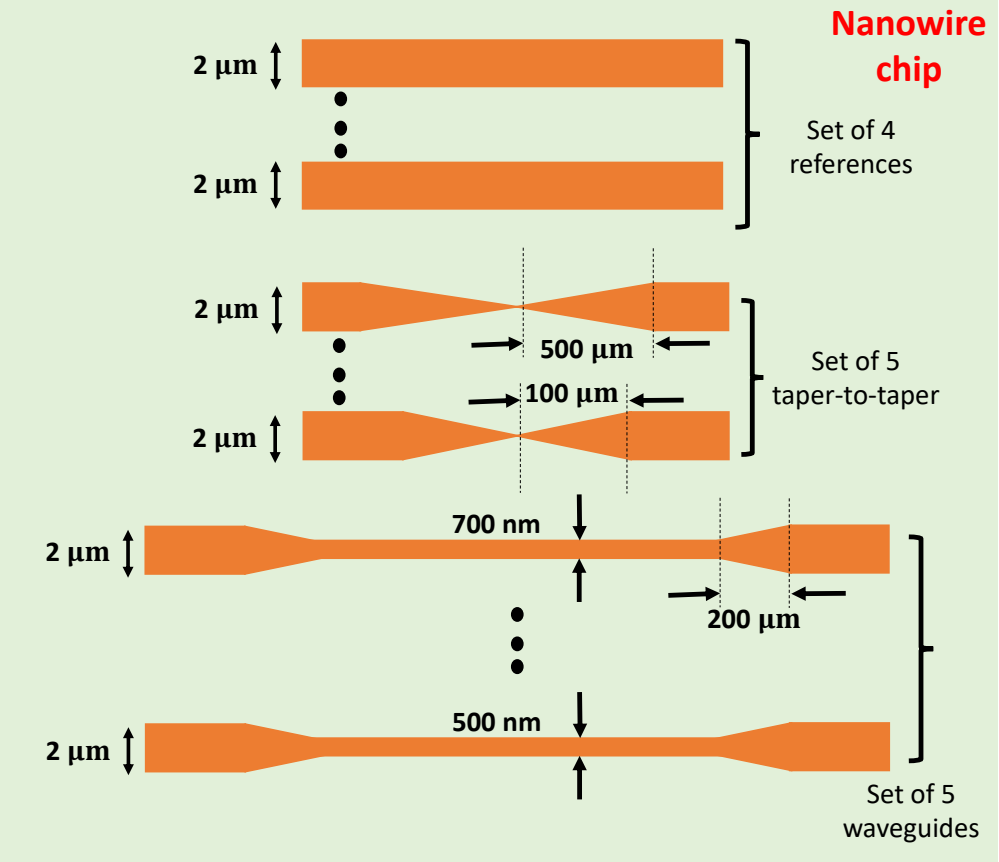

FIGURE 5.8: Schematic of the designed nanowire waveguide chip. The chip includes a set of reference waveguides with the widths matching the width of the coupling regions, a set of taper-to-taper waveguides, and a set of nanowire waveguides with different widths using coupling regions for coupling the light into and out of the waveguide and tapered sections for mode size conversion. A copy of all devices is repeated again on the bottom of the chip, which is not shown here.

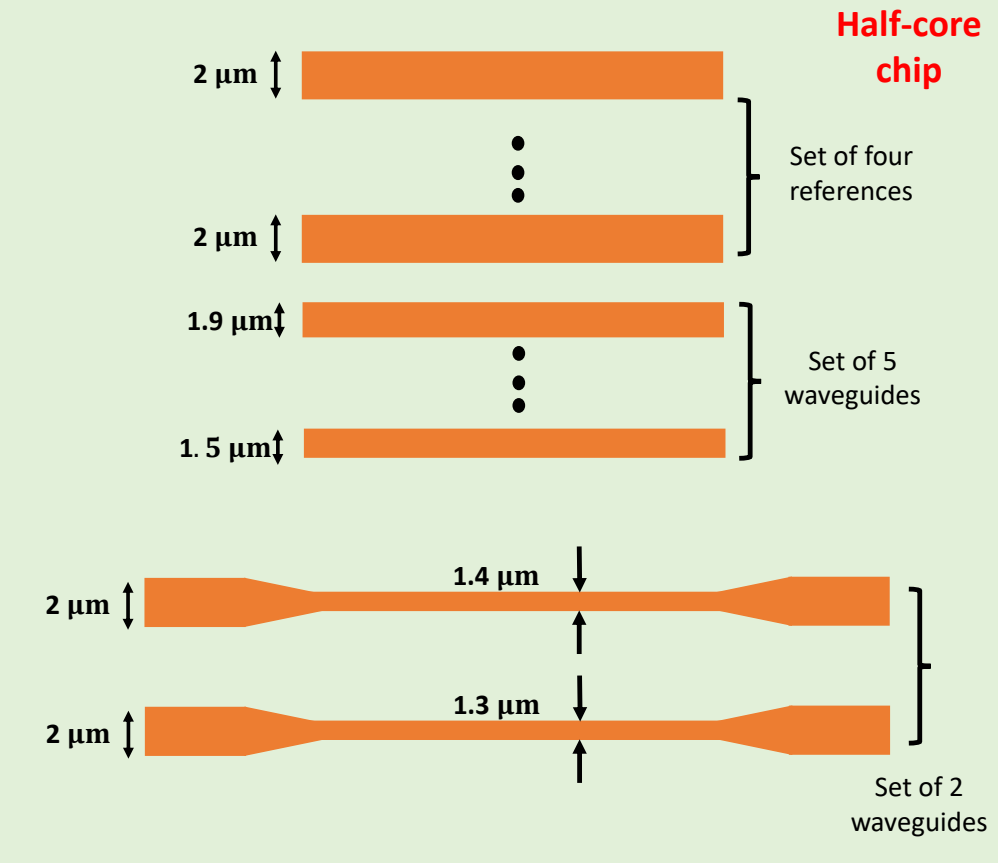

FIGURE 5.9: Schematic of the designed strip-loaded waveguide chip. The chip includes a set of reference waveguides with different widths ranging from 2 µm down to 1.5 µm, and a set of waveguides with narrower widths using tapered sections for coupling. A copy of all devices is repeated again on the bottom of the chip, which is not shown here.

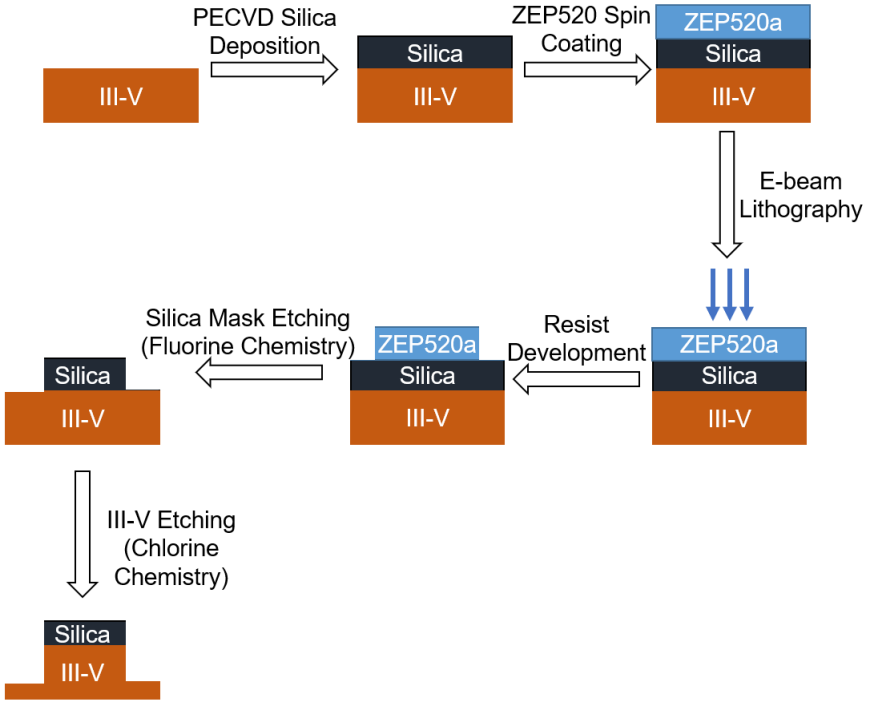

FIGURE 5.10: Process flow used for fabrication of InP waveguides. The image was created by Kaustubh Vyas [179].

5.3 Fabrication

The first step in fabricating any integrated photonic structure is finalizing the epitaxial stack. Based on the design considerations introduced in Section 5.2, the epitaxial stacks were grown using Metal Organic Chemical Vapor Deposition (MOCVD) process. The growth was performed at Sandia National Laboratories in the USA as part of the collaborative program ran by the Center for Integrated Nanotechnologies (CINT). The epitaxially grown wafers were cleaved into 1 cm $\times$ 1 cm pieces. The fabrication process followed a standard top-down approach, as described further.

Wafer cleaning is a key process before starting any fabrication run. The pieces were cleaned in warm acetone and Isopropyl alcohol (IPA) followed by blow drying with nitrogen. Since the etch depth requirements for the designed waveguides were rather large, it would have been impossible to have reached the required etch depth with a soft mask or an E-beam resist only. Therefore, we decided to use a silica hard mask for transferring the pattern into the underlying InP/InGaAsP layers.

Fig. 5.10 shows the process flow used to fabricate the waveguides. Silica

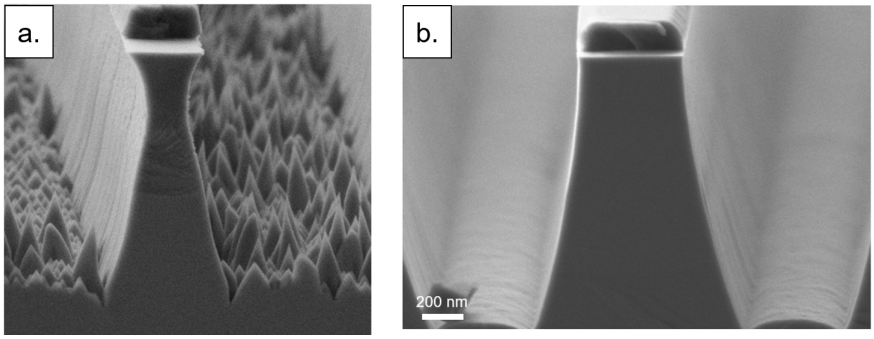

FIGURE 5.11: Plasma etching results for InP etching: (a) InO_x formation leading to poor surface roughness; (b) Optimized etching recipe with improved surface roughness

mask of the thickness 320 nm was deposited on top of the clean wafers using an optimized LPCVD process. Positive-tone E-beam resist ZEP520a was then spin-coated on top of the deposited silica at a spin speed of 2000 rpm, which resulted in a 500-nm-thick resist layer. The waveguide patterns were then written using E-beam lithography. Two E-beam systems were used in this process. The nanowire sample was written using the 100 kV E-beam system at the University of British Columbia by our collaborator Dr. Kashif Awan. The half-core waveguides and the etch-test samples were written by Kaustubh Vyas using the 30 kV E-beam lithography system at uOttawa.

The patterned structures were further cleaved into smaller 3 mm$\times$ 3 mm pieces which were used as etch-test samples. The pattern transfer was performed by an ICP-RIE plasma etcher and a two-step etch process: first, to etch the silica mask using ZEP, and second, to etch InP using the silica mask. Plasma etching of Indium phosphide is not extensively studied, and is known to be relatively tough due to the high chamber temperature requirements [198], [199].

Another common occurrence while etching InP is Indium Oxide (InO_x) formation as shown in Fig. 5.11 (a). This leads to needle-like formation which therefore leads to optical losses due to intolerable surface roughness. In order to optimize the etching recipe to obtain the minimum surface roughness, we had to compromise the sidewall verticality. However, based on the revised simulations, we were still able to obtain light guiding even when the sidewalls were slightly angled and therefore we decided to proceed to the fabrication using the non-vertical sidewalls. Fig. 5.11 (b) shows the final fabricated device for the half-core etched waveguide. By comparing Fig. 5.11 (a) and Fig. 5.11 (b), the improvement in the surface roughness is very evident.

The detailed study of plasma etching of silica using ZEP and etching InP using silica mask has been carried out by Kaustubh Vyas in his PhD thesis [179].

5.3.1 Fabricated waveguides for the experimental characterization

There exist two types of E-beam resists used for patterning the devices: a positive-tone and a negative-tone resist. The role of each type of resist in the fabrication process is shown in Fig. 5.12. The negative-tone resist is hardened by the E-beam exposure process. In the process of development, the unexposed resist regions get washed away by the developer while the exposed resist remains, serving as a mask for the etching process. In contrast, the positive-tone resist becomes weakened by E-beam, so that the exposed regions are washed out by the developer and the unexposed regions stay, serving as a mask for etching.

The waveguides of the kind described in the section 5.1 are usually fabricated using negative resists in order to minimize the E-beam writing time. The preferred kind of negative-tone resists is HSQ which turns into silica glass under the E-beam exposure. It serves as a good alternative to silica hard mask in the etching process. However, HSQ has a disadvantage of a very short shelf life, long commercial lead times and high price. As a result, at the time of sample fabrications, for the interest of time, we decided to use the positive-tone resist ZEP that was readily available in the cleanroom at uOttawa.

In Fig. 5.13, we demonstrate how the E-beam exposure needs to occur in order to obtain the desired waveguide structures in the end. The top part of the figure demonstrates the E-beam exposure of the waveguide structure for the case when the negative-tone resist is used. The region that must be exposed by the E-beam is the waveguide itself, while the surrounding unexposed regions will be washed away by the developer. The bottom part of Fig. 5.13 shows the E-beam process for the case where a positive-tone resist is used. In this situation, the regions that will be exposed are the trenches surrounding the waveguide structure as it is those regions that need to be removed by the developer. In order to reduce the E-beam writing time, the trenches should be as narrow as possible. On the other hand, if the trenches are too

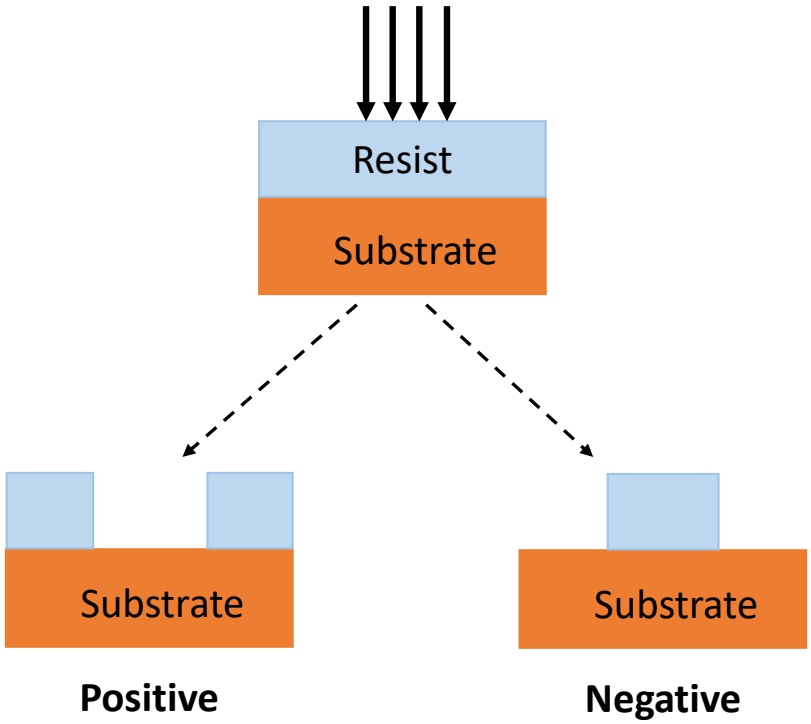

FIGURE 5.12: Schematic that shows the principle of E-beam writing with a positive (left) and negative (right) resist. The arrows on the top show the E-beam exposure.

narrow, it will be difficult to excite the waveguide mode without exciting the surrounding slab mode, and the coupling efficiency will be very small.

In our study, as we mentioned earlier, we had to rely on the positive-tone resist ZEP because it was readily available in the cleanroom. As a result, the E-beam exposure was performed in line with the description on the bottom part of Fig. 5.13. As a result, at the end of the fabrication process, there were lateral slabs remaining in addition to the designed waveguides, see Fig. 5.14. These slabs complicated the process of light coupling to the right waveguide mode, posing difficulty in discriminating between the real guided mode and the slab modes.

The coupling objective lens in our experiment is expected to focus the beam to the spot diameter around 2 μm. However, in reality, the focused spot size is larger due to the following reasons: first, the beam is not an ideal Gaussian beam, and second, there is some scattering from the sidewalls of the waveguide, and the radiation partially scatters into the slab mode. For the case of strip-loaded waveguide, to increase the discrimination between the waveguide mode and the slab modes, we etched the waveguide further

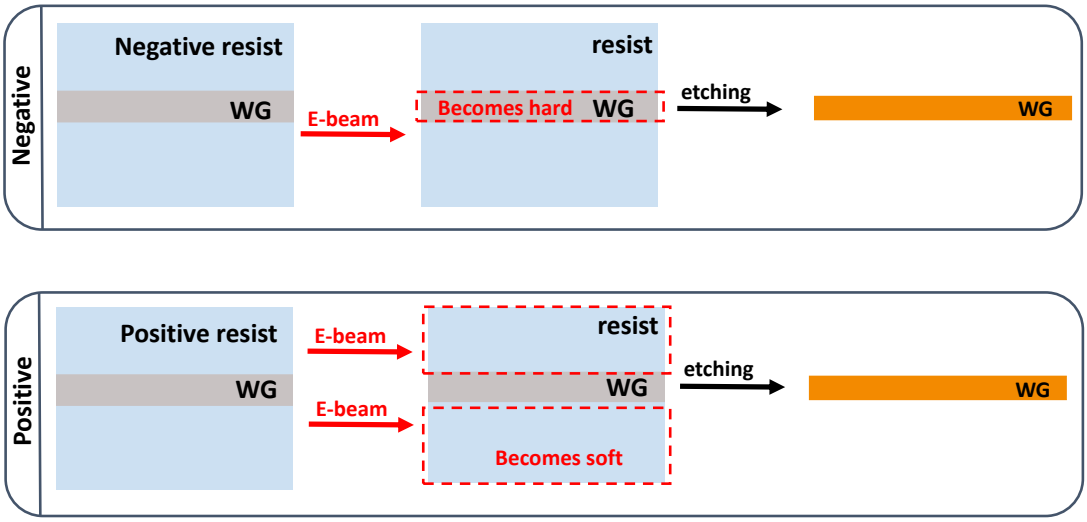

FIGURE 5.13: The top view of the waveguide for the E-beam and etching process with negative (top of the picture) and positive (bottom of the picture) resist. In order to minimize the E-beam writing time, narrow trenches surrounding the waveguide structures were written (see the bottom part).

to end up with half-core waveguides with a smaller effective mode area instead of the originally designed strip-loaded waveguides. Etching deeper facilitated the coupling of light to the desired waveguide mode without a lot of cross-talk with the slab modes. However, only 2-µm-wide waveguides worked for the fabricated half-core chip. Also, for the case of the nanowire, the coupling only into the reference waveguides was possible (only 2-m-wide deeply etched nanowires exhibited light guidance, there were no narrow devices that worked). For the rest of this thesis, we will focus on describing the experimental results that we have obtained with the 2-m-wide half-core and nanowire waveguides that permitted a reliable light coupling and fundamental mode excitation.

Once the waveguide samples were fabricated and SEM images of the waveguides were recorded, we were able to gather the real waveguide parameters for our experimental studies. Since the sample characteristics deviated largely from the targeted design, we found it important to repeat the mode analysis to obtain the realistic mode profiles of as-made structures together with the effective mode area, effective refractive indices and dispersion characteristics. As previously, we used Lumerical Mode Solutions for the modal analysis of the as-fabricated structures.

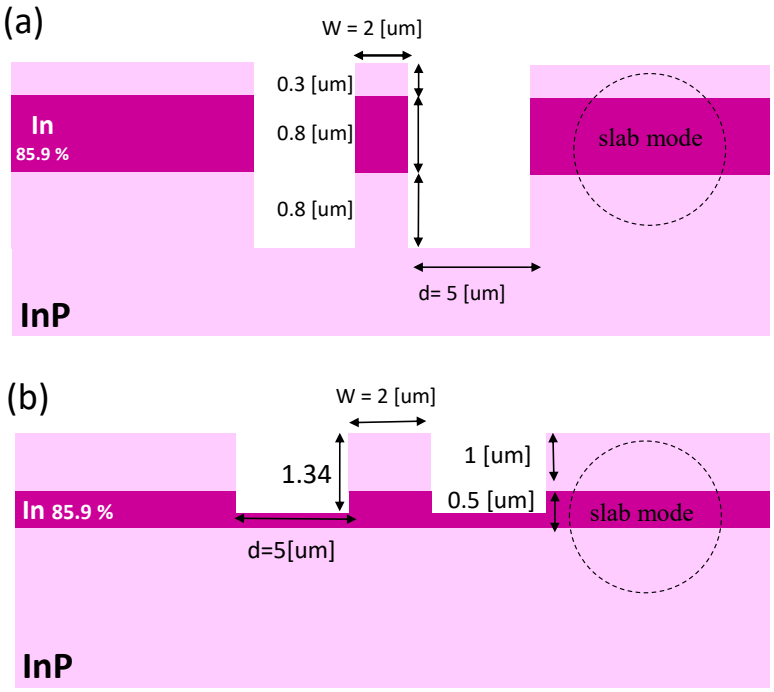

FIGURE 5.14: The schematic showing the side-view of the fabricated waveguides used in our experiment: (a) nanowire, (b) half-core waveguides. The circle shows the region where the slab modes appear.

Figure 5.15 shows the field distribution for the nanowire and half-core waveguides for the TE and TM polarizations. The strip-loaded waveguide exhibits fundamental TE and TM modes, while the nanowire becomes multimode (for the 2-µm waveguide widths that exhibit light guidance). The simulation reveals that the 2-µm-wide nanowire waveguides support two lowest-order modes with close effective refractive indices, see Fig. 5.15. (c)–(d). However, for the case of the half-core waveguide, we are still able to work in the single-mode regime, see Fig. 5.15 (e)–(f).

Table 5.2 shows the effective refractive indices and effective mode areas for the modes supported by the fabricated waveguides. For the nanowires, two values of each parameter are reported, corresponding to the fundamental (TE_{00}, TM_{00}) and the first-order (TE_{01}, TM_{01}) modes, respectively. In Fig. 5.16, we show GVD diagrams obtained from the repeated simulations for the fabricated nanowire and half-core waveguides (both TE and TM polarizations). As can be seen from Fig. 5.16 (a), the ZGVD around the wavelength 1550 nm cannot be obtained for the as-fabricated waveguides width the width of 2 µm.

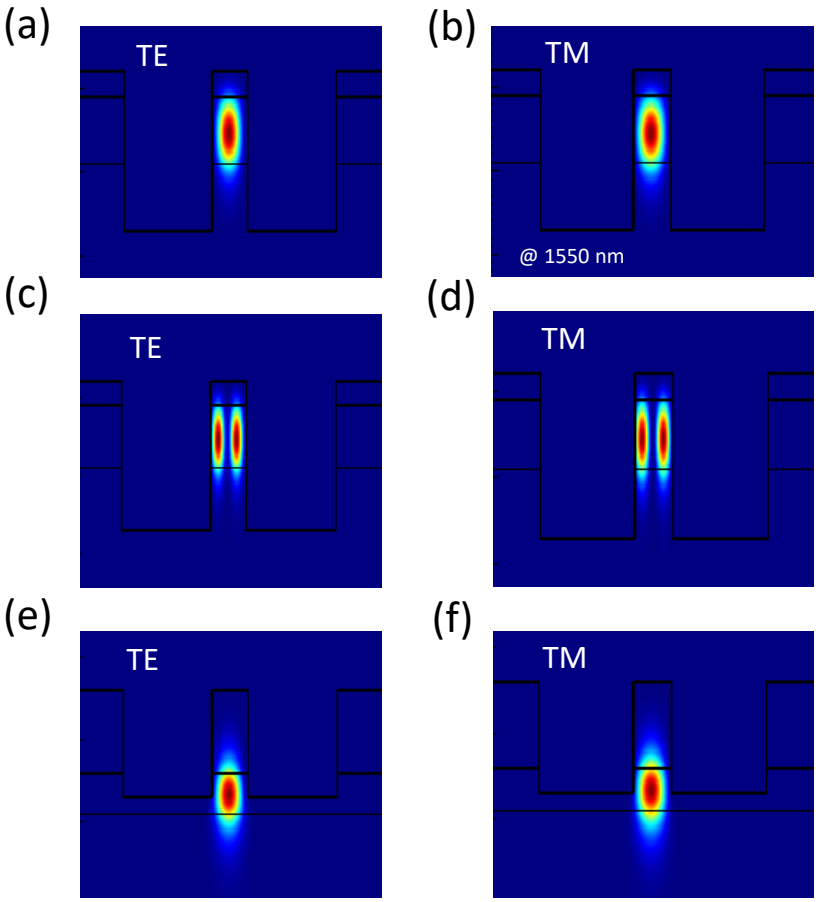

FIGURE 5.15: The mode profiles (electric field intensity distributions) of (a)–(d) nanowire and (e)–(f) half-core waveguide for different polarizations at 1550 nm.

Waveguide type	Refractive index (TE/TM)	Effective mode area (TE/TM)
Nanowire	3.20, 3.13 / 3.24, 3.14	1.39, 1.42/ 1.46, 1.54 μm^2
Half-core	3.19/ 3.19	1.67/ 1.75 μm^2

TABLE 5.2: The effective refractive indices and effective mode areas for the fabricated waveguides. Two values of the parameters for the nanowires correspond to the fundamental (TE_{00} and TM_{00}) and the higher-order (TE_{01} and TM_{01}) modes.

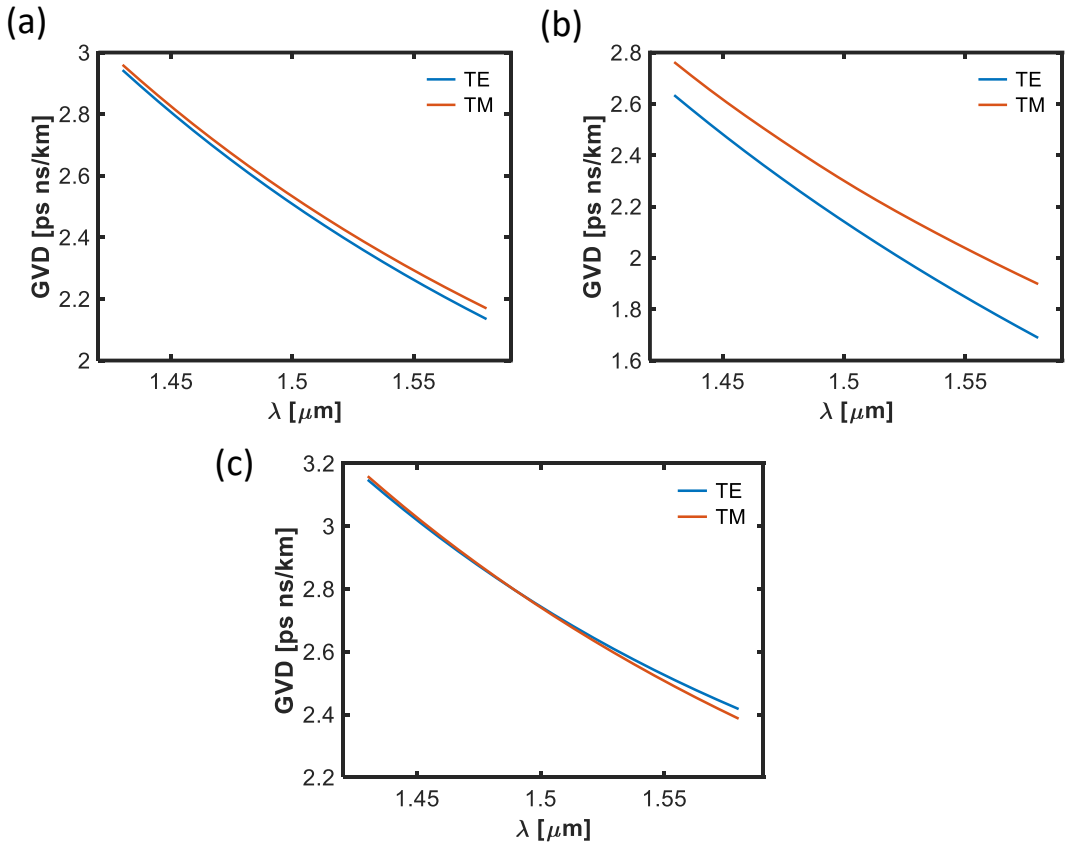

FIGURE 5.16: The GVD as a function of wavelength for as-fabricated waveguides: (a) for the fundamental TE and TM modes of the nanowires, (b) for the TE_{01} and TM_{01} modes of the nanowires, (c) for the fundamental TE and TM modes of the half-core waveguides.

5.4 Measuring the propagation loss of the waveguides

To measure the propagation losses of our waveguides, we use the Fabry-Perot method based on the successive reflections from the waveguide facets [200], see Fig. 5.17. Let us denote the reflection and the transmission coefficients as R and t, respectively. The optical waves undergo a reflection at each interface and an attenuation at each roundtrip, and the total transmission coefficient (T) can be obtained through the superposition of all transmitted waves as [201]

$$T = \frac{(1-R)^2}{4R\sin^2(\beta L) + (e^{2\alpha L} - R)^2}, \tag{5.1}$$

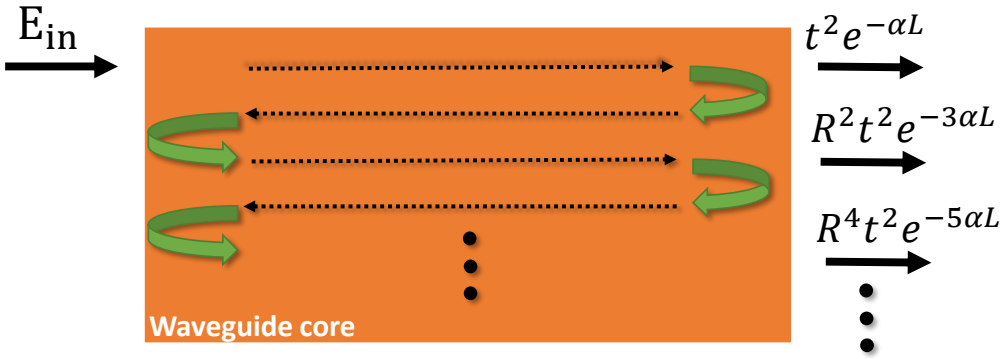

FIGURE 5.17: Schematic that shows the top view of a waveguide core. The arrows represent successive reflections from the waveguide facets known as Fabry-Perot reflections. The parameters t, R, α, and L denote the transmission coefficient, reflection coefficient, linear loss coefficient, and the length of the waveguide, respectively.

where β is the propagation constant of the waveguide, and α is an attenuation coefficient. The transmission T oscillates as a function of wavelength based on the phase of the amplitude reflection and transmission coefficients, thereby exhibiting Fabry-Perot spectral fringes. The ratio of maximum and minimum transmission can be found from the above equation as

$$\frac{T_{\text{min}}}{T_{\text{max}}} = \frac{\left(1 - e^{-2\alpha L} R\right)^2}{\left(1 + e^{-2\alpha L} R\right)^2}. \tag{5.2}$$

From the above equation, the linear loss coefficient can be obtained as

$$\alpha = \frac{1}{L} \ln\left(R \frac{1 + \sqrt{\frac{T_{\text{min}}}{T_{\text{max}}}}}{1 - \sqrt{\frac{T_{\text{min}}}{T_{\text{max}}}}} \right). \tag{5.3}$$

note that the value of $T_{\text{min}}/T_{\text{max}}$ can be determined from the measurements. The linear loss coefficient of an optical waveguide is conventionally expressed in the units of dB/cm and can be related to the loss coefficient in the units of 1/cm as

$$\alpha\,[\text{dB/cm}] \simeq 4.34\,\alpha\,\left[\text{cm}^{-1}\right]. \tag{5.4}$$

In our experiment, the loss is measured by coupling a laser beam from a tunable continuous-wave (cw) laser into the waveguide and measuring the

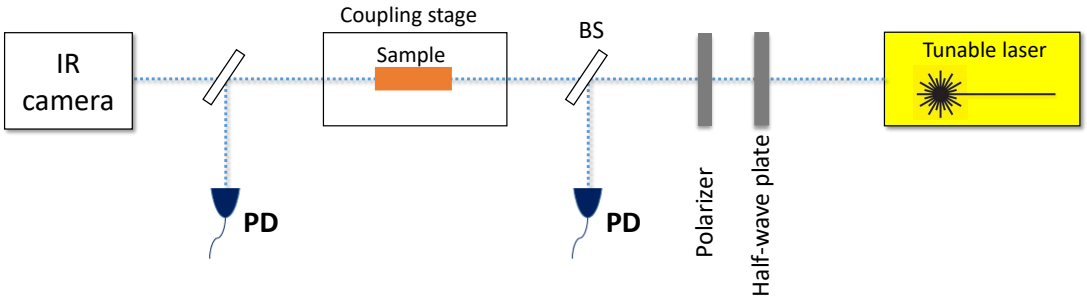

FIGURE 5.18: Schematic of the linear characterization setup. "BS" stands for beam splitter.

output power variation as a function of wavelength. Figure 5.18 shows the schematic of the experimental setup for the loss measurement. The tunable laser Santec TSL-710 was employed in the experiment. Two microscopic objectives were used to couple the laser beam in and out of the waveguide. The measurement is performed at the wavelength range around 1550 nm. The laser beam was coupled into the waveguide via a microscopic objective, and the output power was measured as a function of wavelength using a wavelength sweep in the wavelength interval 0.6 nm.

Figure 5.19 shows the output power of the half-core waveguide as a function of wavelength for the TE and TM polarizations. The length of the waveguide was 0.2 cm. The linear propagation loss for the TE and TM fundamental modes has been determined from the measurements as 13.7 dB/cm and 13.8 dB/cm, respectively. Table 5.3 shows the summary of the loss measurement results for the half-core and nanowire waveguides.

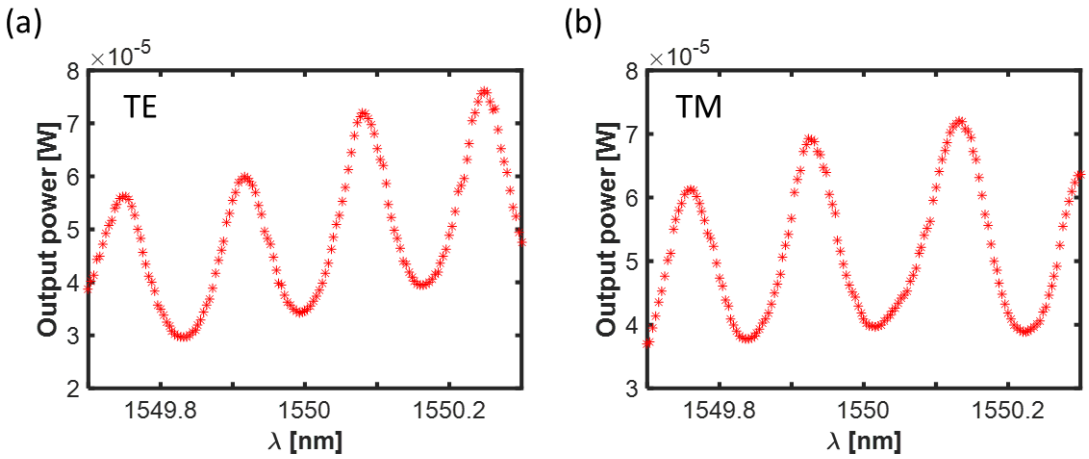

FIGURE 5.19: Experimentally measured output power as a function of wavelength used for the calculation of the linear propagation loss (α). (a) The data for the TE polarization. The linear loss coefficient extracted from this data is 13.7 dB/cm. (b) The data for the TM polarization. The extracted propagation loss coefficient is 13.8 dB/cm.

Waveguide (polarization)	Propagation loss (α)
Half-core (TE)	13.7 dB/cm
Half-core (TM)	13.8 dB/cm
Nanowire (TE)	27.6 dB/cm
Nanowire (TM)	23.2 dB/cm

TABLE 5.3: The results of the linear propagation loss measurements in the half-core and nanowire waveguides for the TE and TM polarizations. The loss measurements reported for the nanowires are for the superposition of the fundamental and first-order spatial modes for each polarization.

5.5 Calculation of the coupling factor

Once the linear propagation loss is measured, it is possuble to determine the fraction of the optical power coupled into the waveguide. The coupling factor (K) can be calculated from the linear propagation loss coefficient (α) and the reflection coefficient of the waveguide facets (R) as

$$P_{\text{in}}(0) = K(1-R)P_{\text{inc}}, \tag{5.5}$$

where P_{inc} and P_{in} represent the incident optical power and the coupled-in power right at the input inside the waveguide, respectively, see Fig. 5.20. The

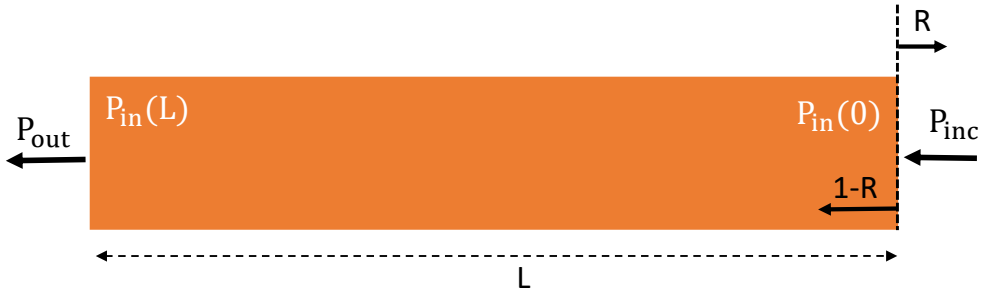

FIGURE 5.20: Schematic that represents the process of transmission and shows how coupling factor K is related to the incident and transmitted optical power. The parameter R denotes the power reflection coefficient at the waveguides' facets.

parameter R denotes the reflection coefficient for the power at the waveguides' facets. Therefore, the portion of the light that enters the waveguide is $K(1-R)$. The portion due to coupling factor K can be associated with the coupling loss ($L_{coupling}$ expressed in dB) as

$$L_{coupling} = L_{total} - 2L_{ref} - L_{prop}L, \tag{5.6}$$

where L_{total}, L_{ref}, and L_{prop} represent the total loss, reflection loss in dB per facet and the propagation loss per unit length in dB/cm. The parameter L denotes the length of the waveguide in cm. The optical power after propagating the length L inside the waveguide with the linear propagation loss coefficient α ($P_{in}(L)$) can be expressed as

$$P_{in}(L) = K(1-R)\,P_{inc}e^{-\alpha L}, \tag{5.7}$$

while the output power (P_{out}) can be expressed as

$$P_{out} = P_{in}(L)(1-R). \tag{5.8}$$

Therefore, we can express K as

$$K = \frac{P_{out}}{P_{inc}e^{-\alpha L}(1-R)^2}. \tag{5.9}$$

For instance, the coupling factor for the half-core waveguide (TM polarization) is obtained as 0.2, (which is associated with the coupling loss of 6.9 dB)

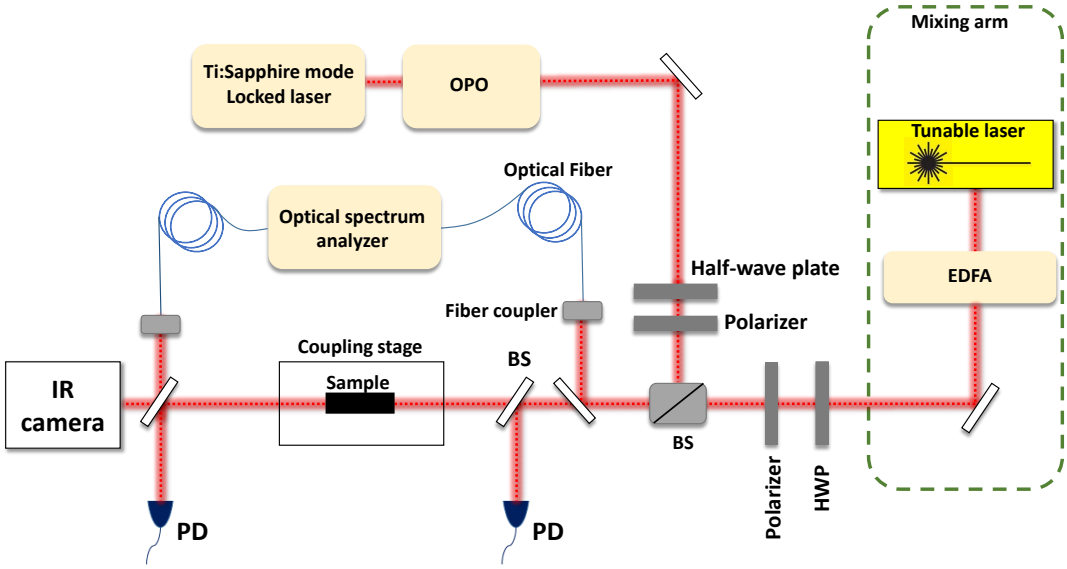

FIGURE 5.21: Schematic of the nonlinear characterization setup used for the FWM and SPM measurements. The SPM experiment is performed without the mixing arm.

while the P_{inc} and P_{out} are obtained from the measurement, and the waveguide length is 2 mm. The value of the coupling factor for the TE fundamental mode is close to 0.2.

5.6 Nonlinear characterization of the waveguides

The experimental setup that we employed for the nonlinear characterization i.e., FWM and SPM measurements is shown in Figure 5.21. The pump source in our setup is a Coherent optical parametric oscillator (OPO) which is pumped by a Ti:Sapphire laser (Mira, made by Coherenc Inc.) emitting light at the wavelength 800 nm. The OPO generates optical pulses with a 3-ps FWHM duration and a repetition rate of 76.6 MHz (in the wavelength range of 1420 nm to 1560 nm for our experiments). Regarding the signal source, we employed the Santec TSL-710 cw tunable laser which is then amplified by an erbium-doped fiber amplifier (EDFA- made by Amonics) up to 2 W. The operation wavelength range of EDFA is between 1535 and 1565 nm. The output of the EDFA is coupled to the free space from a fiber-connected collimator. Then, this light is combined with the OPO pump output through a non-polarizing 50% beam splitter. A polarising beam splitter (PBS) and a

half-wave plate (HWP), placed in each arm of the setup, adjust the polarisation of signal and pump beams. The pump and signal beams were simultaneously coupled into the fabricated chip placed in the coupling stage. The coupling into (from) the desired waveguide is performed using a 40× objective lens with a numerical aperture of 0.65 (20× objective lens with a numerical aperture of 0.4). Also, a reference photodetector is used to measure the power of the input beam before the coupling stage. The amount of power for the pump and signal is manually adjusted by rotating each corresponding half-wave plate (HWP). Based on this control, a maximum output of 130 mW (average power) can be obtained from the OPO. Finally, the output spectra can be measured and observed using an optical spectrum analyzer (OSA) (model AQ6315E). The light exiting from the optical waveguide is coupled to the OSA through a fiber-connected collimator.

5.6.1 Self-phase modulation (SPM)

Since InGaAsP exhibits the TPA effect in the operating wavelength of our experiment, it is necessary to consider the effect of TPA on the SPM. To this end, we briefly explain this effect here before describing the results of SPM obtained in our experiment.

Effect of two-photon absorption on the SPM

As it was mentioned earlier, the solution of NLSE (without TPA effect) in terms of the nonlinear phase shift can be written as

$$A\left(z.t\right) = A\left(0,t\right)e^{\frac{-\alpha}{2}z}e^{i\varphi_{\mathrm{NL}}}, \tag{5.10}$$

where $|A|^2$ represents the power and $\varphi_{\mathrm{NL}} = \gamma L_{\mathrm{eff}}\left|A\left(0,t\right)\right|^2$. For a Gaussian pulse of the amplitude A, we have

$$A(0,t) = A_0 e^{\frac{-\left(t-t_0\right)^2}{2\tau^2}}, \tag{5.11}$$

where τ is FWHM of the pulse. Therefore, for a Gaussian pulse, Eq. (5.10) can be written as

$$A\left(z,\,t\right) = A_0 e^{\frac{-\left(t-t_0\right)^2}{2\tau^2}} e^{\frac{-\alpha}{2}z}\exp(i\varphi_{\mathrm{NL}}(\max)e^{\frac{-\left(t-t_0\right)^2}{\tau^2}}), \tag{5.12}$$

where $\varphi_{NL}(max) = \gamma L_{eff} |A_0|^2$. However, this solution cannot describe the effect of TPA on the self-phase modulation. To this end, the NLSE with the TPA effect should be solved, which is expressed as follows [202]:

$$\frac{\partial A}{\partial z} + \frac{i\beta_2}{2}\frac{\partial^2 A}{\partial t^2} = -\frac{\alpha}{2}A + i\gamma |A|^2 A - \frac{\beta_{TPA}}{2A_{eff}} |A|^2 A, \tag{5.13}$$

in which the free-carrier effect is neglected and β_{TPA} is the TPA coefficient. Let us assume that β_2 in Eq. (5.13) is small. Then Eq. (5.13) has a solution in the form

$$A = \sqrt{P} e^{(i\phi - \alpha z/2)}. \tag{5.14}$$

Inserting this solution into Eq. (5.13) and solving for P and ϕ yields

$$P(L,t) = \frac{P(0,t)\, e^{-\alpha L}}{1 + \frac{\beta_{TPA}}{A_{eff}} P(0,t)\, L_{eff}} \tag{5.15}$$

and

$$\phi(L,t) = \left(\frac{\beta_{TPA}}{\gamma A_{eff}}\right)^{-1} ln\left(1 + \frac{\beta_{TPA}}{A_{eff}} P(0,t)\, L_{eff}\right). \tag{5.16}$$

Further, the phase ϕ in terms of $\varphi_{NL}(max)$ can be written as

$$\phi(L,t) = (2r)^{-1} \ln\left(1 + 2r\varphi_{NL}(max)\right), \tag{5.17}$$

where the parameter r is defined as

$$r = \frac{\beta_{TPA}}{2k_0 n_2}. \tag{5.18}$$

As can be seen from Eqs. (5.15) and (5.16), both the power and phase are dependent on the TPA effect. It can be deduced from the above analysis that the TPA has a detrimental effect on the self-phase modulation, and it can decrease the SPM-induced nonlinear phase shift. This effect becomes more pronounced at higher input intensities due to a logarithmic increase with intensity [202].

Calculation of the nonlinear phase shift

In order to deduce the nonlinear phase shift from the SPM experiment, SPM-broadened spectra have been recorded at the output of the half-core waveguides at different levels of the incident optical power (see Fig. 5.22). Part (a) of the figure displays the incident spectrum recorded at a very low incident power, while part (b) shows SPM evolution for different incident pump powers. As can be seen from the figure, some spectral broadening can be observed in the output spectrum from a half-core waveguide with increasing the pump power.

As can be seen from Fig. 5.22 (b), e.g. for the average incident power of 60 mW, another peak (on the right-side of the pulse) appears in the output spectrum which is due to the SPM effect. This broadening is asymmetric due to the asymmetric effect of TPA and other effects such as FCA and FCD [202].

To calculate the nonlinear phase shift, we use the Fourier transform of Eq. (5.14) as well as the curve fitting with MATLAB. Figure 5.23 shows the fitting of the Fourier transform to the output spectrum. The fitting was performed while assigning the following initial values to the free parameters used in the fit: $r = 0.09$ and the maximum nonlinear phase shift $\varphi_{NL}(\max) = 2\pi$. Based on the nonlinear phase shift 2π, the nonlinear refractive index on the order of 10^{-17} m^2/W can be estimated, which is in agreement with the value reported in Ref. [190]. We perform a more precise measurement of n_2 using the FWM method in Section 5.6.3.

Unfortunately, we lost the SPM effect after continuing our experiments with the waveguide for some time. It could occur due to the use of high input power at the beginning of the experiment that caused some damage at the waveguide entrance. It might have damaged the waveguide facet such that the coupling factor might have reduced and SPM was no longer observable.

5.6.2 Nonlinear absorption

As it was mentioned earlier in Chapter 4, InGaAsP exhibits the TPA effect in the wavelength range used in the nonlinear optical characterization. It is thus important to quantify the effect of TPA at the power levels used for the FWM experiment to be able to determine a power range where TPA has least impact on the useful results.

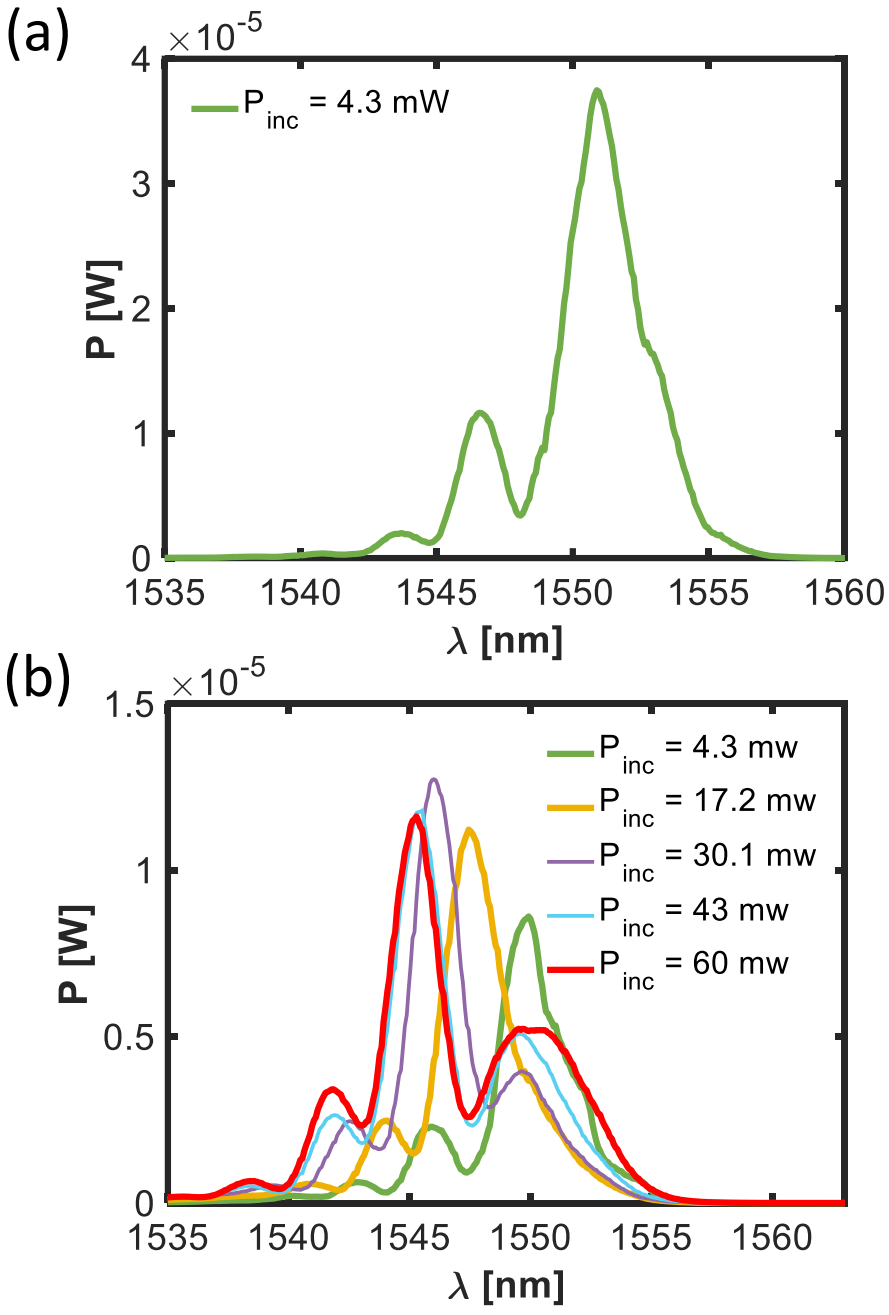

FIGURE 5.22: (a) The input spectrum for the average incident power of 4.3 mW. (b) The output spectra for different average incident pump powers. As can be seen, e.g. for the average incident power of 60 mW, another peak (on the right-side of the pulse) appears in the output spectrum. All spectra are plotted for the TM polarization.

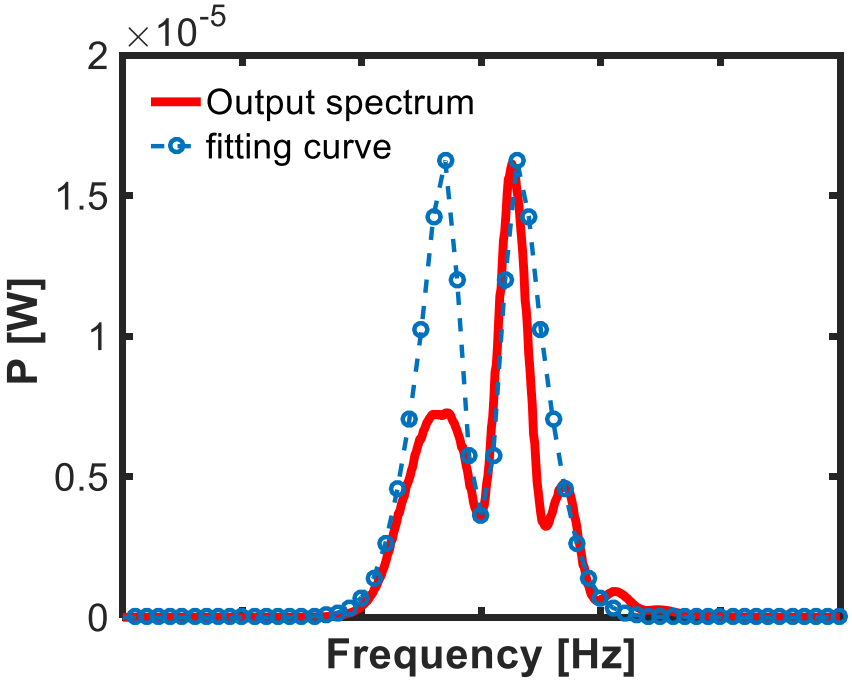

FIGURE 5.23: Calculation of the nonlinear phase shift from the SPM spectrum. The figure shows the output spectrum inside the half-core waveguide fitted with the absolute square of the Fourier transform of the pulse introduced in Eq. (5.14). The average incident power is 60 mW with TM polarization.

In order to experimentally determine the impact of TPA, we measure the power transmitted by a waveguide as a function of the average incident optical power (see Figure 5.24). The figure displays the power characteristics for the half-core (part (a)) and nanowire (part (b)) waveguides for the TE and TM polarizations. As can be seen from the figure, the power transmitted by both half-core and nanowire waveguides exhibits a nonlinear behavior with an increase in the pump power, which is the signature of nonlinear loss effects such as TPA, FCA, and FCD in our waveguides. It can be concluded that for the case of the half-core and the nanowire waveguide, the average incident powers of 17 mW and 4 mW, respectively, are relatively safe for the FWM experiment due to lower nonlinear saturation effect observable in the transmission diagrams at these power levels.

To calculate the TPA coefficient (β_{TPA}), we use the inverse transmission method [79], in which the slope of the inverse transmission as a function of the incident peak power is associated with the β_{TPA} as

$$\mathrm{Slope}\left(\frac{1}{T}\right) \equiv m = \frac{e^{\alpha L} L_{\mathrm{eff}}}{A_{\mathrm{eff}}\,(1-R)}\beta_{\mathrm{TPA}}, \tag{5.19}$$

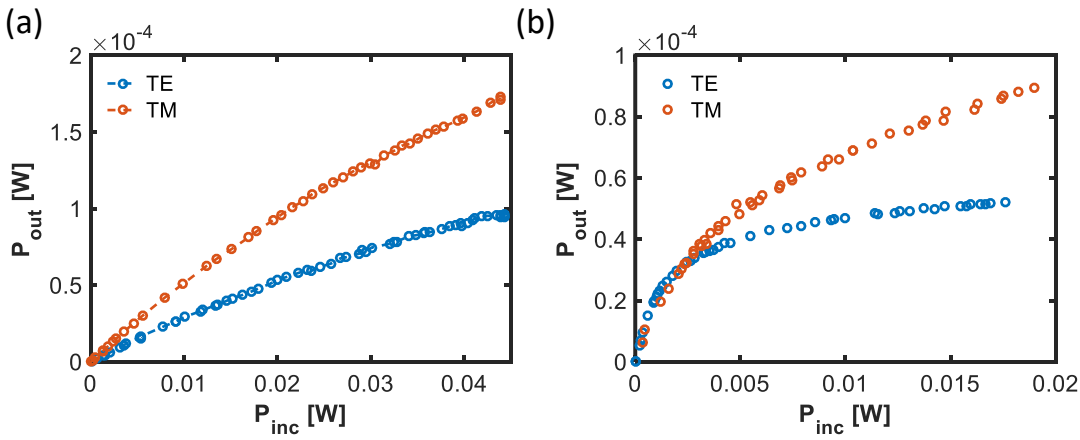

FIGURE 5.24: The power transmitted by (a) the half-core and (b) the nanowire waveguides as a function of the average incident power for TE and TM polarizations. The saturation behavior can be observed as a result of the nonlinear absorption.

where $T = P_{\text{out}}/P_{\text{inc}}$. Therefore, β_{TPA} can be calculated as

$$\beta_{\text{TPA}} = \frac{mA_{\text{eff}}\,(1-R)}{e^{\alpha L}L_{\text{eff}}}. \tag{5.20}$$

Based on the above equation and the plotted inverse transmission diagram for the half-core waveguide *e.g.*, for the TE polarization (see Fig. 5.25), the TPA coefficient can be calculated to have the value of 19 cm/GW. This obtained value for the TPA coefficient agrees well with the value reported in Ref. [190].

5.6.3 Four-wave mixing (FWM)

To explore the FWM effect, first, we started with the half-core waveguide with the reference device on the fabricated chip that showed the best linear performance and coupling of light. This step needs a very careful alignment of the pump and signal beams with respect to each other before they enter the coupling stage. A continuous monitoring of the IR camera is required to avoid the coupling of light to the lateral slab modes. When the light is coupled to the waveguide, the challenging task is to optimize the coupling of light to the OSA, especially since the FWM idler power is small. Therefore, after observing the idler spectrum on the OSA, we performed a very fine adjustment of the knobs on the coupling stage to optimize the idler level. This step is performed while the OSA is on the repetition mode and the scanning

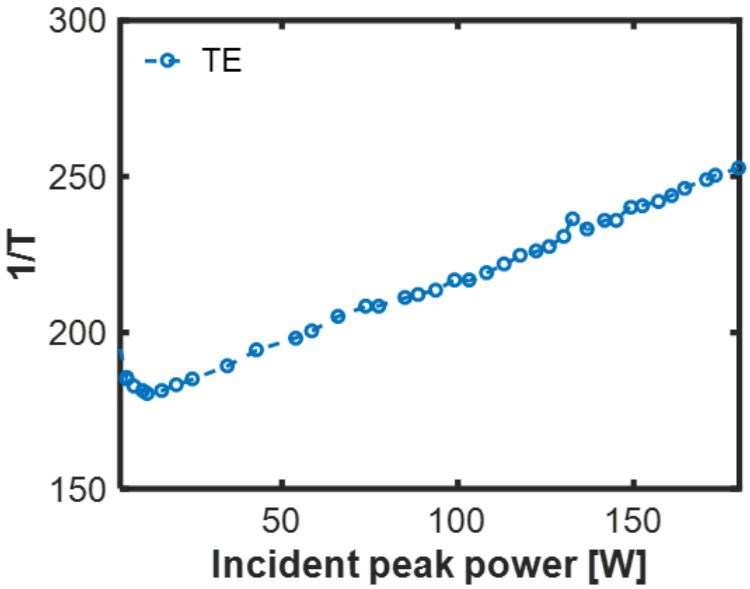

FIGURE 5.25: The inverse transmission as a function of the incident peak power. The TPA coefficient of 19 cm/GW can be calculated through the slope of a line fitted to the experimental data.

is done in a very narrow spectral width covering the idler spectral component. After these adjustments, we started to increase the pump and the signal power gradually to see the maximum FWM effect. Figures 5.26 (a) and (b) show the idler power as a function of the pump power (when the incident signal power was fixed at 215 mW) and as a function of the signal power (when the average incident power was fixed at 17.2 mW), respectively. It is important to note that the lateral pedestals around the signal peaks appear due to amplified spontaneous emission from the EDFA (ASE).

The idler wavelength (λ_i) can be calculated from

$$\frac{1}{\lambda_i} = \frac{2}{\lambda_p} - \frac{1}{\lambda_s}, \tag{5.21}$$

where λ_p and λ_s represent the pump and signal wavelengths, respectively.

In addition, to determine the efficiency of FWM effect as a function of the spectral distance between the signal and the pump wavelengths, we plot the idler power as a function of the spectral difference. Figure 5.27 shows this dependence for the TE and TM polarizations (note that the pump and the signal in the FWM experiments should have the same polarization either both TE or both TM) where the signal wavelength is 1550 nm and the incident pump

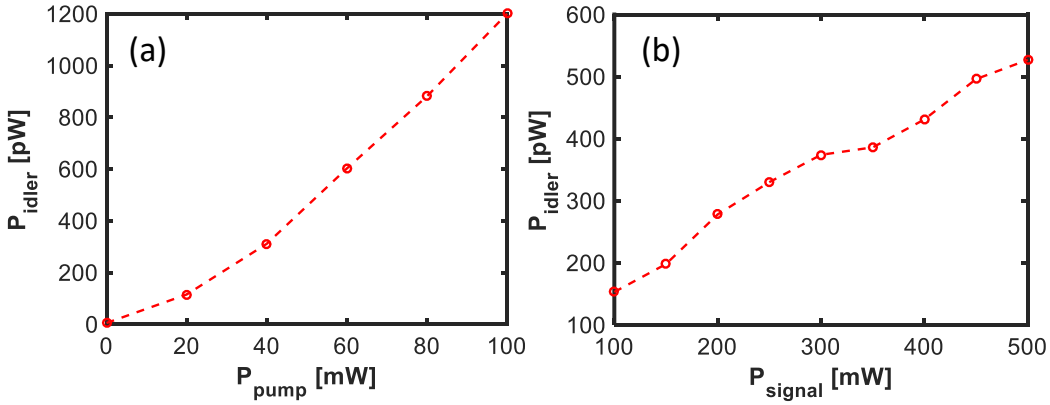

FIGURE 5.26: The idler power as a function of (a) the pump power and (b) the signal power for the half-core waveguide.

and signal powers are 17.2 mW (average power) and 129 mW, respectively. This value of the pump power was chosen such that the detrimental effect of TPA is minimized, and the output power characteristics obey the quadratic law, see Fig. 5.26 and Eq. (4.38). Avoiding the impact of TPA effect when measuring the characteristics shown in Fig. 5.27 allows one to see the pure effect of phase mismatch on the idler power. It can be seen from this figure that the conversion efficiency for TE and TM polarizations drops when the spectral distance between the signal and the pump increases. Figure 5.28 shows the FWM spectra for TE and TM polarizations and the signal wavelength of 1550 nm and the pump and signal powers of 43 mW (average incident power) and 215 mW, respectively.

We repeated FWM experiment for the nanowire waveguides. Figure 5.29 (a) shows the corresponding FWM spectra for the TE and TM polarizations where the signal wavelength is 1550 nm and the average incident pump and signal powers are 4.3 mW and 86 mW, respectively. In Fig. 5.29 (b), we display the generated idler power as a function of the difference between the signal and pump wavelengths. One can see from Fig. 5.29 (b) that, unlike in the case of the half-core waveguides, some side lobes can be observed in addition to the main lobe. It occurs due to the effect of the phase mismatch between the pump, signal, and idler. This phase mismatch results in a sinc-like dependence of the idler power as a function of the spectral distance between the signal and pump, see Eq. (4.39).

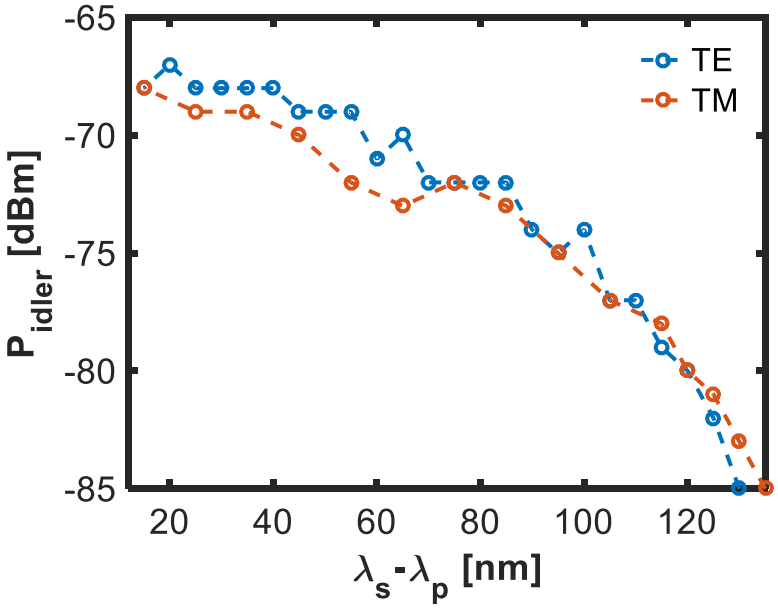

FIGURE 5.27: The idler power as a function of the wavelength difference between the signal and pump for the half-core waveguide for TE and TM polarizations. The signal wavelength is fixed at 1550 nm. The incident pump and signal powers are 17.2 mW (average power) and 129 mW, respectively. The idler power drops as a result of a phase mismatch between the pump, signal and idler as the spectral distance between the pump and signal increases.

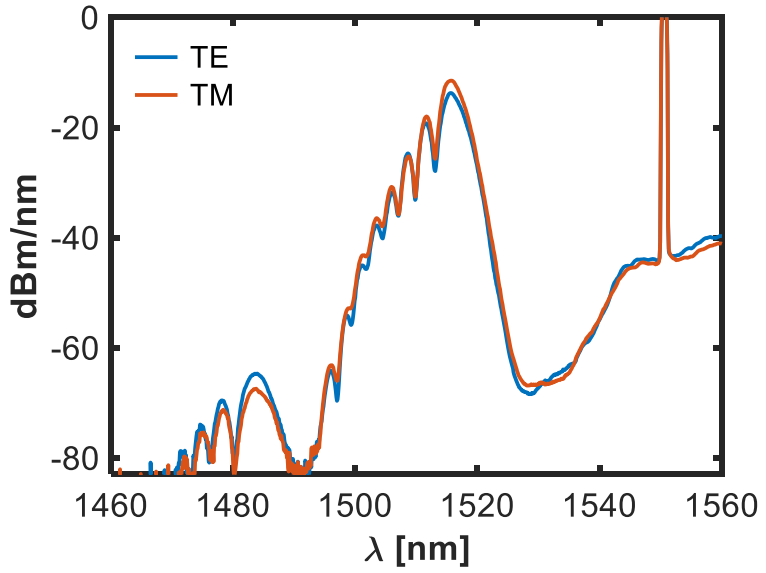

FIGURE 5.28: The FWM spectra for the half-core waveguide for TE and TM polarizations. The incident pump and signal powers are 43 mW (average power) and 215 mW, respectively.

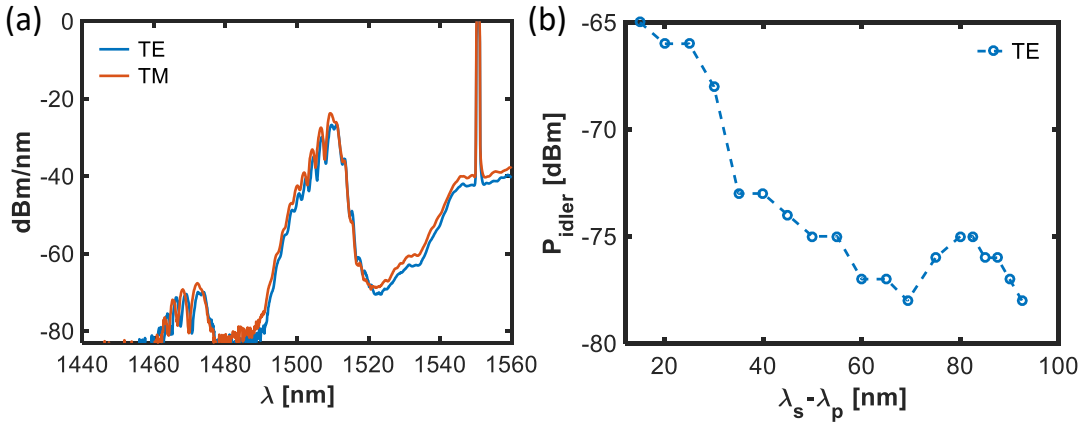

FIGURE 5.29: (a) FWM spectra for the nanowires for TE and TM polarizations. The average incident pump and signal powers are 4.3 mW and 86 mW, respectively (b) The idler power as a function of the wavelength difference between the signal and pump for the nanowire waveguide for the TE and TM polarizations.

5.6.4 Calculation of the conversion efficiency

The conversion efficiency (η) is defined as the ratio of the generated idler power at the output of the waveguide to the signal power at the entrance to the waveguide. It is a key parameter which is used to compare FWM in different devices. It is usually expressed in decibel units as

$$\eta = 10 \log \left(\frac{P^i_{\text{out}}}{P^s_{\text{in}}} \right), \tag{5.22}$$

where P^s_{in} and P^i_{out} represent the signal input power (inside the waveguide) and the idler power at the output of the waveguide, respectively. The conversion efficiency can be obtained either as an average or a peak value. Here, we explain the approach to calculate both those values. The average power $< P >$ from the optical spectrum analyzer (OSA) can be found by integration in the frequency or wavelength domain as

$$< P >= \int_{-\infty}^{\infty} < P(\lambda) > \, \mathrm{d}\lambda. \tag{5.23}$$

The peak power for the signal and idler ($P_{s,i}$) can be obtained as [203]

$$P_{s,i} = \frac{< P_{s,i} >}{\tau f_p}, \tag{5.24}$$

where τ and f_p are the pulse duration and repetition rate of the pump laser, respectively. In our work, we perform the idler power integration based on Eq. (5.23) around the peak wavelength of the idler as

$$\int_{\lambda_{peak}-\delta\lambda}^{\lambda_{peak}+\delta\lambda} < P_i(\lambda) > \, d\lambda, \tag{5.25}$$

where $2\delta\lambda = 1$ nm and the resolution of the OSA is set to 1 nm. The average conversion efficiency can be written as

$$< \eta >= P_i^{dBm} - P_{s_{in}}^{dBm}, \tag{5.26}$$

where $P_i^{dBm} = P_i^{OSA}+$ the OSA coupling loss, which is $\sim$5 dB. On the other hand, the input power for the signal can be calculated as

$$P_{s_{in}}^{dBm} = P_s^{OSA} + \text{OSA coupling loss} - 10\log\left[e^{-\alpha L}(1-R)\right], \tag{5.27}$$

where α, L, and R are known. Finally, the average conversion efficiency of FWM in our experiment can be calculated as

$$< \eta >= P_i^{OSA} - P_s^{OSA} - 4.16 \text{ dB}. \tag{5.28}$$

Regarding the peak conversion efficiency, it can be expressed as

$$P_i^{dBm} = 10\log[< P_i >] - 10\log\left[\tau f_p\right], \tag{5.29}$$

where $\tau = 3$ ps and $f_p = 76.6$ MHz. Therefore, Eq. (5.29) can be expressed as

$$\eta^{peak} =< \eta > +36.4 \text{ dB}. \tag{5.30}$$

For instance, in the case of half-core waveguide, the average and the peak conversion efficiency (for the TE polarization, see Fig. 5.28) are calculated as -69.2 dB and -32.8 dB, respectively, where the incident signal power is 215 mW. Using Eqs. (5.28) and (5.30), one can also calculate the average and the peak conversion efficiencies as functions of the spectral distance, see Fig. 5.30.

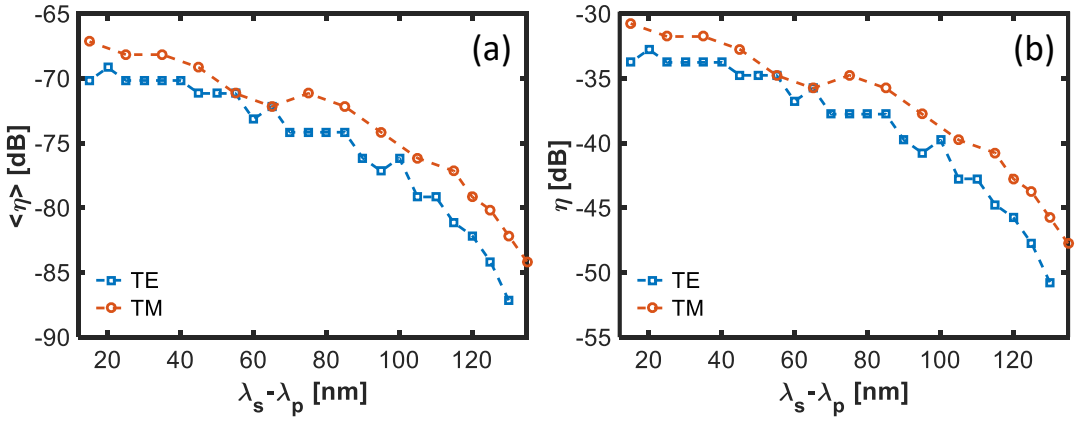

FIGURE 5.30: (a) The average and (b) the peak conversion efficiency as functions of the spectral distance between the signal and the pump for the half-core waveguide.

Based on Fig. 5.27 and Eq. (4.38) from the point where the maximum conversion efficiency occurs (*i.e.* where $\Delta\beta \approx 0$), the nonlinear coefficient (γ) can be obtained as

$$\gamma = \frac{\sqrt{\frac{P_i^{out}}{P_s(e^{-\alpha L})}}}{P_p L_{eff}}. \tag{5.31}$$

Using the parameters extracted from Fig. 5.27, γ can be calculated as 47 which is equivalent to $n_2 = 1.9 \times 10^{-13}$ cm^2/W. These values agree very well with those reported by S. Saeidi *et.al*. [190] ($n_2 \approx 1 \times 10^{-13}$ cm^2/W).

The average conversion efficiency for the nanowire (based on the same approach as we described for the half-core waveguides) can be calculated as

$$< \eta >= P_i^{OSA} - P_s^{OSA} - 13.29 \text{ dB}. \tag{5.32}$$

Using the above equation and Eq. (5.30), the average and the peak conversion efficiencies as functions of spectral distance can be calculated, see Fig. 5.31. From this figure, it can be seen that the average and the peak conversion efficiencies of -74 dB and -37 dB are achievable, respectively, which are lower than the Half-core waveguide. In addition, the nanowire waveguide in comparison with the half-core waveguide exhibits more phase mismatching (see Fig. 5.29 (b)), and the conversion efficiency drops faster as the spectral distance between the signal and the pump changes.

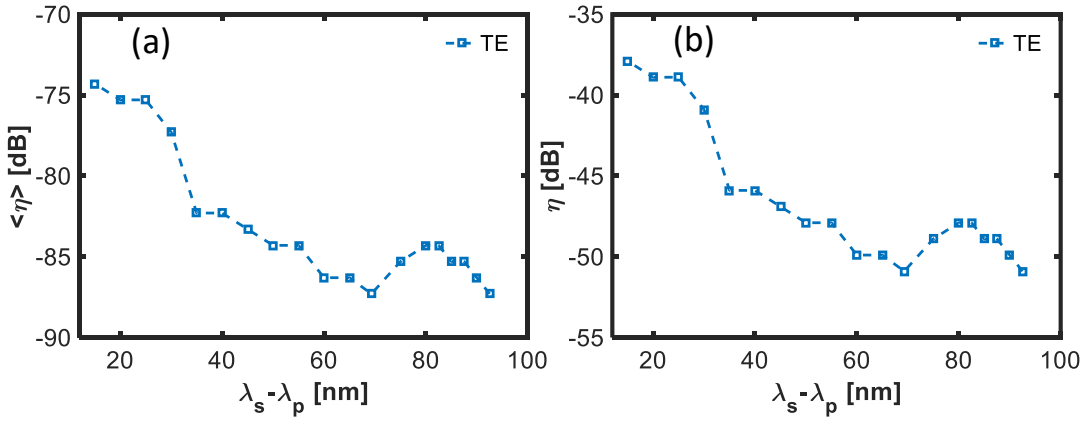

FIGURE 5.31: (a) The average and (b) the peak conversion efficiency as a function of the spectral distance between the signal and pump for the nanowire waveguide. Note that 0 dB level refers to the point where the level of the signal and generated idler are equal.

5.7 Conclusions

In this chapter, we described the results of our nonlinear optical experiments performed in two different InGaAsP/InP waveguide geometries *i.e.* half-core and nanowire waveguides. The original design was targeting zero-GVD by the waveguide geometry, dimensions and composition selection, however, due to fabrication limitations, we employed waveguides with wider widths. The FWM results still represent a valuable contribution. With the composition of $y = 0.7$ and the refractive index contrast of $\Delta n = 0.1$ at the telecom range, we obtained a good light confinement and were able to observe the nonlinear effects. We calculated a nonlinear coefficient of 47 from which the effective nonlinear refractive index of $n_2 = 1.9 \times 10^{-13}$ cm^2/W for InGaAsP has been calculated. This value is in good agreement with an earlier prediction [190]. SPM experiments have been performed in the half-core waveguides. The resulting nonlinear phase shift was measured to be 2π through the SPM effect. This nonlinear phase shift was obtained for the waveguide with the length of $L = 0.2$ cm, which is relatively short. A stronger effect can be observed in a longer waveguide. For the FWM effect, using the half-core (nanowire) waveguide, we obtained the average and the peak conversion efficiencies of -62 dB (-74 dB) and -30 dB (-37 dB), respectively.

Our findings prove that InGaAsP/InP as a suitable material platform for nonlinear photonic devices. In particular, in coherent optical telecommunication, for both transceiver and transmitter parts, nonlinear building blocks are

crucial for optical signal processing and switching. In this regard, $\chi^{(3)}$ processes such as SPM and FWM demonstrated here for InGaAsP waveguides can be quite relevant. That is why developing logic gates made of InGaAsP waveguides based on the FWM process as well as all-optical switches using InGaAsP ring resonators based on the Kerr effect could be potential future work. In an extended context, all the InP devices mentioned here can be integrated with an InP laser on a single chip that in turn can extend the operation wavelength of all-optical circuits. Furthermore, a large second-order nonlinear susceptibility is predicted for InGaAsP (four times larger than GaAs). Due to the importance of $\chi^{(2)}$ effects in quantum optics *e.g.* spontaneous parametric down-conversion (SPDC) process, it would be interesting to measure this coefficient precisely for future work.

Chapter 6

Conclusions

In this thesis, we explored the nonlinear optical potentials of two III-V semiconductor compounds, AlGaAs and InGaAsP, in nonlinear metasurfaces and waveguides, respectively.

In the project related to an AlGaAs metasurface (Chapters 2 and 3 of the thesis), we numerically assessed some linear optical characteristics of a meta-atom made of AlGaAs such as exhibiting Mie resonances, bianisotropy effect, and multipolar decomposition. This part of the study provides a suitable theoretical platform for modelling nonlinear optical response of AlGaAs metasurfaces. Next, we devised an AlGaAs bianisotropic metasurface exhibiting asymmetric second-harmonic generation when illuminated in forward and backward directions. Further, we explored how BICs can enhance the nonlinear optical interactions and the asymmetry effect in such metasurfaces. Numerous studies have been reporting electric and magnetic responses, nonlinear responses (including SHG, THG, and FWM), and the bound states in the continuum (BIC) in high-index metasurfaces. However, none of these studies explored the idea of combining bianisotropy, the BIC concept and nonlinearity. The novelty of our work is that we have combined all these interesting effects to achieve a highly asymmetric nonlinear optical response in an AlGaAs metasurface.

We would like to highlight that our analysis is not reliant on the unique geometry of the bianisotropic meta-atom. The key feature of our work that adds value to the results is the fact that it can be extended to a variety of BIC-based designs of bianisotropic meta-atoms, and our approach to obtaining asymmetric second-harmonic generation is beyond a specific meta-atom geometry. As we claim in Chapter 3 of the thesis, by using BIC, the asymmetric effect can be enhanced by four orders of magnitude compared to that

exhibited by a structure employing only the bianisotropy concept. This is a noteworthy accomplishment of our work.

We believe that this work will motivate several experimental groups to perform an experiment based on our contribution (the idea of combining bianisotropy, nonlinearity, and the BIC concept).

In the InGaAsP project (Chapters 4 and 5), we demonstrated two $\chi^{(3)}$-based effects namely SPM and FWM in the half-core waveguide and FWM in the nanowire waveguide. We reported two initial designs for the strip-loaded and nanowire waveguides exhibiting zero group velocity (for the case of nanowire) and minimum GVD (for the case of strip-loaded). These designs were obtained by selecting a certain composition of phosphorous (*i.e.*, $y = 0.7$) in $In_{1-x}Ga_xAs_{1-y}P_y$ at the Telecom wavelength range. These designs can be helpful for increasing the FWM efficiency in the InGaAsP waveguides. For practical reasons, the fabricated InP waveguides turned out to have a different geometry. Further, the only set of devices that was suitable for optical characterization featured a much wider waveguide width compared to that targeted by the design. Nevertheless, we were able to successfully conduct the linear and nonlinear optical characterization experiments of the waveguides. Furthermore, by performing SPM, FWM, and nonlinear transmission experiments, we were able to retrieve the values of some nonlinear optical coefficients for InGaAsP waveguides with good precision. Specifically, we measured a nonlinear coefficient γ of 47 which is equivalent to the nonlinear refractive index of $n_2 = 1.9 \times 10^{-13}$ cm^2/W, and TPA coefficient of 19 GW/cm. We also observed the SPM effect in the half-core waveguide with the nonlinear phase shift of 2π. This nonlinear phase shift can be increased further for a longer waveguide. The FWM with the average and the peak conversion efficiency of -62 dB (-74 dB) and -30 dB (-37 dB) has been measured in InGaAsP waveguides of half-core and nanowire geometries, respectively. To the best of our knowledge, it is the first report of FWM in the half-core InGaAsP waveguide. The waveguide structures with smaller dimensions and lower propagation loss can be fabricated if an optimum process with a negative-tone resist is implemented.

Measurement of the nonlinear optical coefficient provides important information about nonlinear optical materials. Unfortunately, there is no full information about the dispersion of the nonlinear optical coefficients such as n_2, β_{TPA} available for InGaAsP. Our study represents an isolated measurement at a narrow frequency range. Furthermore, there are no measured

values of the second-order nonlinear optical susceptibility $\chi^{(2)}$ of InGaAsP. Measurement and prediction of the dispersion of the nonlinear optical coefficients of InP-based III-V semiconductor compounds can help one to explore the full potential of this group of materials for nonlinear frequency conversion, for combining passive nonlinear optical devices with light sources on the same chip and for other nonlinear optical applications. InGaAsP/InP as a nonlinear material platform holds great promise for monolithic integration of active and passive devices.

Appendix A

Transformation between the spherical and Cartesian bases

In the Cartesian coordinate, we have a vector $\mathbf{A}$ as

$$\mathbf{A} = a_x \mathbf{e_x} + a_y \mathbf{e_y} + a_z \mathbf{e_z},$$

the above vector can be written in the spherical bases as

$$\mathbf{A}_{spherical} = a_1 \mathbf{e_1} + a_0 \mathbf{e_0} + a_{-1} \mathbf{e_{-1}},$$

where $\mathbf{e_1}$,$\mathbf{e_0}$ and $\mathbf{e_{-1}}$are the spherical bases and

$$\mathbf{e_1} = -\frac{\mathbf{e_x} + i\mathbf{e_y}}{\sqrt{2}},$$

$$\mathbf{e_0} = \mathbf{e_z},$$

$$\mathbf{e_{-1}} = \frac{\mathbf{e_x} - i\mathbf{e_y}}{\sqrt{2}}.$$

These two vectors can be transformed to each other as

$$\begin{bmatrix} a_1 \\ a_0 \\ a_{-1} \end{bmatrix} = \begin{bmatrix} -\frac{1}{\sqrt{2}} & \frac{i}{\sqrt{2}} & 0 \\ 0 & 0 & 1 \\ \frac{1}{\sqrt{2}} & \frac{i}{\sqrt{2}} & 0 \end{bmatrix} \begin{bmatrix} a_x \\ a_y \\ a_z \end{bmatrix}.$$

By the way, the relation between the arbitrary vector $r = \begin{bmatrix} r_1 \\ r_0 \\ r_{-1} \end{bmatrix}$ and the spherical harmonics Y can be obtained as

$$\begin{bmatrix} Y_{11} \\ Y_{10} \\ Y_{1-1} \end{bmatrix} = \frac{1}{2}\sqrt{\frac{3}{\pi}} \begin{bmatrix} -\hat{r}_{-1} \\ \hat{r}_0 \\ -\hat{r}_1 \end{bmatrix},$$

$$\begin{bmatrix} Y_{22} \\ Y_{21} \\ Y_{20} \\ Y_{2-1} \\ Y_{2-2} \end{bmatrix} = \frac{1}{2}\sqrt{\frac{15}{2\pi}} \begin{bmatrix} \hat{r}_{-1}^2 \\ -\sqrt{2}\hat{r}_0\hat{r}_{-1} \\ \sqrt{\frac{2}{3}}\left(\hat{r}_0^2 \hat{r}_{-1}\hat{r}_1\right) \\ -\sqrt{2}\hat{r}_0\hat{r}_1 \\ \hat{r}_1^2 \end{bmatrix},$$

$$\begin{bmatrix} Y_{33} \\ Y_{32} \\ Y_{31} \\ Y_{30} \\ Y_{3-1} \\ Y_{3-2} \\ Y_{3-3} \end{bmatrix} = \frac{1}{2}\sqrt{\frac{35}{2\pi}} \begin{bmatrix} -\hat{r}_{-1}^3 \\ \sqrt{3}\hat{r}_0\hat{r}_{-1}^2 \\ -\sqrt{\frac{3}{5}}\left(2\hat{r}_0^2 + \hat{r}_{-1}\hat{r}_1\right)\hat{r}_{-1} \\ \sqrt{\frac{2}{5}}\left(\hat{r}_0^2 + 3\hat{r}_0\hat{r}_{-1}\right)\hat{r}_0 \\ -\sqrt{\frac{3}{5}}\left(2\hat{r}_0^2 + \hat{r}_{-1}\hat{r}_1\right)\hat{r}_1 \\ \sqrt{3}\hat{r}_0\hat{r}_1^2 \\ -\hat{r}_1^3 \end{bmatrix}.$$

Bibliography

[1] K Al-Hemyari, J. Aitchison, C. Ironside, G. Kennedy, R. Grant, and W Sibbett, "Ultrafast all-optical switching in gaalas integrated interferometer in 1.55 μm spectral region," *Electronics Letters*, vol. 12, no. 28, pp. 1090–1092, 1992.

[2] K Al-hemyari, A Villeneuve, J. Kang, J. Aitchison, C. Ironside, and G. Stegeman, "Ultrafast all-optical switching in gaalas directional couplers at 1.55 μm without multiphoton absorption," *Applied physics letters*, vol. 63, no. 26, pp. 3562–3564, 1993.

[3] A. Locatelli, D. Modotto, D. Paloschi, and C. De Angelis, "All optical switching in ultrashort photonic crystal couplers," *Optics communications*, vol. 237, no. 1-3, pp. 97–102, 2004.

[4] J. Wu, J. Luo, A. K.-Y. Jen, *et al.*, "High-performance organic second- and third-order nonlinear optical materials for ultrafast information processing," *Journal of Materials Chemistry C*, vol. 8, no. 43, pp. 15 009–15 026, 2020.

[5] S. Yoo, C Caneau, R Bhat, M. Koza, A Rajhel, and N. Antoniades, "Wavelength conversion by difference frequency generation in algaas waveguides with periodic domain inversion achieved by wafer bonding," *Applied Physics Letters*, vol. 68, no. 19, pp. 2609–2611, 1996.

[6] W Astar, P. Apiratikul, T. Murphy, and G. Carter, "Wavelength conversion of 10-gb/s rz-ook using filtered xpm in a passive gaas–algaas waveguide," *IEEE Photonics Technology Letters*, vol. 22, no. 9, pp. 637–639, 2010.

[7] L. Caspani, D. Duchesne, K. Dolgaleva, *et al.*, "Optical frequency conversion in integrated devices," *JOSA B*, vol. 28, no. 12, A67–A82, 2011.

[8] M. Ma and L. R. Chen, "Harnessing mode-selective nonlinear optics for on-chip multi-channel all-optical signal processing," *APL Photonics*, vol. 1, no. 8, p. 086 104, 2016.

[9] T. Mahmood, W Astar, B. M. Cannon, *et al.*, "Polarization-insensitive wavelength conversion by FWM of 100-GHz-spaced DWDM 4×10

Gb/s RZ-BPSK signals in a birefringent nonlinear AlGaAs waveguide," *IEEE Journal of Quantum Electronics*, vol. 50, no. 2, pp. 74–84, 2013.

[10] H. Zhang, B. Chang, Z. Li, *et al.*, "Optical frequency combs: From principles to applications," *Journal of Electronic Science and Technology*, p. 100 157, 2022.

[11] V. R. Almeida, C. A. Barrios, R. R. Panepucci, and M. Lipson, "All-optical control of light on a silicon chip," *Nature*, vol. 431, no. 7012, pp. 1081–1084, 2004.

[12] V. G. Ta'eed, M. Shokooh-Saremi, L. Fu, *et al.*, "Integrated all-optical pulse regenerator in chalcogenide waveguides," *Optics Letters*, vol. 30, no. 21, pp. 2900–2902, 2005.

[13] V. G. Ta'eed, M. Shokooh-Saremi, L. Fu, *et al.*, "Self-phase modulation-based integrated optical regeneration in chalcogenide waveguides," *IEEE Journal of Selected Topics in Quantum Electronics*, vol. 12, no. 3, pp. 360–370, 2006.

[14] I. S. Grudinin, N. Yu, and L. Maleki, "Generation of optical frequency combs with a caf$_2$ resonator," *Optics letters*, vol. 34, no. 7, pp. 878–880, 2009.

[15] W Liang, A. Savchenkov, A. Matsko, V. Ilchenko, D Seidel, and L Maleki, "Generation of near-infrared frequency combs from a MgF_2 whispering gallery mode resonator," *Optics letters*, vol. 36, no. 12, 2011.

[16] L. Chang, W. Xie, H. Shu, *et al.*, "Ultra-efficient frequency comb generation in algaas-on-insulator microresonators," *Nature communications*, vol. 11, no. 1, pp. 1–8, 2020.

[17] D. R. Smith, W. J. Padilla, D. Vier, S. C. Nemat-Nasser, and S. Schultz, "Composite medium with simultaneously negative permeability and permittivity," *Physical review letters*, vol. 84, no. 18, p. 4184, 2000.

[18] R. A. Shelby, D. Smith, S. Nemat-Nasser, and S. Schultz, "Microwave transmission through a two-dimensional, isotropic, left-handed metamaterial," *Applied Physics Letters*, vol. 78, no. 4, pp. 489–491, 2001.

[19] D. R. Smith, J. B. Pendry, and M. C. Wiltshire, "Metamaterials and negative refractive index," *Science*, vol. 305, no. 5685, pp. 788–792, 2004.

[20] D. Schurig, J. J. Mock, B. Justice, *et al.*, "Metamaterial electromagnetic cloak at microwave frequencies," *Science*, vol. 314, no. 5801, pp. 977–980, 2006.

[21] R. Fleury, F. Monticone, and A. Alù, "Invisibility and cloaking: Origins, present, and future perspectives," *Physical Review Applied*, vol. 4, no. 3, p. 037 001, 2015.

[22] B. Zhang, "Electrodynamics of transformation-based invisibility cloaking," *Light: Science & Applications*, vol. 1, no. 10, e32–e32, 2012.

[23] D. Smith and D Schurig, "Electromagnetic wave propagation in media with indefinite permittivity and permeability tensors," *Physical Review Letters*, vol. 90, no. 7, p. 077 405, 2003.

[24] A. Poddubny, I. Iorsh, P. Belov, and Y. Kivshar, "Hyperbolic metamaterials," *Nature photonics*, vol. 7, no. 12, pp. 948–957, 2013.

[25] M. Jang, Y. Horie, A. Shibukawa, *et al.*, "Wavefront shaping with disorder-engineered metasurfaces," *Nature photonics*, vol. 12, no. 2, pp. 84–90, 2018.

[26] A. C. Overvig, S. Shrestha, S. C. Malek, *et al.*, "Dielectric metasurfaces for complete and independent control of the optical amplitude and phase," *Light: Science & Applications*, vol. 8, no. 1, pp. 1–12, 2019.

[27] A. M. Shaltout, V. M. Shalaev, and M. L. Brongersma, "Spatiotemporal light control with active metasurfaces," *Science*, vol. 364, no. 6441, eaat3100, 2019.

[28] P. Berini, "Optical beam steering using tunable metasurfaces," *ACS Photonics*, 2022.

[29] P. C. Wu, R. Sokhoyan, G. K. Shirmanesh, W.-H. Cheng, and H. A. Atwater, "Near-infrared active metasurface for dynamic polarization conversion," *Advanced Optical Materials*, vol. 9, no. 16, p. 2 100 230, 2021.

[30] P. Yu, J. Li, and N. Liu, "Electrically tunable optical metasurfaces for dynamic polarization conversion," *Nano Letters*, vol. 21, no. 15, 6690–6695, 2021.

[31] I. Staude, A. E. Miroshnichenko, M. Decker, *et al.*, "Tailoring directional scattering through magnetic and electric resonances in subwavelength silicon nanodisks," *ACS nano*, vol. 7, no. 9, pp. 7824–7832, 2013.

[32] W. Liu and Y. S. Kivshar, "Generalized kerker effects in nanophotonics and meta-optics," *Optics express*, vol. 26, no. 10, pp. 13 085–13 105, 2018.

[33] S. A. Maier *et al.*, *Plasmonics: fundamentals and applications*. Springer, 2007, vol. 1.

[34] V. G. Kravets, A. V. Kabashin, W. L. Barnes, and A. N. Grigorenko, "Plasmonic surface lattice resonances: A review of properties and applications," *Chemical reviews*, vol. 118, no. 12, pp. 5912–5951, 2018.

[35] M. S. Bin-Alam, O. Reshef, Y. Mamchur, *et al.*, "Ultra-high-q resonances in plasmonic metasurfaces," *Nature communications*, vol. 12, no. 1, pp. 1–8, 2021.

[36] M. F. Limonov, M. V. Rybin, A. N. Poddubny, and Y. S. Kivshar, "Fano resonances in photonics," *Nature Photonics*, vol. 11, no. 9, pp. 543–554, 2017.

[37] Z. Liu and J. Ye, "Highly controllable double fano resonances in plasmonic metasurfaces," *Nanoscale*, vol. 8, no. 40, pp. 17 665–17 674, 2016.

[38] A. I. Kuznetsov, A. E. Miroshnichenko, M. L. Brongersma, Y. S. Kivshar, and B. Luk'yanchuk, "Optically resonant dielectric nanostructures," *Science*, vol. 354, no. 6314, aag2472, 2016.

[39] S. Kruk and Y. Kivshar, "Functional meta-optics and nanophotonics governed by mie resonances," *Acs Photonics*, vol. 4, no. 11, pp. 2638–2649, 2017.

[40] A. E. Miroshnichenko and Y. S. Kivshar, "Fano resonances in all-dielectric oligomers," *Nano letters*, vol. 12, no. 12, pp. 6459–6463, 2012.

[41] C. Wu, N. Arju, G. Kelp, *et al.*, "Spectrally selective chiral silicon metasurfaces based on infrared fano resonances," *Nature communications*, vol. 5, no. 1, pp. 1–9, 2014.

[42] C. W. Hsu, B. Zhen, A. D. Stone, J. D. Joannopoulos, and M. Soljačić, "Bound states in the continuum," *Nature Reviews Materials*, vol. 1, no. 9, pp. 1–13, 2016.

[43] I. S. Sinev, K. Koshelev, Z. Liu, *et al.*, "Observation of ultrafast self-action effects in quasi-bic resonant metasurfaces," *Nano Letters*, vol. 21, no. 20, pp. 8848–8855, 2021.

[44] L. Carletti, K. Koshelev, C. De Angelis, and Y. Kivshar, "Giant nonlinear response at the nanoscale driven by bound states in the continuum," *Physical review letters*, vol. 121, no. 3, p. 033 903, 2018.

[45] Z. Liu, Y. Xu, Y. Lin, *et al.*, "High-q quasibound states in the continuum for nonlinear metasurfaces," *Physical review letters*, vol. 123, no. 25, p. 253 901, 2019.

[46] A. P. Anthur, H. Zhang, R. Paniagua-Dominguez, *et al.*, "Continuous wave second harmonic generation enabled by quasi-bound-states in the continuum on gallium phosphide metasurfaces," *Nano Letters*, vol. 20, no. 12, pp. 8745–8751, 2020.

[47] L. Carletti, S. S. Kruk, A. A. Bogdanov, C. De Angelis, and Y. Kivshar, "High-harmonic generation at the nanoscale boosted by bound states in the continuum," *Physical Review Research*, vol. 1, no. 2, p. 023 016, 2019.

[48] A. Krasnok, M. Tymchenko, and A. Alù, "Nonlinear metasurfaces: A paradigm shift in nonlinear optics," *Materials Today*, vol. 21, no. 1, pp. 8–21, 2018.

[49] M. Pu, H. Hu, L. Ottaviano, *et al.*, "Ultra-efficient and broadband nonlinear algaas-on-insulator chip for low-power optical signal processing," *Laser & Photonics Reviews*, vol. 12, no. 12, p. 1 800 111, 2018.

[50] B. E. Saleh and M. C. Teich, *Fundamentals of photonics*. john Wiley & sons, 2019.

[51] J Meier, W. Mohammed, A Jugessur, L Qian, M Mojahedi, and J. Aitchison, "Group velocity inversion in algaas nanowires," *Optics express*, vol. 15, no. 20, pp. 12 755–12 762, 2007.

[52] D. H. Espinosa, S. R. Harrigan, K. M. Awan, P. Rasekh, and K. Dolgaleva, "Geometry-dependent two-photon absorption followed by free-carrier absorption in algaas waveguides," *JOSA B*, vol. 38, no. 12, pp. 3765–3774, 2021.

[53] D. Anderson and J. Boyd, "Wideband co_2 laser second harmonic generation phase matched in gaas thin-film waveguides," *Applied Physics Letters*, vol. 19, no. 8, pp. 266–268, 1971.

[54] J. P. Van Der Ziel, R. C. Miller, R. A. Logan, W. A. Nordland, and R. M. Mikulyak, "Phase-matched second-harmonic generation in GaAs optical waveguides by focused laser beams," *Applied Physics Letters*, vol. 25, no. 4, p. 238, 1974. DOI: 10.1063/1.1655455.

[55] J. P. Van Der Ziel, M. Ilegems, P. W. Foy, and R. M. Mikulyak, "Phase-matched second harmonic generation in a periodic GaAs waveguide," *Applied Physics Letters*, vol. 29, no. 12, p. 775, 1976. DOI: 10.1063/1.88945.

[56] D. Vakhshoori, J. Walker, S. Wang, J. S. Smith, C. E. Soccolich, and M. N. Islam, "Integrable optical correlator: Its temporal resolution, spectral response, and power sensitivity," *Applied Physics Letters*, vol. 54, no. 18, p. 1725, 1989. DOI: 10.1063/1.101374.

[57] H. Q. Le, D. E. Bossi, K. B. Nichols, and W. D. Goodhue, "Observation of Maker fringes and estimation of $\chi^{(3)}$ using picosecond nondegenerate four-wave mixing in AlGaAs waveguides," *Applied Physics Letters*, vol. 56, no. 11, pp. 1008–1010, 1990. DOI: 10.1063/1.102600.

[58] M. Islam, C. Soccolich, R. Slusher, A. Levi, W. Hobson, and M. Young, "Nonlinear spectroscopy near half-gap in bulk and quantum well gaas /algaas waveguides," *Journal of Applied Physics*, vol. 71, no. 4, pp. 1927–1935, 1992.

[59] H. Q. Le and S. D. Cecca, "Ultrafast, multi-THz-detuning, third-order frequency conversion in semiconductor quantum-well waveguides," *IEEE Photonics Technology Letters*, vol. 4, no. 8, pp. 878–880, 1992.

[60] K. Al-Hemyari, J. Aitchison, C. Ironside, G. Kennedy, R. Grant, and W. Sibbett, "Ultrafast all-optical switching in GaAlAs integrated interferometer in 1.55 μm spectral region," *Electronics Letters*, vol. 28, no. 12, p. 1090, 1992. DOI: 10.1049/EL:19920689.

[61] A. Villeneuve, C. C. Yang, P. G. Wigley, *et al.*, "Ultrafast all-optical switching in semiconductor nonlinear directional couplers at half the band gap," *Applied Physics Letters*, vol. 61, no. 2, pp. 147–149, 1992. DOI: 10.1063/1.108200.

[62] A. Villeneuve, C. C. Yang, G. I. Stegeman, C. H. Lin, and H. H. Lin, "Nonlinear refractive-index and two photon-absorption near half the band gap in AlGaAs," *Applied Physics Letters*, vol. 62, no. 20, p. 2465, 1993. DOI: 10.1063/1.109320.

[63] K. Al-Hemyari, A. Villeneuve, J. U. Kang, J. S. Aitchison, C. N. Ironside, and G. I. Stegeman, "Ultrafast all-optical switching in GaAlAs directional couplers at 1.55 μm without multiphoton absorption," *Applied Physics Letters*, vol. 63, no. 26, p. 3562, 1993. DOI: 10.1063/1.110097.

[64] J. S. Aitchison, A. Villeneuve, and G. I. Stegeman, "All optical switching in a nonlinear GaAlAs X-junction," *Optics Letters*, vol. 18, no. 14, pp. 1153–1155, 1993. DOI: 10.1364/OL.18.001153.

[65] C. C. Yang, A. Villeneuve, G. I. Stegeman, C.-H. Lin, H.-H. Lin, and I.-P. Chiou, "Nonlinear polarization switching near half the band gap in semiconductors," *Optics Letters*, vol. 18, no. 18, pp. 1487–1489, 1993. DOI: 10.1364/OL.18.001487.

[66] J. U. Kang, A. Villeneuve, M. Sheik-Bahae, *et al.*, "Limitation due to three-photon absorptionon the useful spectral range for nonlinearoptics in AlGaAs below half band gap," *Applied Physics Letters*, vol. 65, no. 2, pp. 147–149, 1994.

[67] G. Stegeman, A Villeneuve, J Kang, *et al.*, "AlGaAs below half bandgap: The silicon of nonlinear optical materials," *International Journal of Nonlinear Optical Physics*, vol. 3, no. 03, pp. 347–371, 1994.

[68] A Villeneuve, C. C. Yang, G. I. Stegeman, C. N. Ironside, G Scelsi, and R. M. Osgood, "Nonlinear absorption in a GaAs waveguide just above half the band gap," *IEEE Journal of Quantum Electronics*, vol. 30, no. 5, pp. 1172–1175, 1994.

[69] S. Yoo, R Bhat, C Caneau, and M. Koza, "Quasi-phase-matched second-harmonic generation in algaas waveguides with periodic domain inversion achieved by wafer-bonding," *Applied Physics Letters*, vol. 66, no. 25, pp. 3410–3412, 1995.

[70] J. U. Kang, G. I. Stegeman, J. S. Aitchison, and J. S. Aitchison, "All-optical multiplexing of femtosecond signals by using an AlGaAs nonlinear directional coupler," *Conference on Lasers and Electro-Optics (199 5), paper CThB3*, CThB3, 1995.

[71] A. Villeneuve, J. U. Kang, J. S. Aitchison, and G. I. Stegeman, "Unity ratio of cross- to self-phase modulation in bulk AlGaAs and AlGaAs/GaAs multiple quantum well waveguides at half the band gap," *Applied Physics Letters*, vol. 67, no. 1995, p. 760, 1995. DOI: 10.1063/1.115217.

[72] A. Villeneuve, P. Mamyshev, J. U. Kang, G. I. Stegeman, J. S. Aitchison, and C. N. Ironside, "Efficient time-domain demultiplexing with separate signal and control wavelengths in an AlGaAs nonlinear directional coupler," *IEEE Journal of Quantum Electronics*, vol. 31, no. 12, pp. 2165–2172, 1995. DOI: 10.1109/3.477742.

[73] A. Villeneuve, P. Mamyshev, J. U. Kang, G. I. Stegeman, J. S. Aitchison, and C. N. Ironside, "Time domain all-optical demultiplexing with a semiconductor directional coupler," *Applied Physics Letters*, vol. 66, no. 13, p. 1668, 1995. DOI: 10.1063/1.113887.

[74] R. P. Espindola, M. K. Udo, and S. T. Ho, "Nearly-degenerate frequency technique for simultaneous measurement of $n^{(2)}$ and $\alpha^{(2)}$, and four-wave mixing gain coefficients in waveguides," *Optics Communications*, vol. 119, pp. 682–692, 1995.

[75] D. C. Hutchings, J. S. Aitchison, A. Villeneuve, *et al.*, "Polarization dependence of ultrafast nonlinear refraction in semiconductors at the half-bandgap," *Optics and Photonics News*, vol. 6, no. 12, p. 28, 1995.

[76] P. A. Ramos and E. Towe, "Second-harmonic generation of blue light from [112]-oriented III-V antiresonant waveguide heterostructures," *Applied Physics Letters*, vol. 68, no. 13, p. 1754, 1996. DOI: 10.1063/1.116656.

[77] J. U. Kang, G. I. Stegeman, A. Villeneuve, and J. S. Aitchison, "AlGaAs below half bandgap: A laboratory for spatial soliton physics," *Pure and Applied Optics (Print edition) (United Kingdom)*, vol. 5, no. 5, pp. 583–594, 1996. DOI: 10.1088/0963-9659/5/5/012.

[78] C. J. Hamilton, J. H. Marsh, D. C. Hutchings, J. S. Aitchison, G. T. Kennedy, and W. Sibbett, "Localized Kerr-type nonlinearities in GaAs /AlGaAs multiple quantum well structures at 1.55 μm," *Applied Physics Letters*, vol. 68, no. 22, pp. 3078–3080, 1996.

[79] J. S. Aitchison, D. Hutchings, J. Kang, G. Stegeman, and A. Villeneuve, "The nonlinear optical properties of algaas at the half band gap," *IEEE journal of quantum electronics*, vol. 33, no. 3, pp. 341–348, 1997.

[80] A. Fiore, Y. Beaulieu, S. Janz, J. P. McCaffrey, Z. R. Wasilewski, and D. X. Xu, "Quasiphase matched surface emitting second harmonic generation in periodically reversed asymmetric GaAs/AlGaAs quantum well waveguide," *Applied Physics Letters*, vol. 70, no. 20, p. 2655, 1997. DOI: 10.1063/1.118987.

[81] A. Fiore, V. Berger, E. Rosencher, P. Bravetti, N. Laurent, and J. Nagle, "Phase-matched mid-infrared difference frequency generation in GaAs-based waveguides," *Applied Physics Letters*, vol. 71, no. 25, 3622 , 1997. DOI: 10.1063/1.120460.

[82] M. W. Street, N. D. Whitbread, C. J. Hamilton, *et al.*, "Modification of the second-order optical nonlinearities in AlGaAs asymmetric multiple quantum well waveguides by quantum well intermixing," *Applied Physics Letters*, vol. 70, no. 21, p. 2804, 1997. DOI: 10.1063/1.119064.

[83] M. W. Street, N. D. Whitbread, D. C. Hutchings, *et al.*, "Quantum-well intermixing for the control of second-order nonlinear effects in AlGaAs multiple-quantum-well waveguides," *Optics Letters*, vol. 22, no. 21, pp. 1600–1602, 1997. DOI: 10.1364/OL.22.001600.

[84] C. Q. Xu, K. Takemasa, K. Nakamura, K. Shinozaki, H. Okayama, and T. Kamijoh, "Device length dependence of optical second-harmonic generation in AlGaAs quasiphase matched waveguides," *Applied Physics Letters*, vol. 70, no. 12, p. 1554, 1997. DOI: 10.1063/1.118636.

[85] A. Fiore, S. Janz, L. Delobel, *et al.*, "Second-harmonic generation at λ=1.6 μm in AlGaAs/Al_2O_3 waveguides using birefringence phase matching," *Applied Physics Letters*, vol. 72, no. 23, p. 2942, 1998. DOI: 10.1063/1.121501.

[86] P. Bravetti, A. Fiore, V. Berger, E. Rosencher, J. Nagle, and O. Gauthier-Lafaye, "5.2–5.6-μm source tunable by frequency conversion in a GaAs-based waveguide," *Optics Letters*, vol. 23, no. 5, pp. 331–333, 1998. DOI: 10.1364/OL.23.000331.

[87] C. Q. Xu, K. Takemasa, K. Nakamura, H. Okayama, and T. Kamihoh, "AlGaAs semiconductor quasiphase-matched wavelength converters," *Japanese Journal of Applied Physics*, vol. 37, no. 3 A, pp. 823–831, 1998. DOI: 10.1143/JJAP.37.823/XML.

[88] J. U. Kang, J. S. Aitchison, G. I. Stegeman, and N. Akhmediev, "One-dimensional spatial solitons in AlGaAs waveguides," *Optical and Quantum Electronics*, vol. 30, no. 7, pp. 649–672, 1998. DOI: 10.1023/A:1006935801045.

[89] A. Fiore, V. Berger, E. Rosencher, P. Bravetti, and J. Nagle, "Phase matching using an isotropic nonlinear optical material," *Nature*, vol. 39 1, pp. 463–466, 1998. DOI: 10.1038/35091.

[90] P. Millar, R. M. De La Rue, T. F. Krauss, J. S. Aitchison, N. G. R. Broderick, and D. J. Richardson, "Nonlinear propagation effects in an AlGaAs Bragg grating filter," *Optics Letters*, vol. 24, no. 10, pp. 685–687, 1999. DOI: 10.1364/OL.24.000685.

[91] U. Peschel, R. Morandotti, J. S. Aitchison, H. S. Eisenberg, and Y. Silberberg, "Nonlinearly induced escape from a defect state in waveguide arrays," *Applied Physics Letters*, vol. 75, no. 10, pp. 1348–1350, 1999.

[92] K. Dolgaleva, W. C. Ng, L. Qian, and J. S. Aitchison, "Compact highly-nonlinear algaas waveguides for efficient wavelength conversion," *Optics express*, vol. 19, no. 13, pp. 12 440–12 455, 2011.

[93] K. Dolgaleva, P. Sarrafi, P. Kultavewuti, *et al.*, "Tuneable four-wave mixing in algaas nanowires," *Optics express*, vol. 23, no. 17, pp. 22 477–22 493, 2015.

[94] E. Mobini, D. H. Espinosa, K. Vyas, and K. Dolgaleva, "Algaas nonlinear integrated photonics," *Micromachines*, vol. 13, no. 7, p. 991, 2022.

[95] K. Nakatsuhara, R. Muzimoto, R. Munakata, Y. Kigure, and Y. Naito, "All-optical set-reset operation in a distributed feedback GaInAsP waveguide," *IEEE Photonics Technology Letters*, vol. 10, no. 1, pp. 78–80, 1998.

[96] I. E. Day, P. A. Snow, R. V. Pentry, *et al.*, "Bias dependent recovery time of all-optical resonant nonlinearity in an InGaAsP/InGaAsP multi-quantum well waveguide," *Applied Physics Letters*, vol. 65, no. 1, 2657 –2659, 1994. DOI: 10.1063/1.112594.

[97] A. D'Ottavi, A. Mecozzi, S. Scotti, *et al.*, "Four-wave mixing efficiency in traveling wave semiconductor optical amplifiers at high saturation," *Applied Physics Letters*, vol. 67, no. July 1995, p. 2753, 1995. DOI: 10.1063/1.114582.

[98] J. P. Donnelly, H. Q. Le, E. A. Swanson, S. H. Groves, A. Darwish, and E. P. Ippen, "Nondegenerate four-wave mixing wavelength conversion in low-loss passive InGaAsP–InP quantum-well waveguides," *IEEE Photonics Technology Letters*, vol. 8, no. 5, pp. 623–625, 1996.

[99] A. M. Darwish, E. P. Ippen, H. Q. Le, J. P. Donnelly, S. H. Groves, and E. A. Swanson, "Short-pulse wavelength shifting by four wave mixing in passive InGaAsP/InP waveguides," *Applied Physics Letters*, vol. 68, no. 15, pp. 2038–2040, 1996.

[100] H. K. Tsang, R. V. Pentry, I. H. White, *et al.*, "Two-photon absorption and self-phase modulation in InGaAsP/InP multiquantum-well waveguides," *Journal of Applied Physics*, vol. 70, no. 7, pp. 3992–3994, 1991. DOI: 10.1063/1.349168.

[101] S. Saeidi, P. Rasekh, K. M. Awan, A. Tüğen, M. J. Huttunen, and K. Dolgaleva, "Demonstration of optical nonlinearity in InGaAsP/InP passive waveguides," *Optical Materials*, vol. 84, p. 524, 2018.

[102] P. York, K. Beernink, G. Fernandez, and J. Coleman, "Ingaas-gaas strained-layer quantum well buried heterostructure lasers (λ> 1 μm) by metalorganic chemical vapor deposition," *Applied physics letters*, vol. 5 4, no. 6, pp. 499–501, 1989.

[103] K.-Y. Liou, A. Dentai, E. Burrows, C. Joyner, C. Burrus, and G Raybon, "Strained-layer single quantum-well ingaasp/inp lasers for wavelength range from 1.43 μm to 1.55 μm," in *Conference on Lasers and Electro-Optics*, Optica Publishing Group, 1991, CFD4.

[104] F. Xiong, T. Tombrello, H Wang, *et al.*, "Fabrication of gaas/algaas quantum well lasers with mev oxygen ion implantation," *MRS Online Proceedings Library*, vol. 144, no. 1, pp. 367–372, 1988.

[105] D. Saxena, N. Jiang, X. Yuan, *et al.*, "Design and room-temperature operation of gaas/algaas multiple quantum well nanowire lasers," *Nano letters*, vol. 16, no. 8, pp. 5080–5086, 2016.

[106] S. Adachi, *Properties of semiconductor alloys: group-IV, III-V and II-VI semiconductors*. John Wiley & Sons, 2009.

[107] T. M. Quist, R. H. Rediker, R. Keyes, *et al.*, "Semiconductor maser of gaas," *Applied Physics Letters*, vol. 1, no. 4, pp. 91–92, 1962.

[108] G. Roelkens, A. Abassi, P. Cardile, *et al.*, "Iii-v-on-silicon photonic devices for optical communication and sensing," in *Photonics*, MDPI, vol. 2, 2015, pp. 969–1004.

[109] B. Jalali, "Nonlinear optics in the mid-infrared," *Nature Photonics*, vol. 4, no. 8, pp. 506–508, 2010.

[110] K. Vyas, D. H. Espinosa, D. Hutama, *et al.*, "Group iii-v semiconductors as promising nonlinear integrated photonic platforms," *Advances in Physics: X*, vol. 7, no. 1, p. 2 097 020, 2022.

[111] J. Donnelly, H. Le, E. Swanson, S. Groves, A Darwish, and E. Ippen, "Nondegenerate four-wave mixing wavelength conversion in low-loss passive ingaasp-inp quantum-well waveguides," *IEEE Photonics Technology Letters*, vol. 8, no. 5, pp. 623–625, 1996.

[112] E. Mobini, R. Alaee, R. W. Boyd, and K. Dolgaleva, "Giant asymmetric second-harmonic generation in bianisotropic metasurfaces based on bound states in the continuum," *ACS Photonics*, vol. 8, no. 11, pp. 3234–3240, 2021.

[113] S Gehrsitz, F. Reinhart, C Gourgon, N Herres, A Vonlanthen, and H Sigg, "The refractive index of al x ga 1- x as below the band gap: Accurate determination and empirical modeling," *Journal of Applied Physics*, vol. 87, no. 11, pp. 7825–7837, 2000.

[114] M Savanier, A Andronico, A Lemaître, *et al.*, "Large second-harmonic generation at 1.55 μmin oxidized algaas waveguides," *Optics letters*, vol. 36, no. 15, pp. 2955–2957, 2011.

[115] S. Adachi, *GaAs and related materials: bulk semiconducting and superlattice properties*. World Scientific, 1994.

[116] M Ohashi, T Kondo, R Ito, *et al.*, "Determination of quadratic nonlinear optical coefficient of al x ga1- x as system by the method of reflected second harmonics," *Journal of applied physics*, vol. 74, no. 1, pp. 596–601, 1993.

[117] I. Shoji, T. Kondo, A. Kitamoto, M. Shirane, and R. Ito, "Absolute scale of second-order nonlinear-optical coefficients," *JOSA B*, vol. 14, no. 9, pp. 2268–2294, 1997.

[118] J. Aitchison, D. Hutchings, J. Kang, G. Stegeman, and A. Villeneuve, "The nonlinear optical properties of AlGaAs at the half band gap,"

IEEE Journal of Quantum Electronics, vol. 33, no. 3, pp. 341–348, 1997, ISSN: 00189197. DOI: 10.1109/3.556002. [Online]. Available: http://ieeexplore.ieee.org/document/556002/.

[119] M. S. Shur, *Handbook Series on Semiconductor Parameters, Vol. 2: Ternary and Quaternary III-V Compounds*. World Scientific, 1996.

[120] M Cada, M Svilans, S Janz, R Bierman, R Normandin, and J Glinski, "Second harmonic generation in ingaasp waveguides at 1.3 μm wavelength," *Applied physics letters*, vol. 61, no. 17, pp. 2090–2092, 1992.

[121] O. J. Glembocki and H. Piller, *Handbook of Optical Constants in Solids*. Academic Press, 1985.

[122] A. Yariv and P. Yeh, *Photonics: optical electronics in modern communications*. Oxford university press, 2007.

[123] G. Marino, C. Gigli, D. Rocco, *et al.*, "Zero-order second harmonic generation from algaas-on-insulator metasurfaces," *ACS photonics*, vol. 6, no. 5, pp. 1226–1231, 2019.

[124] G. Marino, A. S. Solntsev, L. Xu, *et al.*, "Sum-frequency-and photon-pair-generation in algaas nano-disks," in *Nonlinear Photonics*, Optical Society of America, 2018, NpM2I–2.

[125] L. Carletti, G. Marino, L. Ghirardini, *et al.*, "Nonlinear goniometry by second-harmonic generation in algaas nanoantennas," *ACS photonics*, vol. 5, no. 11, pp. 4386–4392, 2018.

[126] D. Rocco, M. A. Vincenti, and C. De Angelis, "Boosting second harmonic radiation from algaas nanoantennas with epsilon-near-zero materials," *Applied Sciences*, vol. 8, no. 11, p. 2212, 2018.

[127] L. Xu, M. Rahmani, D. Smirnova, *et al.*, "Highly-efficient longitudinal second-harmonic generation from doubly-resonant algaas nanoantennas," in *Photonics*, MDPI, vol. 5, 2018, p. 29.

[128] V. F. Gili, L. Carletti, A Locatelli, *et al.*, "Monolithic algaas second-harmonic nanoantennas," *Optics Express*, vol. 24, no. 14, pp. 15 965–15 971, 2016.

[129] D. Rocco, C. Gigli, L. Carletti, *et al.*, "Vertical second harmonic generation in asymmetric dielectric nanoantennas," *IEEE Photonics Journal*, vol. 12, no. 3, pp. 1–7, 2020.

[130] S. S. Kruk, R. Camacho-Morales, L. Xu, *et al.*, "Nonlinear optical magnetism revealed by second-harmonic generation in nanoantennas," *Nano letters*, vol. 17, no. 6, pp. 3914–3918, 2017.

[131] A. B. Evlyukhin, S. M. Novikov, U. Zywietz, *et al.*, "Demonstration of magnetic dipole resonances of dielectric nanospheres in the visible region," *Nano letters*, vol. 12, no. 7, pp. 3749–3755, 2012.

[132] S. Liu, M. B. Sinclair, S. Saravi, *et al.*, "Resonantly enhanced second-harmonic generation using iii–v semiconductor all-dielectric metasurfaces," *Nano letters*, vol. 16, no. 9, pp. 5426–5432, 2016.

[133] R. Camacho-Morales, M. Rahmani, S. Kruk, *et al.*, "Nonlinear generation of vector beams from algaas nanoantennas," *Nano letters*, vol. 16, no. 11, pp. 7191–7197, 2016.

[134] S. V. Makarov, M. I. Petrov, U. Zywietz, *et al.*, "Efficient second-harmonic generation in nanocrystalline silicon nanoparticles," *Nano letters*, vol. 17, no. 5, pp. 3047–3053, 2017.

[135] C. Gigli, G. Marino, A. Artioli, *et al.*, "Tensorial phase control in nonlinear meta-optics," *Optica*, vol. 8, no. 2, pp. 269–276, 2021.

[136] M. R. Shcherbakov, D. N. Neshev, B. Hopkins, *et al.*, "Enhanced third-harmonic generation in silicon nanoparticles driven by magnetic response," *Nano letters*, vol. 14, no. 11, pp. 6488–6492, 2014.

[137] A. S. Shorokhov, E. V. Melik-Gaykazyan, D. A. Smirnova, *et al.*, "Multifold enhancement of third-harmonic generation in dielectric nanoparticles driven by magnetic fano resonances," *Nano letters*, vol. 16, no. 8, pp. 4857–4861, 2016.

[138] M. Kerker, D.-S. Wang, and C. Giles, "Electromagnetic scattering by magnetic spheres," *JOSA*, vol. 73, no. 6, pp. 765–767, 1983.

[139] K. Koshelev, A. Bogdanov, and Y. Kivshar, "Engineering with bound states in the continuum," *Optics and Photonics News*, vol. 31, no. 1, pp. 38–45, 2020.

[140] L. Kang, H. Bao, and D. H. Werner, "Efficient second-harmonic generation in high q-factor asymmetric lithium niobate metasurfaces," *Optics Letters*, vol. 46, no. 3, pp. 633–636, 2021.

[141] Z. Han, F. Ding, Y. Cai, and U. Levy, "Significantly enhanced second-harmonic generations with all-dielectric antenna array working in the quasi-bound states in the continuum and excited by linearly polarized plane waves," *Nanophotonics*, vol. 10, no. 3, pp. 1189–1196, 2021.

[142] K. Koshelev, Y. Tang, K. Li, D.-Y. Choi, G. Li, and Y. Kivshar, "Nonlinear metasurfaces governed by bound states in the continuum," *Acs Photonics*, vol. 6, no. 7, pp. 1639–1644, 2019.

[143] C. Zhou, S. Li, C. Gong, Y. Wang, X. Liu, and M. Zhan, "Resonant asymmetric all-dielectric metasurface for boosting third-harmonic generation," *arXiv preprint arXiv:2004.01088*, 2020.

[144] M. Gandolfi, A. Tognazzi, D. Rocco, C. De Angelis, and L. Carletti, "Near-unity third-harmonic circular dichroism driven by a quasibound state in the continuum in asymmetric silicon metasurfaces," *Physical Review A*, vol. 104, no. 2, p. 023 524, 2021.

[145] G. Zograf, K. Koshelev, A. Zalogina, *et al.*, "High-harmonic generation from resonant dielectric metasurfaces empowered by bound states in the continuum," *ACS Photonics*, vol. 9, no. 2, pp. 567–574, 2022.

[146] C. Pfeiffer and A. Grbic, "Bianisotropic metasurfaces for optimal polarization control: Analysis and synthesis," *Physical Review Applied*, vol. 2, no. 4, p. 044 011, 2014.

[147] Y. Ra'di, V. S. Asadchy, and S. A. Tretyakov, "Tailoring reflections from thin composite metamirrors," *IEEE transactions on antennas and propagation*, vol. 62, no. 7, pp. 3749–3760, 2014.

[148] R. Alaee, M. Albooyeh, A. Rahimzadegan, M. S. Mirmoosa, Y. S. Kivshar, and C. Rockstuhl, "All-dielectric reciprocal bianisotropic nanoparticles," *Physical Review B*, vol. 92, no. 24, p. 245 130, 2015.

[149] J. Dixon, M. Lawrence, D. R. Barton III, and J. Dionne, "Self-isolated raman lasing with a chiral dielectric metasurface," *Physical Review Letters*, vol. 126, no. 12, p. 123 201, 2021.

[150] A. B. Evlyukhin, V. R. Tuz, V. S. Volkov, and B. N. Chichkov, "Bianisotropy for light trapping in all-dielectric metasurfaces," *Physical Review B*, vol. 101, no. 20, p. 205 415, 2020.

[151] R Alaee, M Albooyeh, M Yazdi, *et al.*, "Magnetoelectric coupling in nonidentical plasmonic nanoparticles: Theory and applications," *Physical Review B*, vol. 91, no. 11, p. 115 119, 2015.

[152] M. Yazdi, M. Albooyeh, R. Alaee, *et al.*, "A bianisotropic metasurface with resonant asymmetric absorption," *IEEE Transactions on Antennas and Propagation*, vol. 63, no. 7, pp. 3004–3015, 2015.

[153] R. Alaee, M. Albooyeh, and C. Rockstuhl, "Theory of metasurface based perfect absorbers," *Journal of Physics D: Applied Physics*, vol. 50, no. 50, p. 503 002, 2017.

[154] X. Wang, G. Ptitcyn, V. Asadchy, *et al.*, "Nonreciprocity in bianisotropic systems with uniform time modulation," *Physical Review Letters*, vol. 12 5, no. 26, p. 266 102, 2020.

[155] L. Cheng, R. Alaee, A. Safari, M. Karimi, L. Zhang, and R. W. Boyd, "Superscattering, superabsorption, and nonreciprocity in nonlinear antennas," *ACS Photonics*, vol. 8, no. 2, pp. 585–591, 2021.

[156] C. F. Bohren and D. R. Huffman, *Absorption and scattering of light by small particles*. John Wiley & Sons, 2008.

[157] G. Mie, "Beiträge zur optik trüber medien, speziell kolloidaler metallösungen," *Annalen der physik*, vol. 330, no. 3, pp. 377–445, 1908.

[158] S. Mühlig, C. Menzel, C. Rockstuhl, and F. Lederer, "Multipole analysis of meta-atoms," *Metamaterials*, vol. 5, no. 2-3, pp. 64–73, 2011.

[159] R. Alaee, C. Rockstuhl, and I. Fernandez-Corbaton, "An electromagnetic multipole expansion beyond the long-wavelength approximation," *Optics Communications*, vol. 407, pp. 17–21, 2018.

[160] I. Fernandez-Corbaton, S. Nanz, R. Alaee, and C. Rockstuhl, "Exact dipolar moments of a localized electric current distribution," *Optics express*, vol. 23, no. 26, pp. 33 044–33 064, 2015.

[161] V. S. Asadchy, A. Díaz-Rubio, and S. A. Tretyakov, "Bianisotropic metasurfaces: Physics and applications," *Nanophotonics*, vol. 7, no. 6, 1069 –1094, 2018.

[162] C. Caloz and A. Sihvola, "Electromagnetic chirality, part 1: The microscopic perspective [electromagnetic perspectives]," *IEEE Antennas and Propagation Magazine*, vol. 62, no. 1, pp. 58–71, 2020.

[163] Y. E. Terekhov, A. Zhuravlev, and G. Belokopytov, "The polarizability matrix of split-ring resonators," *Moscow University Physics Bulletin*, vol. 66, no. 3, pp. 254–259, 2011.

[164] F. H. Stillinger and D. R. Herrick, "Bound states in the continuum," *Physical Review A*, vol. 11, no. 2, p. 446, 1975.

[165] Z. Sadrieva and A. Bogdanov, "Bound state in the continuum in the one-dimensional photonic crystal slab," in *Journal of Physics: Conference Series*, IOP Publishing, vol. 741, 2016, p. 012 122.

[166] A. I. Ovcharenko, C. Blanchard, J.-P. Hugonin, and C. Sauvan, "Bound states in the continuum in symmetric and asymmetric photonic crystal slabs," *Physical Review B*, vol. 101, no. 15, p. 155 303, 2020.

[167] H. Tang, C. DeVault, S. A. Camayd-Muñoz, *et al.*, "Low-loss zero-index materials," *Nano Letters*, vol. 21, no. 2, pp. 914–920, 2021.

[168] K. Koshelev, S. Lepeshov, M. Liu, A. Bogdanov, and Y. Kivshar, "Asymmetric metasurfaces with high-q resonances governed by bound states in the continuum," *Physical review letters*, vol. 121, no. 19, p. 193 903, 2018.

[169] M. V. Rybin, K. L. Koshelev, Z. F. Sadrieva, *et al.*, "High-q supercavity modes in subwavelength dielectric resonators," *Physical review letters*, vol. 119, no. 24, p. 243 901, 2017.

[170] A. B. Evlyukhin, C. Reinhardt, E. Evlyukhin, and B. N. Chichkov, "Multipole analysis of light scattering by arbitrary-shaped nanoparticles on a plane surface," *JOSA B*, vol. 30, no. 10, pp. 2589–2598, 2013.

[171] P. D. Terekhov, V. E. Babicheva, K. V. Baryshnikova, A. S. Shalin, A. Karabchevsky, and A. B. Evlyukhin, "Multipole analysis of dielectric metasurfaces composed of nonspherical nanoparticles and lattice invisibility effect," *Physical Review B*, vol. 99, no. 4, p. 045 424, 2019.

[172] J. D. Jackson, "Classical electrodynamics john wiley & sons," *Inc., New York*, vol. 13, 1999.

[173] M. Odit, P. Kapitanova, P. Belov, R. Alaee, C. Rockstuhl, and Y. S. Kivshar, "Experimental realisation of all-dielectric bianisotropic metasurfaces," *Applied Physics Letters*, vol. 108, no. 22, p. 221 903, 2016.

[174] V. Asadchy, M. Albooyeh, and S. Tretyakov, "Optical metamirror: All-dielectric frequency-selective mirror with fully controllable reflection phase," *JOSA B*, vol. 33, no. 2, A16–A20, 2016.

[175] D. Jalas, A. Petrov, M. Eich, *et al.*, "What is—and what is not—an optical isolator," *Nature Photonics*, vol. 7, no. 8, pp. 579–582, 2013.

[176] C. Gigli, T. Wu, G. Marino, A. Borne, G. Leo, and P. Lalanne, "Quasinormal-mode non-hermitian modeling and design in nonlinear nanooptics," *ACS photonics*, vol. 7, no. 5, pp. 1197–1205, 2020.

[177] S. S. Kruk, L. Wang, B. Sain, *et al.*, "Asymmetric parametric generation of images with nonlinear dielectric metasurfaces," *Nature Photonics*, pp. 1–5, 2022.

[178] L. Ottaviano, M. Pu, E. Semenova, and K. Yvind, "Low-loss high-confinement waveguides and microring resonators in algaas-on-insulator," *Optics Letters*, vol. 41, no. 17, pp. 3996–3999, 2016.

[179] K. Vyas, "Design, fabrication and testing of novel iii-v waveguides architectures for nonlinear integrated photonic applications," Ph.D. dissertation, Université d'Ottawa/University of Ottawa, 2022.

[180] R. W. Boyd, *Nonlinear optics*. Academic press, 2020.

[181] S. Liu, P. P. Vabishchevich, A. Vaskin, *et al.*, "An all-dielectric metasurface as a broadband optical frequency mixer," *Nature communications*, vol. 9, no. 1, pp. 1–6, 2018.

[182] P. Franken, A. E. Hill, C. e. Peters, and G. Weinreich, "Generation of optical harmonics," *Physical Review Letters*, vol. 7, no. 4, p. 118, 1961.

[183] G. P. Agrawal, *Nonlinear Fiber Optics*. Springer, 2007.

[184] F. Yoshino, S. Polyakov, and G. I. Stegeman, "All-optical multiphoton absorption figures of merit: Polydiacetylene poly (bis para-toluene sulfonate) of 2, 4-hexadiyne-1, 6 diol," *Applied physics letters*, vol. 84, no. 26, pp. 5362–5364, 2004.

[185] S. May, M. Clerici, and M. Sorel, "Supercontinuum generation in dispersion engineered algaas-on-insulator waveguides," *Scientific Reports*, vol. 11, no. 1, pp. 1–7, 2021.

[186] X. Li, Z. Wang, and H. Liu, "The coupled nonlinear schrödinger equations describing power and phase for modeling phase-sensitive parametric amplification in silicon waveguides," *Journal of Applied Mathematics*, vol. 2014, 2014.

[187] N. Shibata, R. Braun, and R. Waarts, "Phase-mismatch dependence of efficiency of wave generation through four-wave mixing in a single-mode optical fiber," *IEEE Journal of Quantum Electronics*, vol. 23, no. 7, pp. 1205–1210, 1987.

[188] R. Tkach, A. Chraplyvy, F. Forghieri, A. Gnauck, and R. Derosier, "Four-photon mixing and high-speed wdm systems," *Journal of Lightwave Technology*, vol. 13, no. 5, pp. 841–849, 1995.

[189] D. H. G. Espinosa, K. M. Awan, M. Odungide, S. R. Harrigan, D. R. Sanchez, and K. Dolgaleva, "Tunable four-wave mixing in algaas waveguides of three different geometries," *Optics Communications*, vol. 47 9, p. 126 450, 2021.

[190] S. Saeidi, P. Rasekh, K. M. Awan, A. Tüğen, M. J. Huttunen, and K. Dolgaleva, "Demonstration of optical nonlinearity in ingaasp/inp passive waveguides," *Optical Materials*, vol. 84, pp. 524–530, 2018.

[191] D. Botez, "Ingaasp/inp double-heterostructure lasers: Simple expressions for wave confinement, beamwidth, and threshold current over wide ranges in wavelength (1.1-1.65 μm)," *IEEE Journal of Quantum Electronics*, vol. 17, no. 2, pp. 178–186, 1981.

[192] R. Nelson and N. Dutta, "Review of ingaasp/inp laser structures and comparison of their performance," *Semiconductors and Semimetals*, vol. 22, pp. 1–59, 1985.

[193] L. C. Comandar, B. Fröhlich, J. F. Dynes, *et al.*, "Gigahertz-gated ingaas/inp single-photon detector with detection efficiency exceeding 55% at 1550 nm," *Journal of Applied Physics*, vol. 117, no. 8, p. 083 109, 2015.

[194] X. Jiang, M. A. Itzler, R. Ben-Michael, and K. Slomkowski, "Ingaasp–inp avalanche photodiodes for single photon detection," *IEEE Journal of selected topics in quantum electronics*, vol. 13, no. 4, pp. 895–905, 2007.

[195] M. Razeghi, "High-power laser diodes based on ingaasp alloys," *Nature*, vol. 369, no. 6482, pp. 631–633, 1994.

[196] K Mettler, "Design and performance of high power semiconductor lasers," in *ESSDERC'87: 17th European Solid State Device Research Conference*, IEEE, 1987, pp. 817–825.

[197] *The Advantages of Indium Phosphide Photonic Integration in Highperformance Coherent Optics*. https://www.infinera.com/.

[198] L. Chee-Wei and C. Mee-Koy, "Room-temperature inductively coupled plasma etching of inp using cl2/n2 and cl2/ch4/h2," *Chinese Physics Letters*, vol. 23, no. 4, p. 903, 2006.

[199] V. Donnelly, D. Flamm, C. Tu, and D. Ibbotson, "Temperature dependence of inp and gaas etching in a chlorine plasma," *Journal of the Electrochemical Society*, vol. 129, no. 11, p. 2533, 1982.

[200] G Tittelbach, B Richter, and W Karthe, "Comparison of three transmission methods for integrated optical waveguide propagation loss measurement," *Pure and Applied Optics: Journal of the European Optical Society Part A*, vol. 2, no. 6, p. 683, 1993.

[201] J. M. Vaughan, *The Fabry–Perot interferometer: history, theory, practice and applications*. Routledge, 2017.

[202] L. Yin and G. P. Agrawal, "Impact of two-photon absorption on self-phase modulation in silicon waveguides," *Optics letters*, vol. 32, no. 14, pp. 2031–2033, 2007.

[203] J. Choi, B.-U. Sohn, G. Chen, D. Ng, and D. Tan, "Broadband incoherent four-wave mixing and 27 db idler conversion efficiency using ultra-silicon rich nitride devices," *Applied Physics Letters*, vol. 112, no. 18, p. 181 101, 2018.